

Developing new experimental techniques to investigate the Co-linear Cluster Tri-partitioning.



Riaan Louw Korsten

Thesis presented in the partial fulfilment
of the requirement for the degree of
MSc Physics (Nuclear Physics)
at the University of Stellenbosch

Supervisor: Prof. S.M. Wyngaardt

Co-Supervisors: Dr. V.D. Malaza,
Prof. Yu.V. Pyatkov

December 2022

PLAGIARISM DECLARATION

1. Plagiarism is the use of ideas, material and other intellectual property of another's work and to present it as our own.
2. We agree that plagiarism is a punishable offence because it constitutes theft.
3. Accordingly, all quotations and contributions from any source whatsoever (including the internet) have been cited fully. We understand that the reproduction of text without quotation marks (even when the source is cited) is plagiarism.
4. We also understand that direct translations are plagiarism.
5. We declare that the work contained in this thesis, except otherwise stated, is our original work and that we have not previously (in its entirety or in part) submitted it for grading in this thesis or another thesis.

R.L. Korsten	23 December 2022
Initials and surname	Date

ACKNOWLEDGEMENTS

Before starting, I would like first to extend a heartfelt thanks to some people, as without their support, this would not have been possible. To my supervisor, Prof. S. M. Wyngaardt: Thank you very much for all the help and guidance you have given me during this study and how understanding and patient you were with me.

To my Co-supervisors:

- Dr. V.D. Malaza: Thank you for all the help you have given me, from showing me around Dubna for the first time, to explaining new concepts and work to me.
- Prof. Yu.V. Pyatkov: I give thanks for all the assistance you gave me during my time in Russia and in South-Africa, and for all the time you spent carefully explaining things and helping me, making sure that I understood all of the little details.

I would also like to thank my colleagues from the group at the Flerov Laboratory in JINR, you were all very welcoming and immediately made me feel at home. To Dr D.V. Kamanin, I thank for inviting me to be a part of such an amazing research group, and for making sure that I could thrive in that environment. A special thanks to Z. I. Goryainova and A.O. Strekalovsky, for your friendship, and all of the assistance given by teaching and familiarizing me with the experimental equipment and data processing techniques.

Finally I would like to thank both of my parents, for your constant love, support and encouragement. Ek is baie Lief vir julle. To God all the praise.

ABSTRACT

Computational simulations were developed to calculate data collection efficiency, as well as data accuracy for existing experimental setups used in the study of the exotic ternary decay of low excited heavy nuclei known as Co-linear Cluster Tri-partitioning (CCT) [1]. The most populated CCT mode containing the so called “Ni-bump”. This bump is centered at the masses associated with the magic isotopes of Ni (which include ^{68}Ni and ^{72}Ni). The results from these simulations give new insight into the identification capability of heavy ions using current experimental equipment and hint at some possible solutions to increase data collection efficiency and data accuracy.

As a charged particle interacts with the material of a semiconductor detector and deposits energy into it, it creates high conductivity plasma along the trajectory of the particle. This disrupts the internal electric field of the detector for some time which retards data collection. This effect is known as Plasma Delay (PD). Development of a new algorithm and subsequent computational implementation of this algorithm -Paraspline algorithm-, with the goal of more accurate time-of-flight (TOF) calculations, by correcting for the PD effect in semiconductor detectors. Testing of this algorithm show promising results, potentially improving the reliability of future experimental results.

OPSOMMING

TABLE OF CONTENTS

PLAGIARISM DECLARATION	ii
ACKNOWLEDGEMENTS	iii
ABSTRACT	iv
OPSOMMING	v
LIST OF FIGURES	ix
LIST OF TABLES	xv
LIST OF APPENDICES	xvi
LIST OF ABBREVIATIONS AND/OR ACRONYMS	xvii
1 BACKGROUND ON NUCLEAR PHYSICS	1
1.1 History	1
1.2 Nuclear instability	4
1.2.1 Fusion	4
1.2.2 Fission	4
1.2.3 Nuclear Decay	7
1.3 Current topics in nuclear physics	10
2 CLUSTERING AND FISSION	11
2.1 Fission Barrier	11
2.2 Exotic modes of fission decay	12
2.3 Nuclear Clustering	14
2.4 Ternary Fission	18
2.5 Fission Shape Isomers	20
3 EXOTIC NUCLEAR FISSION AND RELATED EXPERIMENTAL METHODS	22

3.1	Collinear Cluster Tri-partition	22
3.2	Experimental setups and further evidence of CCT	24
3.2.1	FOBOS and modified FOBOS spectrometer	24
3.2.2	COMETA	34
3.2.3	LIS - Light Ion Spectrometer	37
3.2.4	VEGA	39
3.3	Experimental Equipment	44
3.3.1	PIN Diode Detectors	44
3.3.2	Micro-Channel Plate Time Based Detectors	44
3.3.3	The Californium-252 source (^{252}Cf)	46
3.4	Experimental Manifestations	51
3.4.1	Pulse height defect (PHD)	51
3.4.2	Plasma Delay (PD)	52
4	SIMULATIONS AND DATA PROCESSING	55
4.1	Probability estimation of detecting CCT events	55
4.1.1	Goal of this section	55
4.1.2	Method to accomplish this	56
4.2	Distance distributions of detected particles	59
4.2.1	Goal of this section	59
4.2.2	Method to accomplish this	59
4.3	New time-pick-off “Paraspline” algorithm	61
4.3.1	Problem Outline	61
4.3.2	Paraspline algorithm description	62
4.3.3	Paraspline testing methods	66
5	RESULTS	71
5.1	Probability estimation of detecting CCT events	71
5.2	Distance distributions of detected particles	73
5.3	New time-pick-off “Paraspline” algorithm	76
5.3.1	Noise to signal ratio test results	76

5.3.2	Clean signal + real noise test results	77
5.3.3	Results of the experiment at IC-100 reactor	78
6	CONCLUSION AND FURTHER OUTLOOK	87
6.1	Conclusions	87
6.2	Improvements and shortcomings	87
	REFERENCES	95
	APPENDIX A MASS RECONSTRUCTION PROCEDURE	96
	APPENDIX B SPLINES	97
	APPENDIX C CODE	98
C.0.1	Probability Estimation	98
C.0.2	Distance Distribution	106

LIST OF FIGURES

1.1	Early diagram of an atom based on Rutherford's model	2
1.2	Average binding energy per nucleon inside the nucleus of atoms. . .	3
1.3	Fission fragment mass distribution for thermal neutron induced fission of ^{235}U , ^{233}U and ^{239}Pu	5
1.4	An early model for depicting the process of neutron induced fission, as described by the liquid drop model.	6
1.5	Neutron Induced fission.	6
2.1	Depictions of various different types of clustering, these include small clusters inside a closed shell, halo nucleons outside of a normal core, and instances of complete condensation into α - particle clusters. . .	14
2.2	Calculated density contour plots for ^4Be , and slightly excited ^{12}C and ^{16}O , illustrating how these nuclei consist of α -particles.	15
2.3	Calculated density (in fm^{-3}) contours of ^8Be resting lab frame (left) and the intrinsic frame (some rotational momenta, right), showing clear distinction of two α - particles.	15
2.4	Modified "Ikeda-Diagram" depicting molecular shape isomers in light neutron-rich isotopes of nuclei, these consisting of ^4He -, ^{16}O -, ^{14}C -clusters and some covalently bound neutrons (Xn means X neutrons). This so called diagram with α -particles (left panel) and ^{16}O -cores (middle panel) can be generalized to ^{14}C -cluster cores (right panel). The threshold energies needed to change the shape of the nuclei into these particular configurations are given below each diagram in MeV.	16
2.5	$(\overline{D}(\overline{Z}_2, \overline{N}_2))$ corresponding to cluster preformation probability in ^{232}Th of certain clusters as a function of the cluster charge (\overline{Z}_2)	18
2.6	The bottoms of the fission valleys as a function of parameter Q (proportional to the quadrupole moment) for ^{246}Cm . The panels depict the shapes of the fissioning system at the points marked by arrows. .	21

3.1	Depiction of conventional ternary fission (left) versus. depictions of two different modes of CCT (right)	23
3.2	Schematic of the FOBOS Spectrometer. (1)-Structural frame. (2)-Detection module.	25
3.3	Detector module for the FOBOS spectrometer: 1 outer part of the BIC, 2. Supporting grid for the entrance window, 3. PSAC, 4. Thin foil, 5. Teflon cone, 6. Grid, 7. Anode, 8. HV divider, 9. Scintillation shell	26
3.4	Schematic view of the modified-FOBOS spectrometer	27
3.5	Picture of the modified-FOBOS spectrometer	28
3.6	Diagram of the modified-FOBOS spectrometer setup, note that source has a thin Al_2O_3 backing in “arm 1”	29
3.7	Contour map with the mass-mass distribution of the collinear fragments detected in coincidence from the two opposite arms of the FOBOS spectrometer setup.	30
3.8	Schematic view of the mini-FOBOS spectrometer showing 1-’start’ avalanche counter, 2-BIC, 3-PSAC and 4-beam of thermal neutrons .	31
3.9	Picture of the mini-FOBOS spectrometer.	32
3.10	Projections of the “Ni-bump” onto M_1 for both the spontaneous fission of ^{252}Cf and neutron induced fission of ^{235}U	33
3.11	Diagram of the COMETA with PIN diodes (d), MCP Time Based detector (b) with ^{252}Cf source (a), and a neutron belt (c) that consists of 28 neutron detectors.	35
3.12	Picture of the COMETA setup.	36
3.13	Diagram showing the possible configurations of fragments hitting the array of PINs, (note trajectory marked “3” hits the array structure and is not detected)	37
3.14	Mass-mass distribution of the two heavier CCT fragments. Each data point represent three individual fragments registered, with the condition $m_1 < m_2 < m_3$	38

3.15	Layout of LIS spectrometer.	39
3.16	Picture of the VEGA experimental setup, the elongated flight tube of the can be seen extending from the center to the bottom left of the picture.	41
3.17	Mass correlation distribution for coincidence detected fission fragments in separate PIN-diodes(a) and the data from box marked w1 (b)	42
3.18	Two different fission valleys shapes of the fissioning ^{252}Cf nucleus. .	42
3.19	Diagram of a PIN-Diode showing the three different layers of semiconductors, p-type semiconductor intrinsic semiconductor and n-type semiconductor.	44
3.20	Picture of a PIN diode used inside an α spectrometer. The Capton tape is used to shield the border region of the active surface.	45
3.21	The schematic view that shows how the MCP detects the heavy ions passing through via the scattered electrons.	46
3.22	The schematic view that shows how the electrons scattered from the heavy ion get detected by the MCP plate of the MCP detector. . . .	47
3.23	Picture of the MCP time-based detector and the PIN diode attached behind the MCP.	47
3.24	Photo of one of the ^{252}Cf sources used in this study, the thin coating of ^{252}Cf on top of the aluminium backing can be seen as the circular disk with a slightly lighter colour.	49
3.25	Photo of another ^{252}Cf source inside of a vacuum chamber.	50
3.26	Picture showing how PIN diodes where tested inside a clean room to determine their peak working voltage.	54
4.1	Diagram of the curved detector array (160mm x 40mm), with the 3 labeled different possible locations a particle can hit the array, with the black lines serving as examples of particle trajectories. All PIN diodes are 150 mm from the center of the source.	56
4.2	Diagram of the setup under investigation.	60

4.3	Output amplitude(arbt. units) versus time(ns), signal output from a PIN diode after a HCP impacted upon it.	61
4.4	Red Line yb - Local average of the noise, Blue Lines - $[yb-3\sigma, yb+3\sigma]$ noisy region, Orange - Fitted spline, Green - parabola with vertex at the signal start time.	63
4.5	Example of a signal where the section of the signal between 0 ns and 30 ns could be seen as a noise-only region	67
4.6	Experimental setup of the experiment at IC-100 accelerator. Target - Al, Ti, Cu, Ag, Au, Zr or Ni foil; Start TD, Stop TD - MCP time detectors; Degradar - Ti and Al foil of different thickness. L1 = 500 mm, L2 = 142 mm, L3 = 141 mm	69
4.7	Photo of the target knot of the experimental setup at IC-100 accelerator. 70	
5.1	This graph simulates 1000 000 events per angle, in angular increments of 0.01 degrees.	71
5.2	This graph simulates 1000 000 events per angle, with 1000 different angles between 0-10 degrees. This is done for each of the 10 different target sizes.	72
5.3	This graph simulates 1000 000 events per angle, with 1000 different angles between 0-10 degrees. This is done for each of the 10 different target sizes. Zoomed in on the significant part of the smaller angles. 73	
5.4	Histogram of the amount of different distances calculated for the configuration (d = 0 mm).	74
5.5	Histogram of the amount of different distances calculated for the configuration (d = 5 mm).	74
5.6	Histogram of the amount of different distances calculated for the configuration (d = 16 mm).	75
5.7	Histogram of the amount of different distances calculated for the configuration (d = 20 mm).	75
5.8	Clean signal with $\pm 2\%$ of the signals maximum amplitude added. .	76
5.9	Clean signal with $\pm 20\%$ of the signals maximum amplitude added. .	76

5.10	Clean signal with $\pm 40\%$ of the signals maximum amplitude added. .	77
5.11	Experimental mass [a.m.u] spectrum from the ^{252}Cf source in LIS setup (blue line – experimental data, dotted line –literature data).(y-axis in arbt. units)	78
5.12	Experimental velocity [cm/ns] spectrum from the ^{252}Cf source in LIS spectrometer experiment(blue line – experimental data, dotted line –literature data)(y-axis in arbt. units).	79
5.13	Mean difference $< V2 - V1 >$ as a function of $V1$ for the fragments from the ^{252}Cf source in LIS spectrometer experiment.	80
5.14	$M(\text{a.m.u})$ as a function of Energy (MeV) in experiment with Al emitter and 5 μm thick Ti foil degrader at IC-100 accelerator.	81
5.15	$< M >$ (a.m.u) as a function of Energy (MeV) in experiment with Al emitter and 5 μm thick Ti foil degrader at IC-100 accelerator. . . .	82
5.16	M (a.m.u) as a function of Energy (MeV) in experiment with Cu emitter and 5 μm thick Ti foil degrader at IC-100 accelerator.	83
5.17	$< M >$ (a.m.u) as a function of Energy (MeV) in experiment with Cu emitter and 5 μm thick Ti foil degrader at IC-100 accelerator. . .	84
5.18	M (a.m.u) as a function of Energy (MeV) in experiment with Xe emitter and no degrader at IC-100 accelerator.	85
5.19	$< M >$ (a.m.u) as a function of Energy (MeV) in experiment with Xe emitter and no degrader at IC-100 accelerator.	85
5.20	Energy/Mass distribution for all ions and all combination of degraders in the experiment at IC-100 accelerator (Standard Error of Mean is so small that error bars are omitted in the plot).	86
A.1	Flow diagram of the mass reconstruction procedure used to compensate for the pulse height defect.	96

B.1 The upper figure shows the dependence $f(x_i)=y_i$, $i=1,\dots,N$, of temperature from time in a certain water reservoir. The left column shows smoothing splines $\sigma_p(x_i)$, $i=1,\dots,n$, of order $q=2$, calculated for different values of the smoothing factor ($p=49, 9, 6.14, 1, 0.25, 0.01, 0.0001$, values of p indicated in the upper right corner of each chart in the left column). The right column shows graphs of the corresponding differences $\mu_p(x_i)=y_i-\sigma_p(x_i)$, $i=1,\dots,n$, and the red line on each chart in the right column shows smoothing splines σ'_p , calculated on the basis of differences $\mu_p(x_i)=y_i-\sigma_p(x_i)$, $i=1,\dots,n$. In the upper right corner of each chart the norm value is shown in the right column $\|\nu_p(x)\|^2$, $p=49, 9, 6.14, 1, 0.25, 0.01, 0.0001$. It can be seen that the value $\|\nu_p(x)\|^2$ is minimal for $p_{\text{opt}}=1$, which determines the optimal smoothing spline σ_{opt} 97

LIST OF TABLES

5.1	Table containing some of the results from the second test on the Paraspine method.	77
-----	--	----

LIST OF APPENDICES

APPENDIX A	Mass reconstruction procedure
APPENDIX B	Splines
APPENDIX C	Simulation Code

LIST OF ABBREVIATIONS AND/OR ACRONYMS

BCM	Binary Cluster Model
CCT	Collinear Cluster Tri-partition
FLNR	Flerov Laboratory of Nuclear Reactions
ff	Fission Fragment
HCP	Heavy Charged Particle
JINR	The Joint Institute for Nuclear Research
LIS	Light Ion Spectrometer
LCP	Light Charged Particle
PD	Plasma Delay
PHD	Pulse Height Defect
SEMF	Semi-Empirical Mass Formula
TOF	Time-of-Flight

CHAPTER 1

BACKGROUND ON NUCLEAR PHYSICS

1.1 HISTORY

Nuclear physics is the study of the atomic nuclei, focusing mainly on the protons, neutrons and the complexity of the nucleon-nucleon interaction, and the structural properties of nuclei. Nuclear physics became distinct from atomic physics as a separate discipline in 1896 when radioactivity was discovered by Henri Becquerel which led to its inception [2].

In the years following the discovery of radioactivity a lot of work was done in this new field to further understand the phenomenon. Notably was the work of Marie Curie, Pierre Curie, and Ernest Rutherford earning them a shared Nobel Prize in 1903 [3] for further cementing the theory of radioactivity, Marie Curie now being famous as she was the first woman to receive this award. In these studies, three different types of radiation were postulated and in the years following proved experimentally. These were firstly alpha- and beta-radiation in 1899 [4] and later in 1903 gamma radiation was discovered. Knowing about these types of radiation and having some understanding of their interaction with matter proved to be instrumental in future discoveries surrounding nuclear physics.

The decades following this a lot of research was done to try and determine what the constituents of an atom was, as well as understanding the forces that governed its structure.

Following the discovery of nuclear spin in 1925 [5], it was clear that Rutherford's model of the atom (at the time the most developed model) was missing something, and hinted that there were still unknown parts of the nucleus. This missing piece was found by James Chadwick in 1932 in "The existence of a neutron " [6] with his discovery of the neutron. This particle had a mass slightly greater than that of the proton and had no electric charge. Later that year Dmitri Ivanenko [7] proposed that no electrons were inside the nucleus. With these two new pieces of the puzzle filled

in an updated version of Rutherford's model was created (depicted in figure 1.1). It still was not quite complete, it was however good enough for understanding the basics.

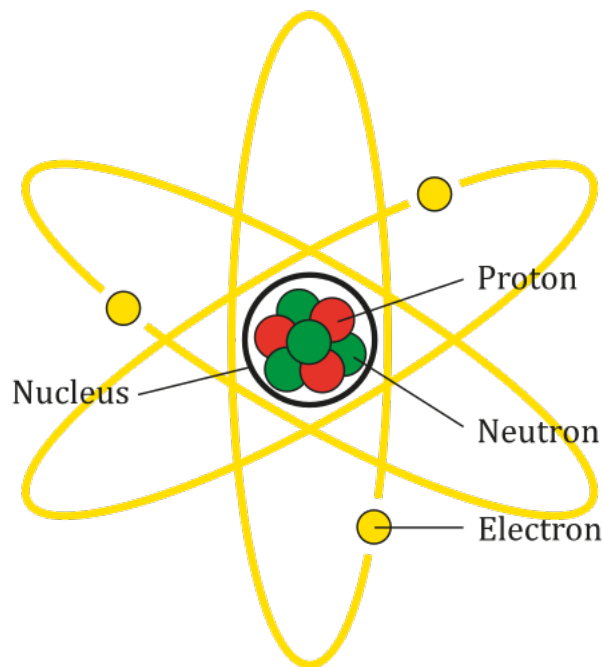


Figure 1.1: Early diagram of an atom based on Rutherford's model [8]

F. W. Aston [9] had discovered in 1920 that 4 Hydrogen atoms were heavier than a single Helium atom. Sir Arthur Eddington [10] used this information to develop his theory of nuclear fusion (see section 1.2.1), proposing that energy was released as Hydrogen fused together to form Helium inside the Sun. Physicists continued to build on the work of F. W. Aston and Sir Arthur Eddington to calculate the binding energy of the nucleus. Particles that are bound have some of their rest mass “lost” in the process of binding to another particle, this lost mass is converted to energy and is considered to be the binding energy between the particles. Binding energy is calculated by taking the difference between the mass of the nucleus's particles and the total mass of the nucleus. This difference is then converted to energy via Einstein's equation Figure 1.2 graphs this binding energy per nucleon vs the number of nucleons inside a given nucleus. Higher binding energies require more energy to break the bonds.

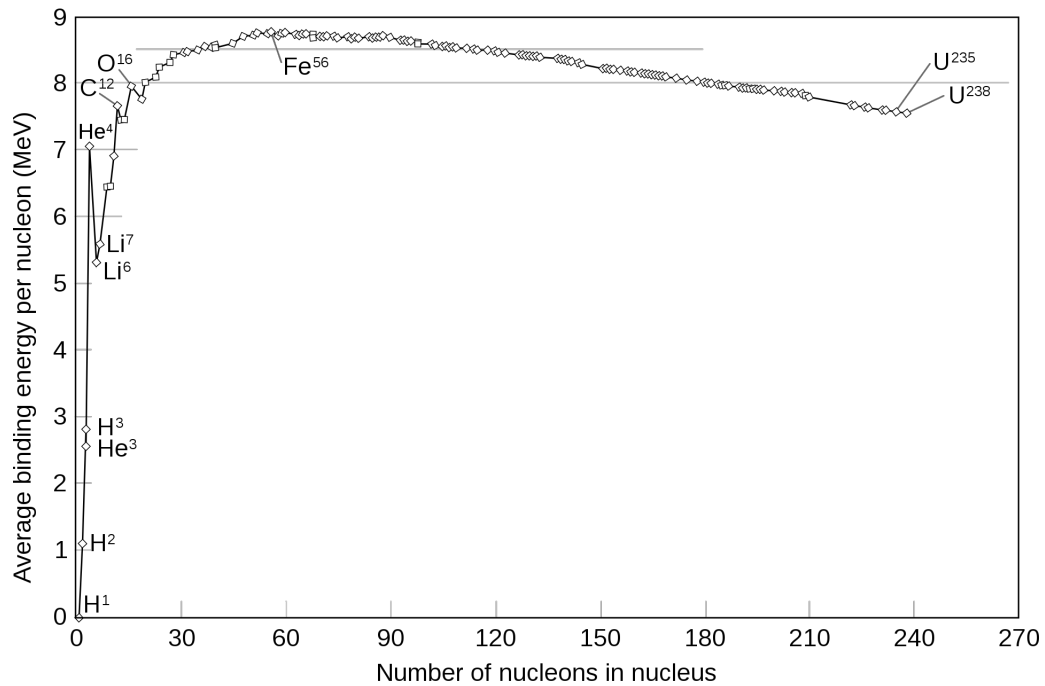


Figure 1.2: Average binding energy per nucleon inside the nucleus of atoms [11].

It was yet unclear what exactly held nuclei together that had more than one proton inside the nucleus, as protons repel each other via the electromagnetic force. Hideki Yukawa proposed his theory of the nuclear strong force in 1935 [12].

This new formulation of the nucleon-nucleon interaction would be mediated via a messenger particle, later discovered to be a meson [13]. This force is extremely strong force over short distances, and named the *residual strong force* or the more commonly used name *nuclear force*.

The strength of the nuclear force drops off drastically over larger distances and is why larger atoms require more neutrons inside the nucleus to remain stable, and why atoms can't just keep on getting bigger. With this final discovery, our understanding of the basic structure of the nucleus was completed, opening up the field of nuclear physics to more modern study in which we study the interactions between different nuclei and nucleons as well as the structure of the nucleus itself. As can be seen from figure 1.2 some atoms like ${}^4\text{He}$, ${}^{12}\text{C}$ and ${}^{16}\text{O}$ have a higher average binding energy per nucleon compared to the atoms that are next to them (local maximum)

indicating that these specific atoms are more likely to occur as clusters inside bigger nuclei, see section 2.3 for further information on this.

1.2 NUCLEAR INSTABILITY

1.2.1 Fusion

A major development in 1920 was when Arthur Eddington correctly proposed in “The Internal Constitution of the Stars ”[10] nuclear fusion as the mechanism in which stars produce energy. He also correctly predicted that the Sun had to have been mostly hydrogen for this to be the case.

Nuclear fusion is the process in which two light nuclei get close enough to one another to allow the strong force to fuse them into one single nucleus. As these atoms fuse energy is released equal to the difference in the sum of the initial two atoms binding energy and the binding energy of the product atom. Light atoms will fuse up to heavier atoms until they reach Ni-62, this is because Ni-62 has the highest binding energy per nucleon and is the most stable, and as such lighter atoms fusing into heavier ones produce a lot of energy as the system gets more stable.

1.2.2 Fission

Fission is the reverse of fusion, where heavier atoms split up into two (or more) lighter atoms. Here Ni-62 is again the threshold, where atoms heavier than Ni-62 will split up into smaller atoms often accompanied by one or more lone neutrons. Figure 1.3 shows what products are formed from different fissioning nuclei, note that there is a range of possible daughter products for any particular nucleus. This mass distribution of the daughter products doesn't include the neutrons. Similar to fusion having the constraint that the two atoms must be close enough, fission also has a constraint, this being that the atoms that will split needs to be unstable enough to overcome its own binding energy.

Fission was first discovered in 1938 by Lise Meitner and Otto Robert Frisch [14] when bombarding uranium with neutrons and finding barium isotopes in the products.

they explained this effect by using the liquid drop model. In this model proposed by George Gamow the nucleus of the uranium atoms acts like a drop of liquid, the incoming neutron perturbs the droplet enough to elongate it into a dumbbell shape before it splits at the thinnest part (known as the scission point) propelling the two ffs away from one another because of their electromagnetic repulsion. Figure 1.4 shows their explanation of the phenomenon.

This was a major new discovery as the amount of energy released in each of these fission events was orders of magnitude larger than the energy released from conventional chemical reactions. This type of fission was also easy to induce, needing only thermal (slow moving) neutrons to hit the Uranium nucleus in order to start the fission process. This culminated in the development of the atomic bomb near the end of the 2nd World War and the subsequent development of nuclear power plants in the 1950's.

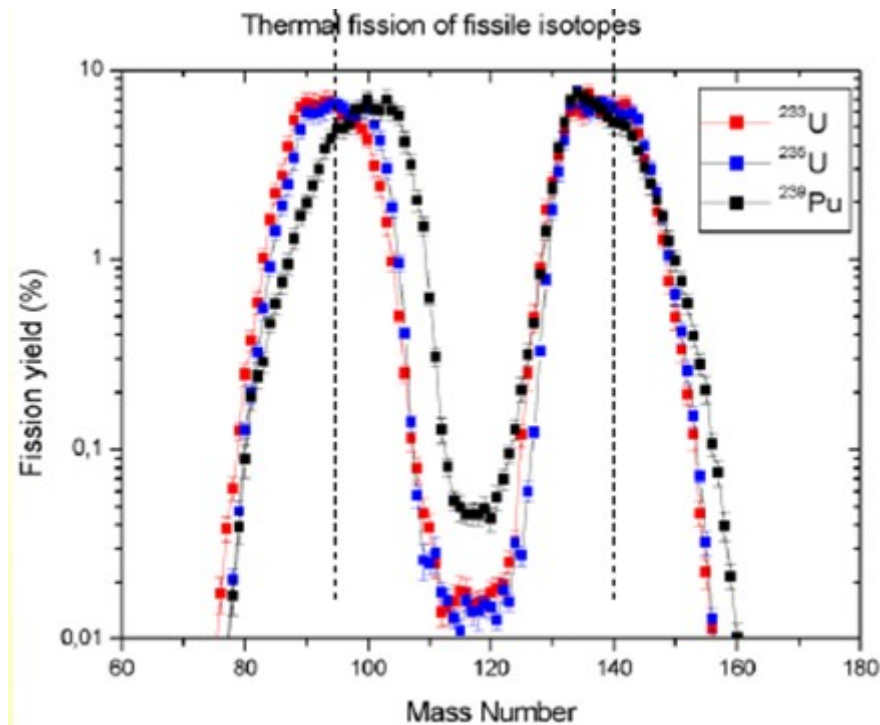


Figure 1.3: Fission fragment mass distribution for thermal neutron induced fission of ^{235}U , ^{233}U and ^{239}Pu [15]

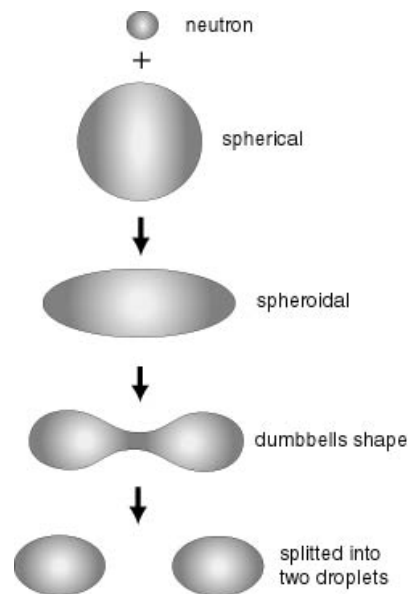


Figure 1.4: An early model for depicting the process of neutron induced fission, as described by the liquid drop model [16]. *Note: not all particles are shown.*

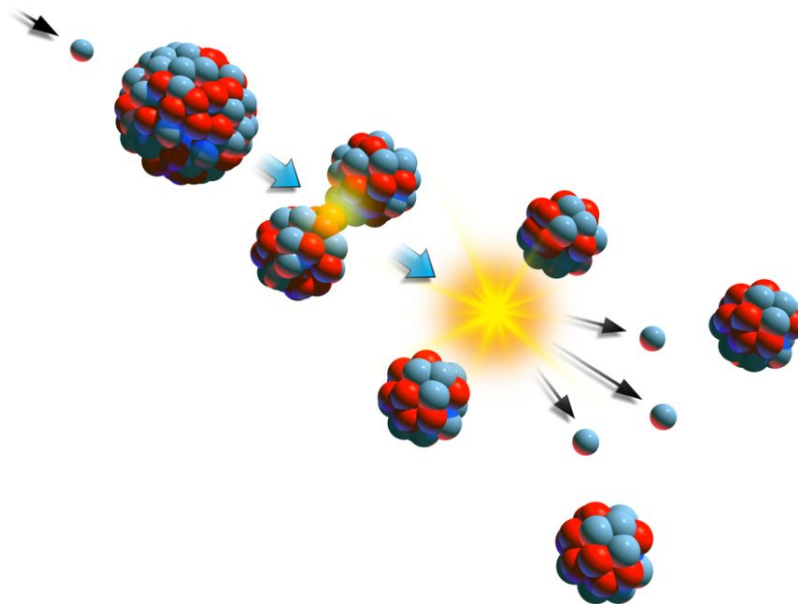


Figure 1.5: Neutron Induced fission [17]

1.2.2.1 *Spontaneous Fission*

Spontaneous fission was discovered in 1940 [18] by the Russian physicists Georgy N. Flerov and Konstantin A. Petrzhak, when they observed ^{238}U . This new form of fission required no neutron capture to initiate the fissioning process, seemingly happening on its own accord. It is observable in many isotopes of mass number 230 or more [19], and the chance of a this process occurring in any particular species of nuclei seems to be correlated to the atomic number of the nuclei. Nuclei with higher atomic numbers seem to undergo spontaneous fission more regularly. This rate at which these events happen is correlated to the half life of the atom in question. Half life is the amount of time it would take for half of a particular sample to decay radioactively.

Further study into the breakup of nuclei during a fission event found that these nuclei could break up into more than just two fission fragments [20]. Ternary fission is one such a case where the fissioning nucleus splits into three fission fragments. This will be discussed in more detail in Chapter 2.

1.2.3 Nuclear Decay

1.2.3.1 *Gamma Decay*

Radioactive decay is the process by which an unstable atomic nucleus loses energy via radiation, we say an unstable nucleus decays into a more energetically favourable state by some method of radiation. Fission among other decay methods is one of the mechanisms that cause this radiation. Most interestingly is ionizing radiation. This is classified as radiation that is considered to have enough energy to ionize matter it interacts with. One of these forms of ionizing radiation is produced in Gamma decay, which is the emission of an gamma photon from the nucleus to lower its energy. The energy (and therefore wavelength) of this gamma photon is equal to the energy lost by the nuclei as it decays to an lower and more stable state.

Gamma photons generally have an energy greater than 100 keV [21]. Gamma photons primarily interact with the electrons of other atoms and are quite penetrating,

especially in matter that has a low atomic number (and therefore low amount of electrons). Lead is typically used as a shielding material, as it has a high amount of electrons per atom and has a small atomic radius. Thus it is more 'electron dense' per volume and therefore attenuates gamma radiation quite well. This decay mode doesn't change the amount of or type of particles in the atom and as such its identity remains unchanged.

1.2.3.2 *Beta Decay* (β^\pm)

Beta decay is another form of ionising radiation and has two different modes, it is characterised by the emission of a electron or a positron. This changes the parent nuclei into an isobar of itself, i.e. the atomic mass (A) remains unchanged but the number of protons (Z) and neutrons(N) in the nucleus change.

β^- decay occurs when the weak interaction converts the parent nucleus into one with $Z \rightarrow Z+1$ by one, while emitting an electron (e^-) and an electron anti-neutrino ($\bar{\nu}_e$) as shown in equation 1.1 [22]. In this equation the parent nucleus is X and the daughter nucleus is represented by X'. Typically β^- decay occurs in neutron rich nuclei.



β^+ decay decreases the atomic number by one, while emitting a positron (e^+) and an electron neutrino (ν_e) as shown in equation 1.2 [22]. Again the parent nucleus is represented by X and the daughter nucleus is represented by X'. Typically β^+ decay occurs in to proton rich nuclei. This type of decay can also be considered as one of the protons inside the nucleus decaying into a neutron and an electron neutrino [22].



1.2.3.3 *Alpha Decay (α)*

α decay is characterised by the emission of a α -particle (^4He). This decreases the number of nucleons inside the nucleus by four. Two of these are protons and two are neutrons, which make up the α -particle. This typically happens in heavier nuclei with the lightest recorded nuclei undergoing α decay being the lightest isotopes (104-109) of Tellurium [23]. Generally α radiation has energies in excess of 1 MeV, however because of its highly charged nature it interacts very strongly with surrounding matter in its path, losing its energy along the way. Because of this α -particles usually lose almost all of their kinetic energy within a centimeter or two in air, this is similar for heavier charged particles and so trying to detect these particles as they were when they were emitted requires special experimental setups. To eliminate any loss of energy in these particles when trying to detect them the experiment is performed in a vacuum chamber. This removes practically all of the matter in the way flight path of the emitted ion, ensuring that a correct energy measurement can be taken.

Although radiation consisting of charged particles such as α radiation and β^\pm radiation is not as very penetrating, and therefore easier to shield, they are still considered to be dangerous. These charged particles themselves can emit photons in a wide spectrum of energies as they are slowed down in matter. This effect is called Bremsstrahlung (translates to 'braking radiation') and it is electromagnetic radiation produced by the deceleration of the charged particle.

1.3 CURRENT TOPICS IN NUCLEAR PHYSICS

One of the most impactful fields of study in nuclear physics is that of nuclear energy. Nuclear fission power for the purpose of electricity generation is in constant development, and it is still a very active field of study. But where the amount of research in fission reactors might have dipped of late, there has been a renewed uptake in the amount of research into fusion power as a energy source. This renewal is the result of various other developments in the fields of nuclear and laser physics as well as developments in material science and computer science. Inching us ever closer to stable and net-energy positive fusion reactors, and perhaps someday an even safer form of power generation.

Finally the subtle art of bombarding atoms with various different forms of matter and energy is also a very active field of nuclear physics, allowing the production and discovery of elements and isotopes not found in nature as well as exotic particles predicted by the Standard Model. By looking at the products of such bombardments we also gain increased insight into the structure and composition of the matter around us, as well as a better understanding of the forces that govern these structures. This has led to ion beam facilities being developed that have beams of radioactive and exotic nuclei, opening up many new and interesting avenues of study for nuclear physics.

It is in this final category where the focus of this study lies. Developing new experimental techniques to investigate and understand these and more exotic structures and processes better. With the aim to increase the degree of accuracy and reliability of experimental results relating to this, whilst simultaneously allowing further study into the phenomenon known as Collinear Cluster Tri-partition (CCT) [1].

CHAPTER 2

CLUSTERING AND FISSION

2.1 FISSION BARRIER

The fission barrier is the energy required for a nucleus of an atom to undergo fission or, more intuitively, the amount of energy needed to deform the nucleus enough so that it is irreversibly committed to the fission process. This start of the fission process is known as the scission point. In the case of neutron-induced fission, this deformation energy comes from external neutrons being captured by the nucleus. This external neutron carries energy (momentum), which excites the nucleus. The added neutron can also affect the fission barrier by changing the binding energy of the nucleus as it now has one more nucleon. In the case of spontaneous fission, this deformation energy can be acquired in many ways, one of which is Rutherford scattering. Binding energy as calculated from the Liquid Drop Model (equation 2.1) can be used as a basis to calculate the energy needed to overcome this barrier. This formula is also known as the semi-empirical mass formula (SEMF).

$$B_{LDM} = a_\nu A - a_s A^{2/3} - a_c \frac{Z(Z-1)}{A^{1/3}} - a_a \frac{(A-2Z)^2}{A} + \delta(N, Z) \quad (2.1)$$

here the coefficients a_ν (volume term), a_s (surface term), a_c (Coulomb term) and a_a (asymmetry term) are determined empirically. Z and N are the number of protons and neutrons respectively, with $A = Z + N$ (Atomic number). The pairing term consisting of a delta function shown in equation 2.2.

$$\delta(N, Z) = \begin{cases} +\delta_0 & Z, N \text{ even (A even)} \\ 0 & A \text{ odd} \\ -\delta_0 & Z, N \text{ odd (A even)} \end{cases} \quad (2.2)$$

These results however predict that nuclei containing more than $A=104$ cannot exist in a stable ground-state. By adding a shell corrections term [24] an energy value for the fission barrier (B_{fb}) can be calculated via equation 2.3 [25].

$$B_{fb} = B_{LDM} + \sum_{p,n} (\delta S + \delta P) \quad (2.3)$$

The delta function for δS and δP here have similar definitions to equation 2.2. These shell corrections tend to lower the ground state of nuclei with spherical shapes, as well as singly and doubly magic nuclei, effectively making these nuclei more stable. Singly magic nuclei have either proton- or neutron- shell filled and tend to very stable. Doubly magic nuclei have both proton and neutron shells filled making them en more stable than singly magic nuclei [25].

2.2 EXOTIC MODES OF FISSION DECAY

Included in spontaneous fission is “cluster” decay a.k.a. heavy particle radioactivity [26], which is the process of a small cluster of protons and neutrons are emitted from the nucleus. This cluster is larger than alpha particles but smaller than the typical Fission Fragment (ff). However this cluster decay is an extremely asymmetric spontaneous fission event. Typically defined as having decay products heavier than alphas and lighter than typical ffs ($A \approx 60$) [27]. Such exotic decay (cluster decay) was first observed by Rose and Jones [28], when they detected the emission of a carbon isotope from ^{223}Ra .

Another form of exotic decay is ternary fission , where a fissioning nuclei splits into three different nuclei, ternary fission is considered to be an exotic form of nuclear fission. Usually when ternary fission occurs two of the particle are heavier charged particles similar to conventional symmetric binary fission, with the third being a lighter charged particle, usually an α - particle [29]. This is however not always the case and this third particle can be more massive. Ternary fission itself is a lot less likely to occur than binary fission, and the case where a heavier third particle is emitted is also possible, however even more rare. Confirming the existence of such exotic states can be done by directly measuring them. This might be the most straightforward method, but is by no means the only one. Sometime directly measuring all these exotic particles experimentally can be problematic and so it

is necessary to confirm their existence in other methods. Some products(daughter particles) formed during the types of exotic decay mentioned above can be formed in excited states, and they themselves will then decay further. They might not have the required excitation energy to break through the fission barrier, but other decay modes exist for these particles such as those discussed in Chapter 1 (and many other). By measuring these secondary decay modes of the daughter particles you can infer the existence of those exotic states. This is one of the methods used to study the phenomenon known as Collinear Cluster Tri-partition (CCT), explained further in Chapter 3.

2.3 NUCLEAR CLUSTERING

As stated at the end of section 1.1, ${}^4\text{He}$ (α - particle) among others have a higher average binding energy per nucleon compared to the nuclei that are next to it. This large binding energy allows it to sometimes keep its own identity inside larger nuclei [30]. This identifiable partition of the nucleus inside a larger nucleus is defined as a nuclear cluster, and is not just confined to α - particles, with sometimes multiple and much larger clusters existing as part of even bigger nuclei [31]. As mentioned in the first section of this Chapter magic nuclei also have very high binding energies, and can therefore also form as clusters inside of larger nuclei.

Figure 2.1 has some examples of nuclei where parts of these nuclei consist of α - particles or α -chains. It is important to note that multi α - clusters and other heavier clusters not consisting of α -chains do also exist.

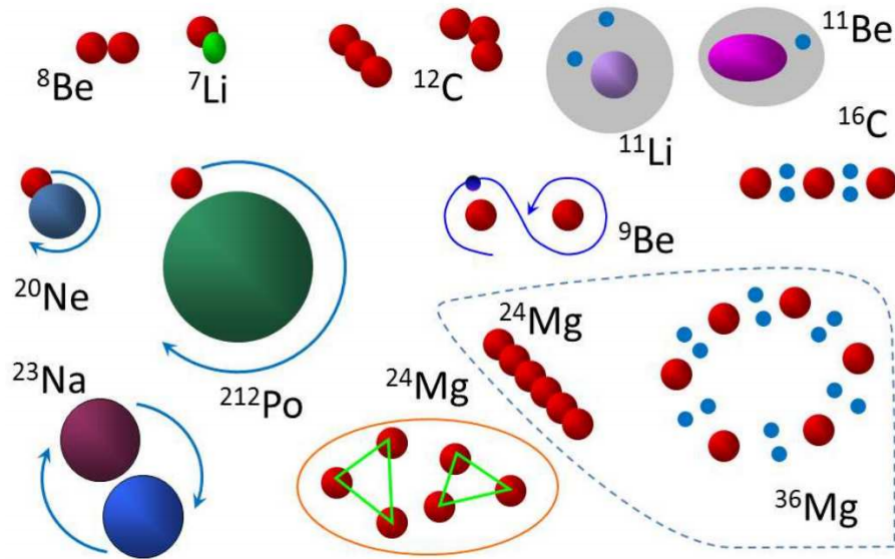


Figure 2.1: Depictions of various different types of clustering from [30], these include small clusters inside a closed shell, halo nucleons outside of a normal core, and instances of complete condensation into α - particle clusters.

As shown in figure 2.2 [32] one can see that in its ground state ${}^8\text{Be}$ can be viewed as two adjacent α - particles. Similarly in slightly excited ${}^{12}\text{C}$ and ${}^{16}\text{O}$ you can see that chains of α - particles exist.

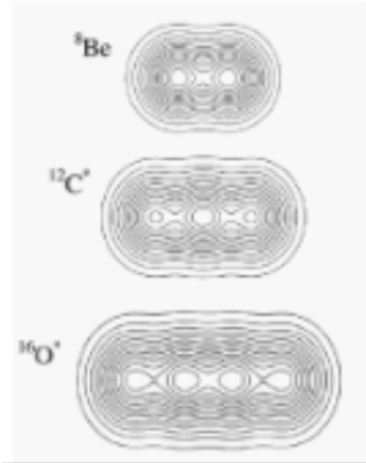


Figure 2.2: Calculated density contour plots for ${}^8\text{Be}$, and slightly excited ${}^{12}\text{C}$ and ${}^{16}\text{O}$, illustrating how these nuclei consist of α -particles. [33]

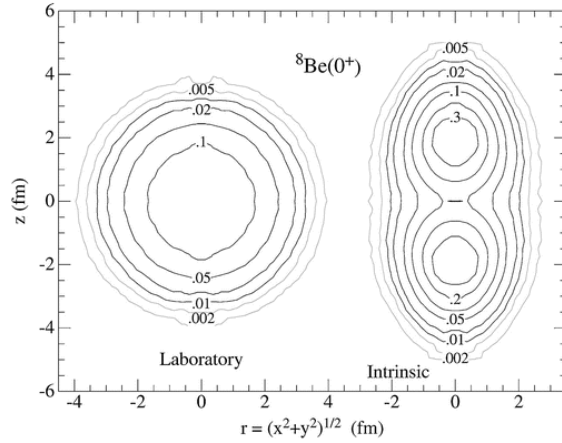


Figure 2.3: Calculated density (in fm^{-3}) contours of ${}^8\text{Be}$ resting lab frame (left) and the intrinsic frame (some rotational momenta, right), showing clear distinction of two α - particles. [33]

Clustering in light α -like nuclei is observed as a general phenomenon at high excitation energy close to the α -decay thresholds, this is shown to us in the famous Ikeda-diagram 2.4 [34].

Figure 2.4 is a modified (by Oertzen *et al.* [34]) version of this diagram containing more neutron-rich configurations, and serves as a nice visual example of cluster formation inside nuclei.

The Ikeda model for nuclear clustering is however not the only model. The Ikeda model focuses on the α - particle and nuclei that are made up of α -clusters and α -chains. Another model for example the "Asymmetric two-centre shell model" [35], functions by considering the interacting potential between the parent nucleus and the cluster as a superposition of two oscillators, a two-centre shell model. However when larger and more irregular nuclei emerge from cluster decay the Binary Cluster Model (BCM) is one of the simplest models one could consider. It was first proposed in 1975 by Buck *et al* [36], and consist of assuming that the cluster is a point particle orbiting around the core. The parent nucleus therefore consists of a core-cluster decomposition.

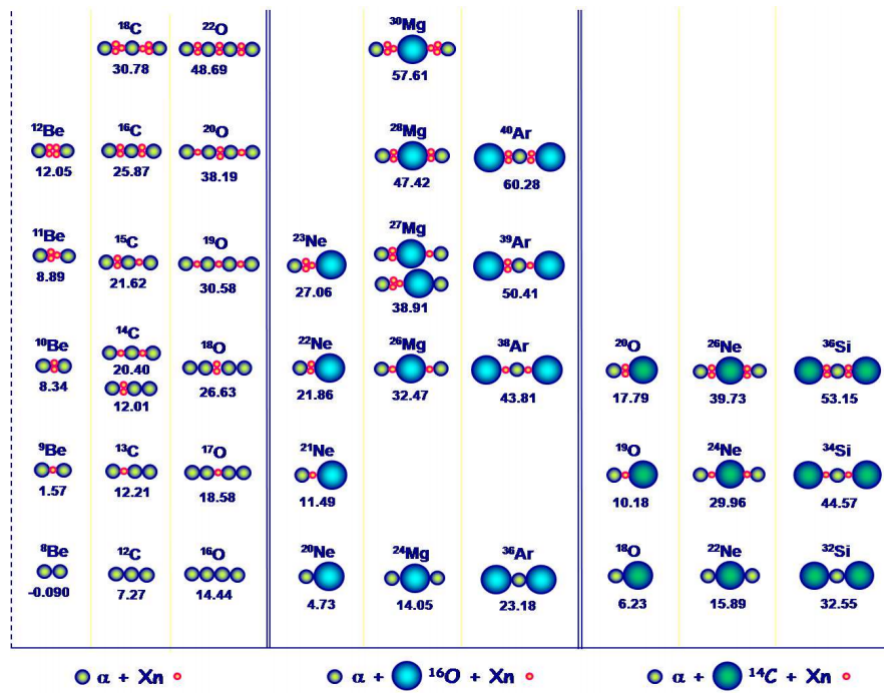


Figure 2.4: Modified “Ikeda-Diagram” depicting molecular shape isomers in light neutron-rich isotopes of nuclei, these consisting of ${}^4\text{He}$ -, ${}^{16}\text{O}$ -, ${}^{14}\text{C}$ -clusters and some covalently bound neutrons (Xn means X neutrons). This so called diagram with α -particles (left panel) and ${}^{16}\text{O}$ -cores (middle panel) can be generalized to ${}^{14}\text{C}$ -cluster cores (right panel). The threshold energies needed to change the shape of the nuclei into these particular configurations are given below each diagram in MeV [30].

The Model then assumes that there is some interacting potential between the core and the cluster, this is a central potential $V(r)$ and the BCM is defined by the Schrödinger equation 2.4.

$$\left(-\frac{\hbar^2}{2\mu}\frac{d^2}{dr^2} + V(r)\right)\varphi_{nL}(r) = E_{nL}\varphi_{nL}(r) \quad (2.4)$$

here μ is the reduced mass given by $\frac{A_1 A_2}{A_1 + A_2}$, L refers to the orbital angular momentum and n is the number of internal nodes. Here A_1 refers to the atomic mass number of the core and A_2 is the atomic mass number of the cluster. The potential $V(r)$ is the interacting potential between the core and the cluster.

In a study done by E.J. du Toit *et al* [37], a model was developed to determine viable core and cluster configurations, as well as the preformation probability of these clusters in excited nuclei. This model would work on the basis of the BCM, however would consider a nucleus consisting of up to four core-cluster decompositions. Results from this model for cluster preformation in ^{232}Th is shown in figure 2.5, by plotting the preformation probability of certain clusters as a function of the cluster charge. In this case it points $Z = 10$, suggesting Ne would be a likely cluster formed inside of ^{232}Th prior to decay, specifically ^{26}Ne was to the most likely. These results give strong theoretical evidence for the formation of cluster in heavy actinides prior to decay.

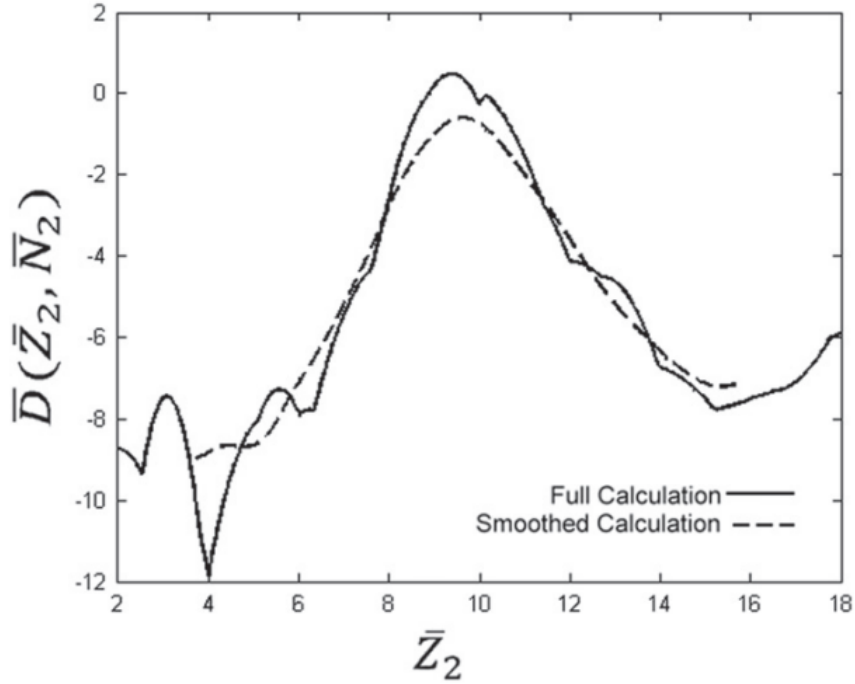


Figure 2.5: $(\bar{D}(\bar{Z}_2, \bar{N}_2))$ corresponding to cluster preformation probability in ^{232}Th of certain clusters as a function of the cluster charge (\bar{Z}_2) [37]

2.4 TERNARY FISSION

Ternary fission was first discovered in 1946 by L.L. Green and D.L. Liversy [20]. This conventional ternary fission is the process in which an extra Light Charged particle (LCP) is found as a product among the products of conventional binary fission. Most commonly this LCP is an alpha particle [29], but not always, and because of this third particle, the other two ffs would have slightly less mass than binary fission products. Similar to binary fission photons and neutrons with a range of different energies are also produced in ternary fission.

Because this third particle is relatively light compared to the other ffs, the repulsive Coulomb forces from the other more massive ffs expel it perpendicular to the fission axis. Since then ternary fission has been investigated a lot, and a multitude of different ternary fission mechanisms have been discovered. Some of these studies include [38], [39] and [26] among many others. These other mechanisms include

Polar emission, discovered by Piasecki [39], which is when the LCP is found to be moving along the fission axis. Research done by Y. Ronen [27] proved how similar some ternary fission modes and cluster decay are, somewhat muddying the water when trying to concretely differentiate between these decay modes. An example of this is ternary alpha emission, which is classed as alpha decay. Interestingly Y. Ronen found that the cluster commonly associated with cluster decay heavily correlates to the daughter particle yield in ternary fission, suggesting that ternary fission is a special mode where the fissioning nuclei undergo cluster decay at the last stage of scission.

2.5 FISSION SHAPE ISOMERS

It is possible for a nucleus to get trapped in a deformed state for a short period of time. Most actinides are not spheres but rather closer to a prolate shape when in their ground state. When these heavy nuclei get excited above their ground state they deform even further from a spherical form and can form metastable isomers, which slightly decreases how excited they are. This can cause them to get trapped in this highly deformed state, not having enough energy to overcome the fission barrier, but also not being deformed enough to not easily return to its ground state [40]. This deformed state is known as a fission shape isomer and can exist for a short amount of time. This fission shape isomer can then decay via spontaneous fission and/or decay back to the first minimum. Figure 2.6 shows some of the different shape isomer states ^{246}Cm can form. The energy required for the initial deformation of the nuclei can come from a multitude of sources, one such a method is after an initial fission event, leaving one of the decay fragments in this excited and deformed state.

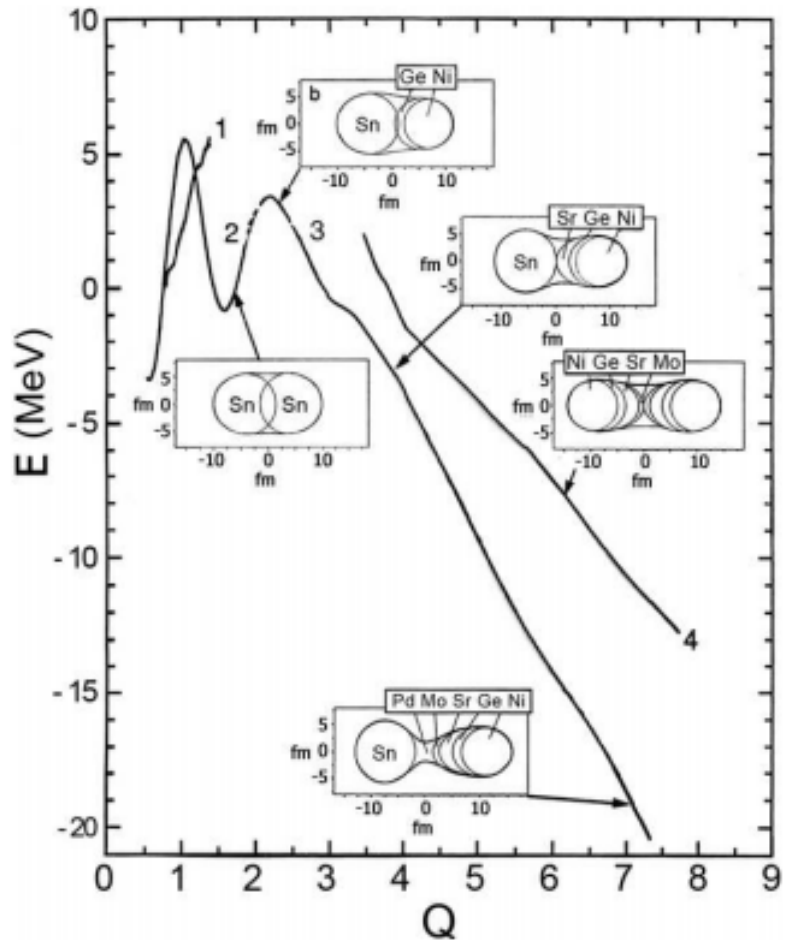


Figure 2.6: The bottoms of the fission valleys as a function of parameter Q (proportional to the quadrupole moment) for ^{246}Cm . The panels depict the shapes of the fissioning system at the points marked by arrows. [31]

CHAPTER 3

EXOTIC NUCLEAR FISSION AND RELATED EXPERIMENTAL METHODS

3.1 COLLINEAR CLUSTER TRI-PARTITION

A new type of ternary decay of low excited heavy nuclei was identified as Collinear Cluster Tri-partition (CCT). This new ternary decay mode was observed experimentally alongside conventional binary fission [1]. The first step in trying to describe this phenomenon was made by Vijayaraghavan and his colleagues in their study of sequential decay processes, their result were however very specific to models they had used and this thus served only as a first step. They calculated different potential energies of various pre-scission configurations leading to ternary decays with similar kinetic energies to those observed in CCT [41]. The next step in from Diehl and Greiner [42] with their work on the energetics of different fission modes. In their work they showed that ternary fission using the liquid drop model in direct ternary fission modes the prolate configuration of ternary fission is more energetically favourable than the oblate configuration of ternary fission. This work put a constraint on how the exact mechanisms for CCT would have to work, forcing it to separate colinearly. Furthermore in [1] it is outlined that there exists a strong link between CCT and various other decay modes, such as cluster radioactivity and cold fission. Similarities in kinematics between CCT and polar emission ternary fission do exist, however experimentally only LCP were observed in polar emission [1]. This discrepancy did not allow CCT to be described as polar emission and thus it was classified as a separate process.

Some of the first experiments described in [43] and in [44], featured some indication of CCT, interestingly one of the decay products in this experiment was a double magic cluster. The particular characteristics of the decay mode make a very promising field of research. Section 3.2 discusses some of the work done investigating this phenomenon.

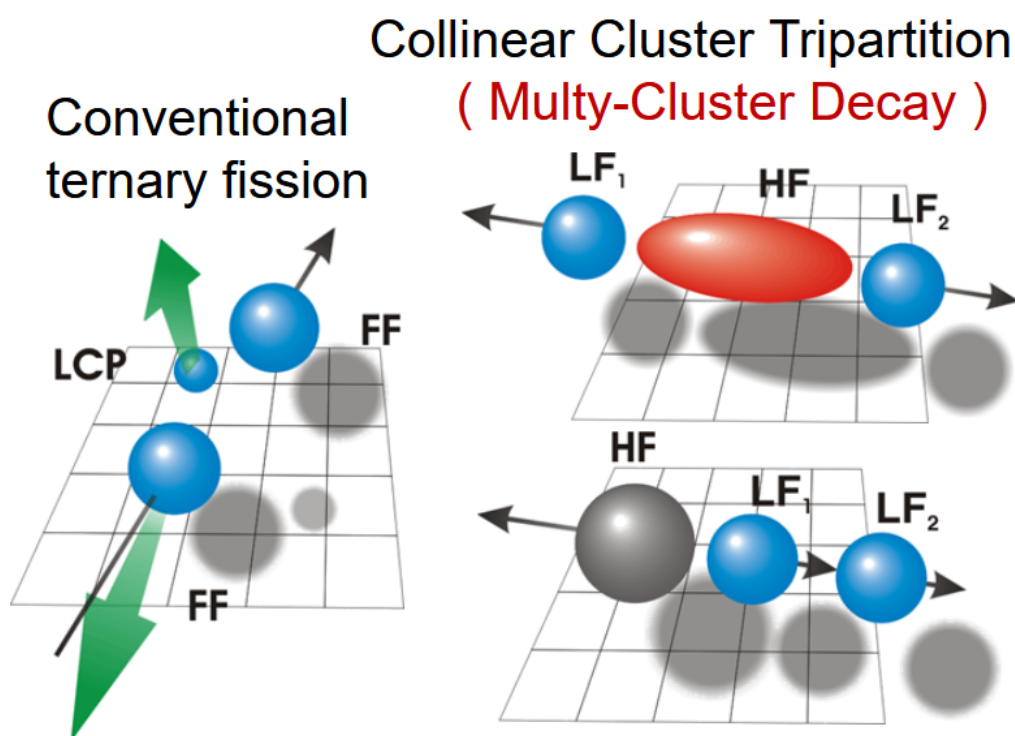


Figure 3.1: Depiction of conventional ternary fission (left) versus. depictions of two different modes of CCT (right) [45]

3.2 EXPERIMENTAL SETUPS AND FURTHER EVIDENCE OF CCT

3.2.1 FOBOS and modified FOBOS spectrometer

The FOBOS spectrometer was installed at the Flerov Laboratory of Nuclear Reactions (FLNR) at The Joint Institute for Nuclear Research (JINR), and was developed to investigate the kinematics of nuclear processes. A schematic view of this spectrometer can be seen in figure 3.2. The FOBOS spectrometer is comprised of three successive shells for allowing for 4π particle detection. These are packed into a detector module shown in figure 3.3.

The inner shell is made up of 30 Position-Sensitive Avalanche Counters (PSAC). These allow time-of-flight (TOF) and positional coordinates (x, y) for detected particles. The second shell a Bragg Ionization Chamber (BIC) attached to the back of the PSAC. The BIC measuring the stopping power of fission fragments as they travel through the gas chamber. The TOF and measured energy from the stopping power are used to calculate the particle mass (accounting for the energy lost by the particle as it enters the detection module is needed). Finally behind the BIC, the third shell of detection consists of scintillating CsI(Tl) detectors, and is used to detect fast moving Light Charged Particles (LCP).

A modified-FOBOS spectrometer was created using the components of the FOBOS spectrometer, with the purpose of providing better data resolution compared to the FOBOS spectrometer. This modified spectrometer featured a new start detector with embedded ^{252}Cf source. A “neutron belt” was also added, consisting of neutron detectors around the outside of the spectrometer. The modified-FOBOS spectrometer is a two arm TOF-E (time-of-flight - energy) spectrometer. A schematic view of this spectrometer can be seen in figure 3.4 and a photo of this setup in figure 3.5. The modified-FOBOS no longer provided 4π coverage, providing only 29% coverage of each hemisphere with each arm, this could be done because of the colinear nature of the decay mode under investigation. This simplified the spectrometer design in addition to creating space for the neutron counters.

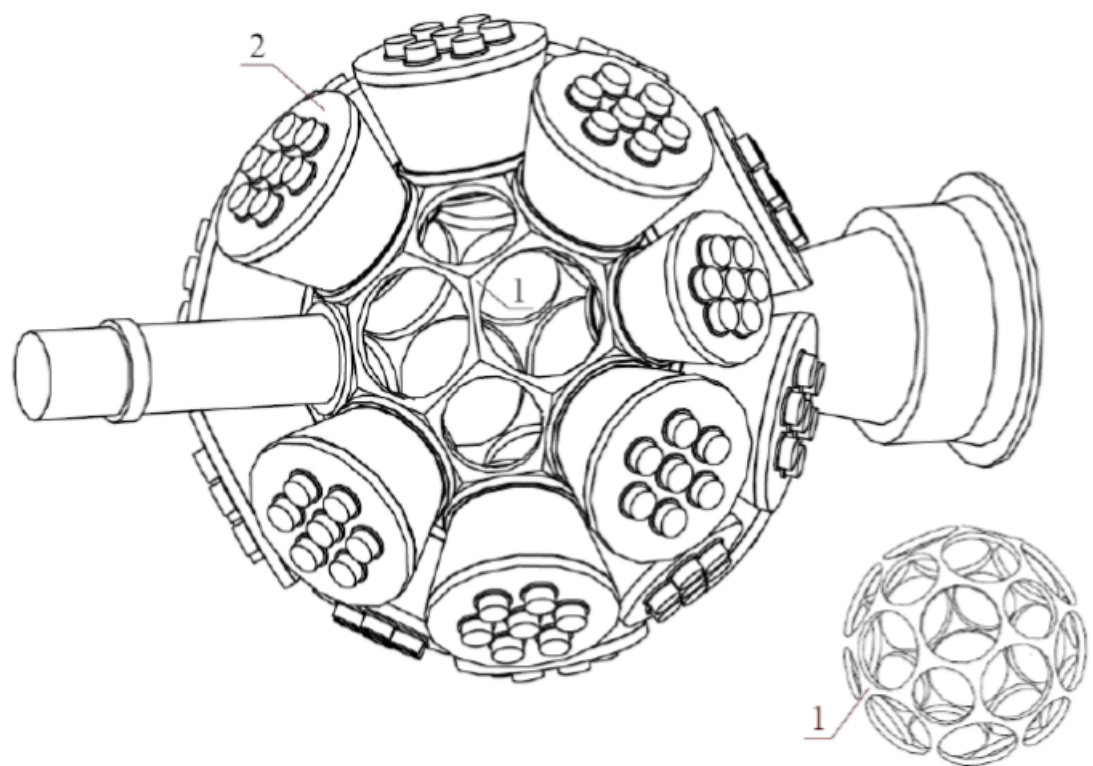


Figure 3.2: Schematic of the FOBOS Spectrometer. (1)-Structural frame. (2)-Detection module [46].

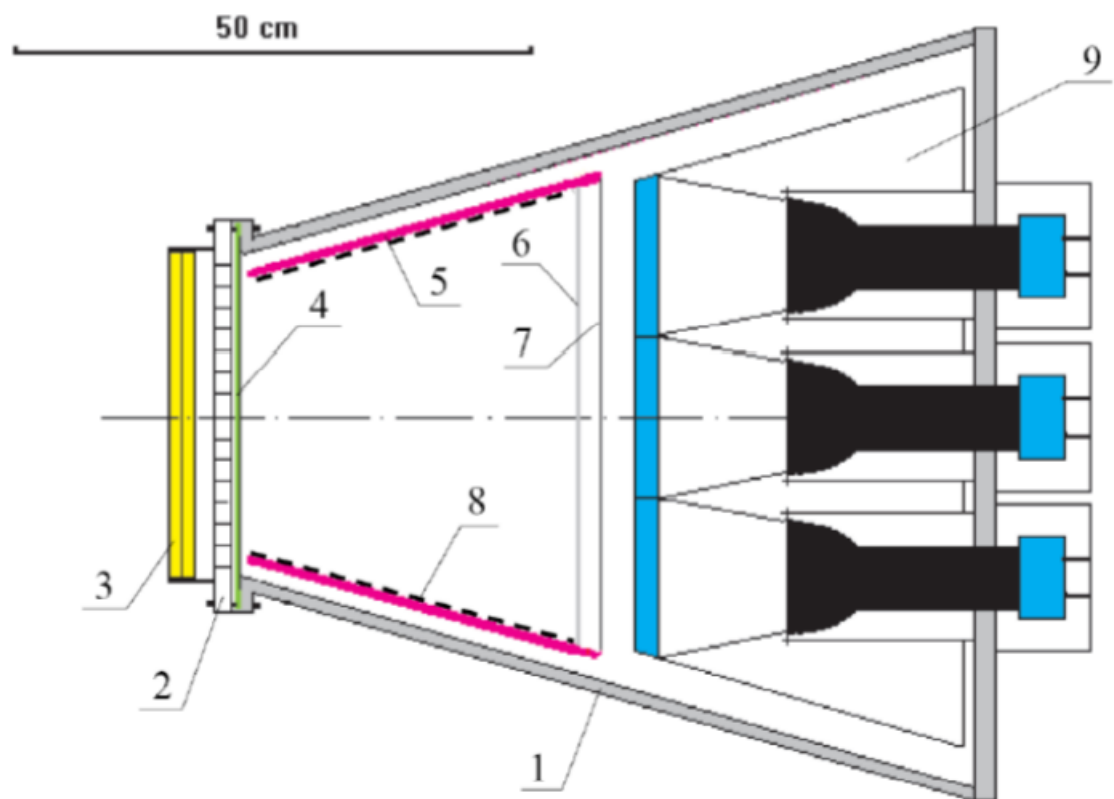


Figure 3.3: Detector module for the FOBOS spectrometer: 1 outer part of the BIC, 2. Supporting grid for the entrance window, 3. PSAC, 4. Thin foil, 5. Teflon cone, 6. Grid, 7. Anode, 8. HV divider, 9. Scintillation shell [46]

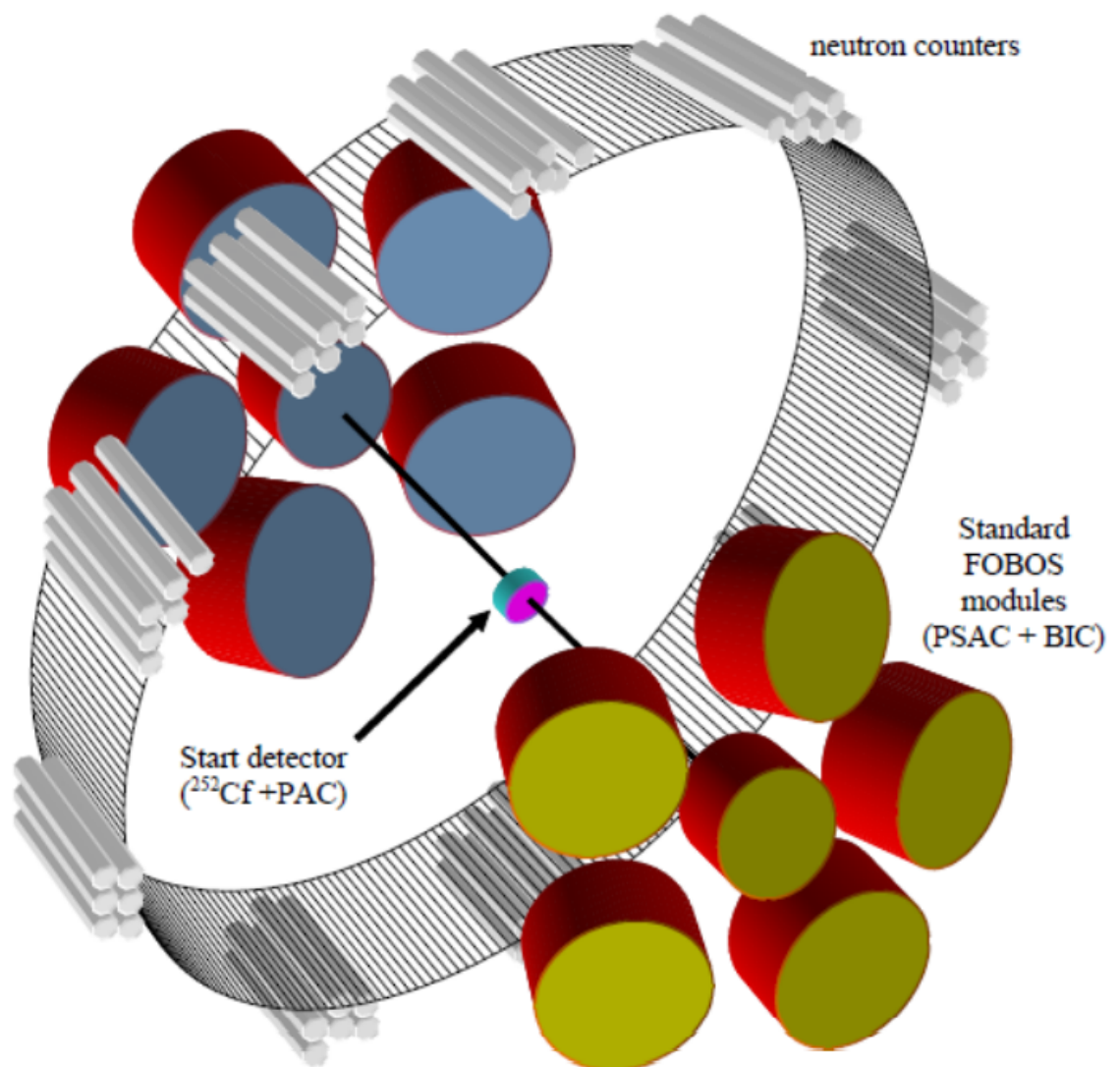


Figure 3.4: Schematic view of the modified-FOBOS spectrometer [46]

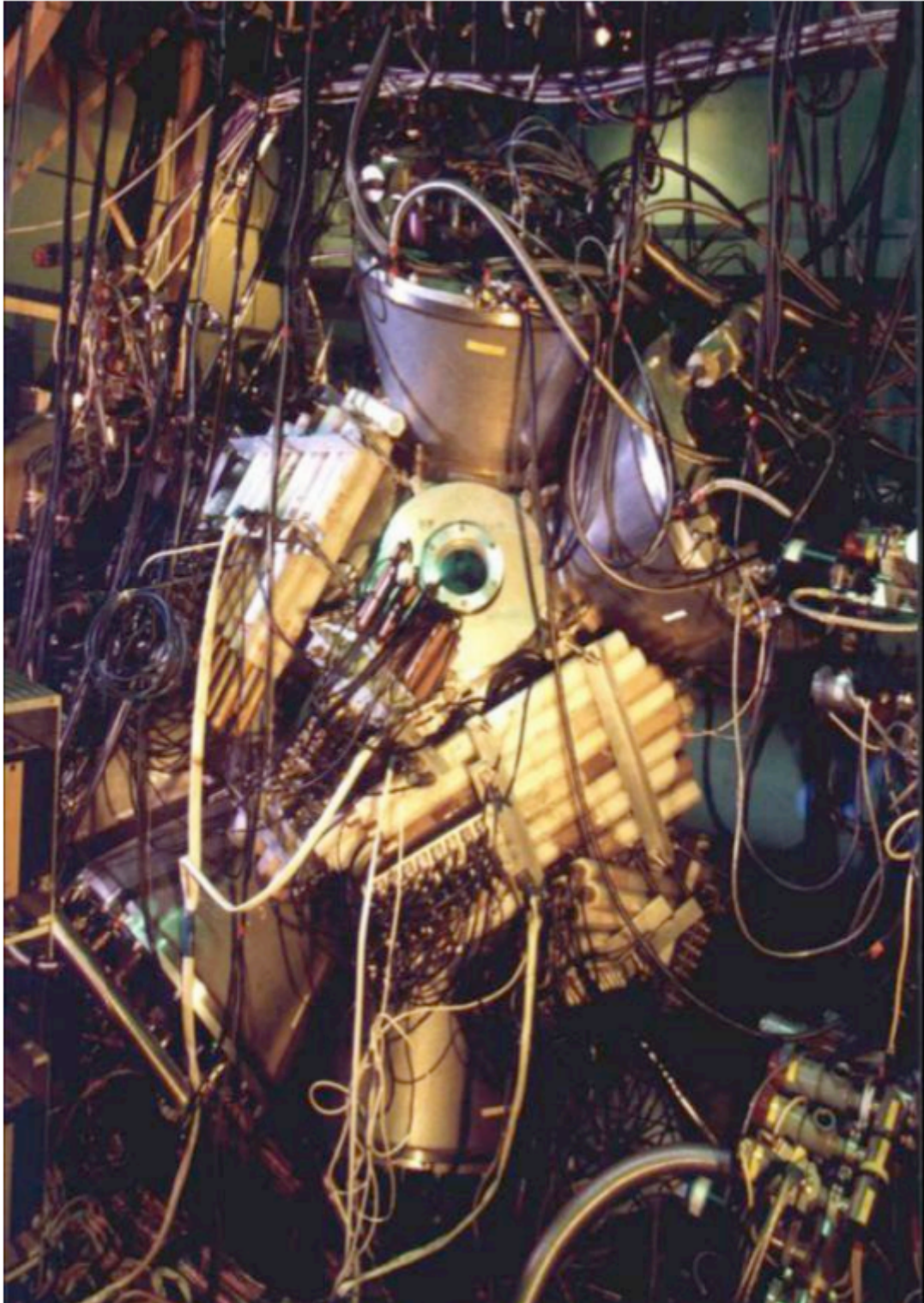


Figure 3.5: Picture of the modified-FOBOS spectrometer [46]

The first results containing the CCT [47] decay mode was from an experiment done with the FOBOS spectrometer. Figure 3.7 from [1], [26] is from subsequent experiments performed. It is a mass-mass distribution of detected fission fragments (ffs) from the spontaneous fission of ^{252}Cf . The particular setup used is shown in 3.6.

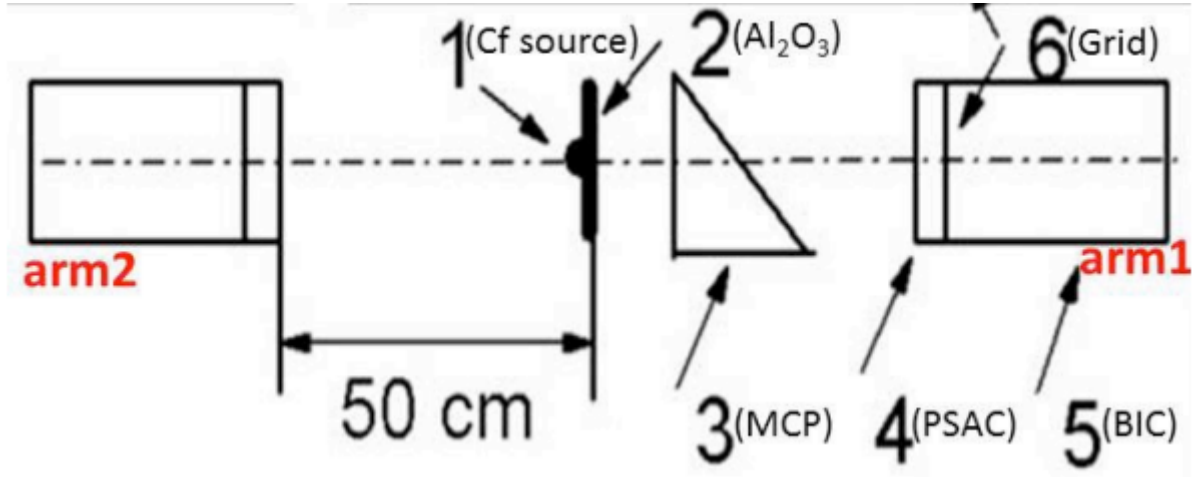


Figure 3.6: Diagram of the modified-FOBOS spectrometer setup, note that source has a thin Al_2O_3 backing in “arm 1” [46]

In figure 3.7: M_1 - Mass of the particle detected in arm 1 this side contains the source backing of Al_2O_3 , M_2 - Mass of the particle detected in arm 2. The numbered features 1 and 2 contain events produced by conventional binary fission. Features 3, 4, 5 and 6 consist of events scattered from the source backing and a grid placed in front of the PSAC detector of arm 1. This grid also accounts for the count rate difference in regions 3 and 4.

The region marked by the arrow 7 was to be the main breakthrough in revealing the existence of the CCT decay mode. This feature is explained as follows: If ternary fission occurs, two lighter fragments travel down arm 1 and are scattered by the source backing at a very small angle. One of these particles will hit the grid while the other is detected. The mass of this missing particle Ni was named the “Ni-bump”. If the two lighter particles travel down the other arm of the spectrometer both would be detected and counted as one big fragment, thus being indistinguishable to binary fission.

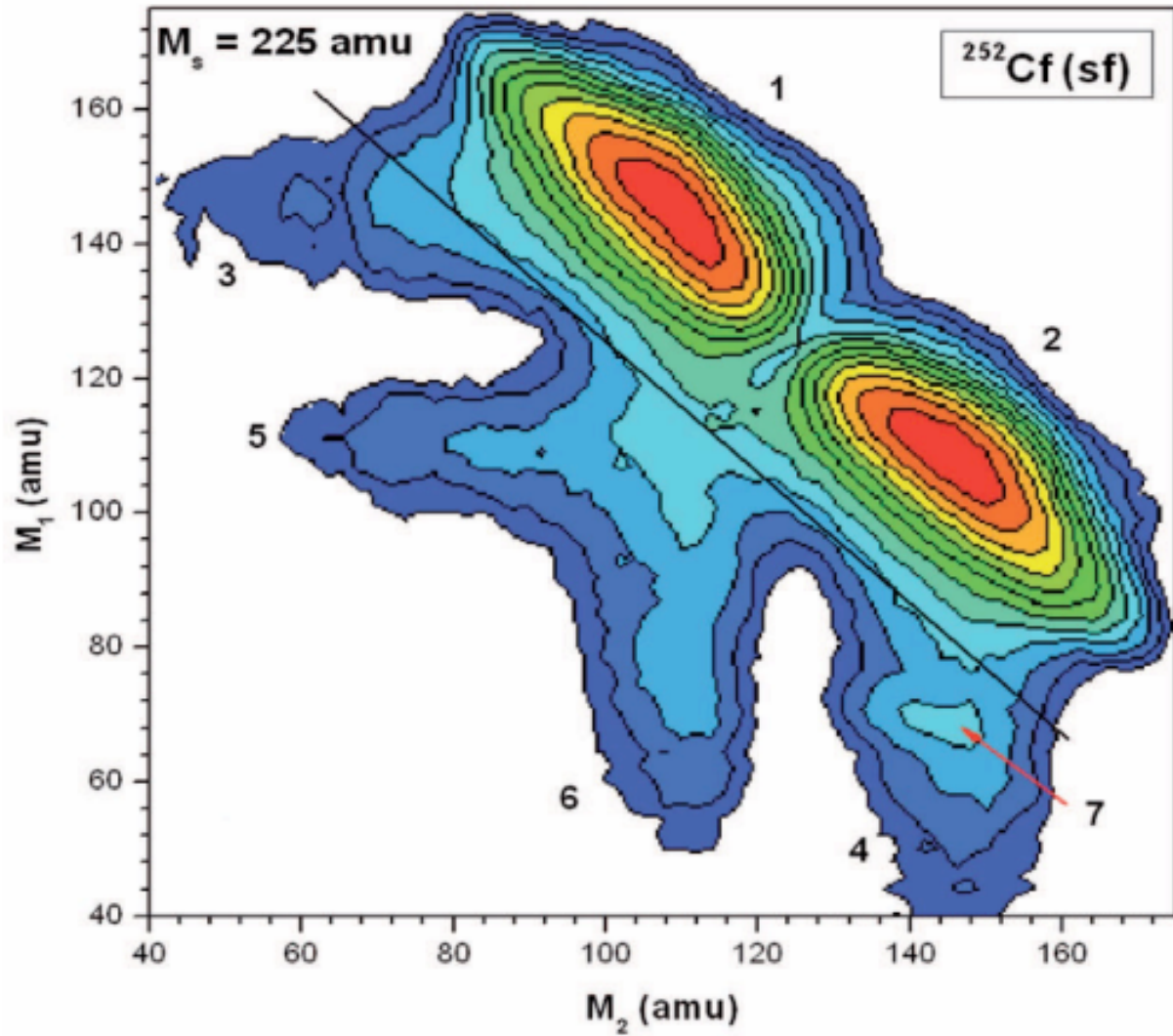


Figure 3.7: Contour map with the mass-mass distribution of the collinear fragments detected in coincidence from the two opposite arms of the FOBOS spectrometer setup. [1], [26]

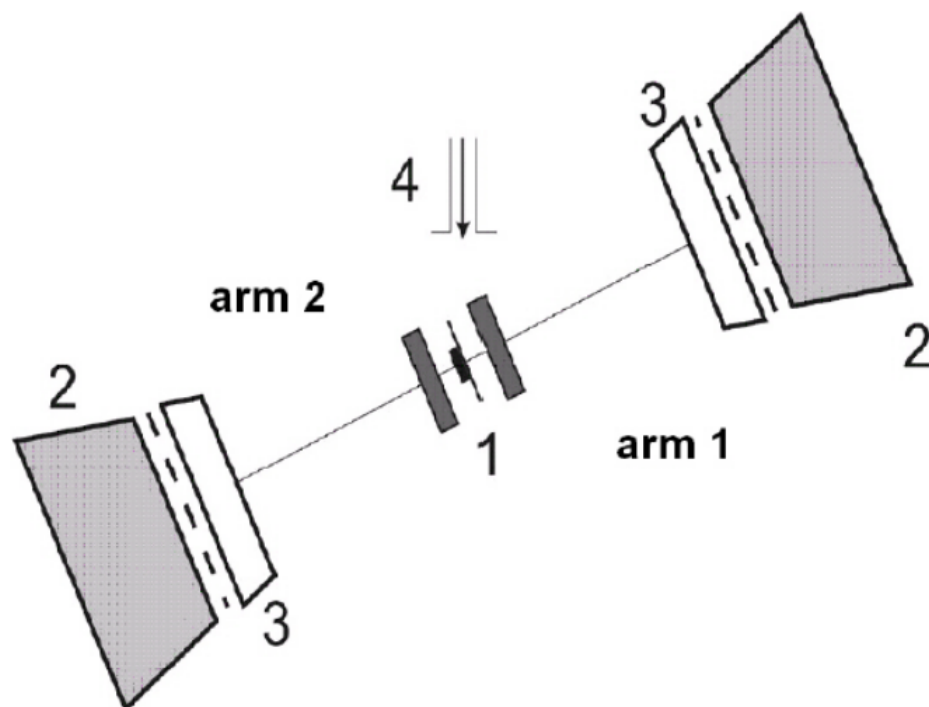


Figure 3.8: Schematic view of the mini-FOBOS spectrometer showing 1-'start' avalanche counter, 2-BIC, 3-PSAC and 4-beam of thermal neutrons [46].

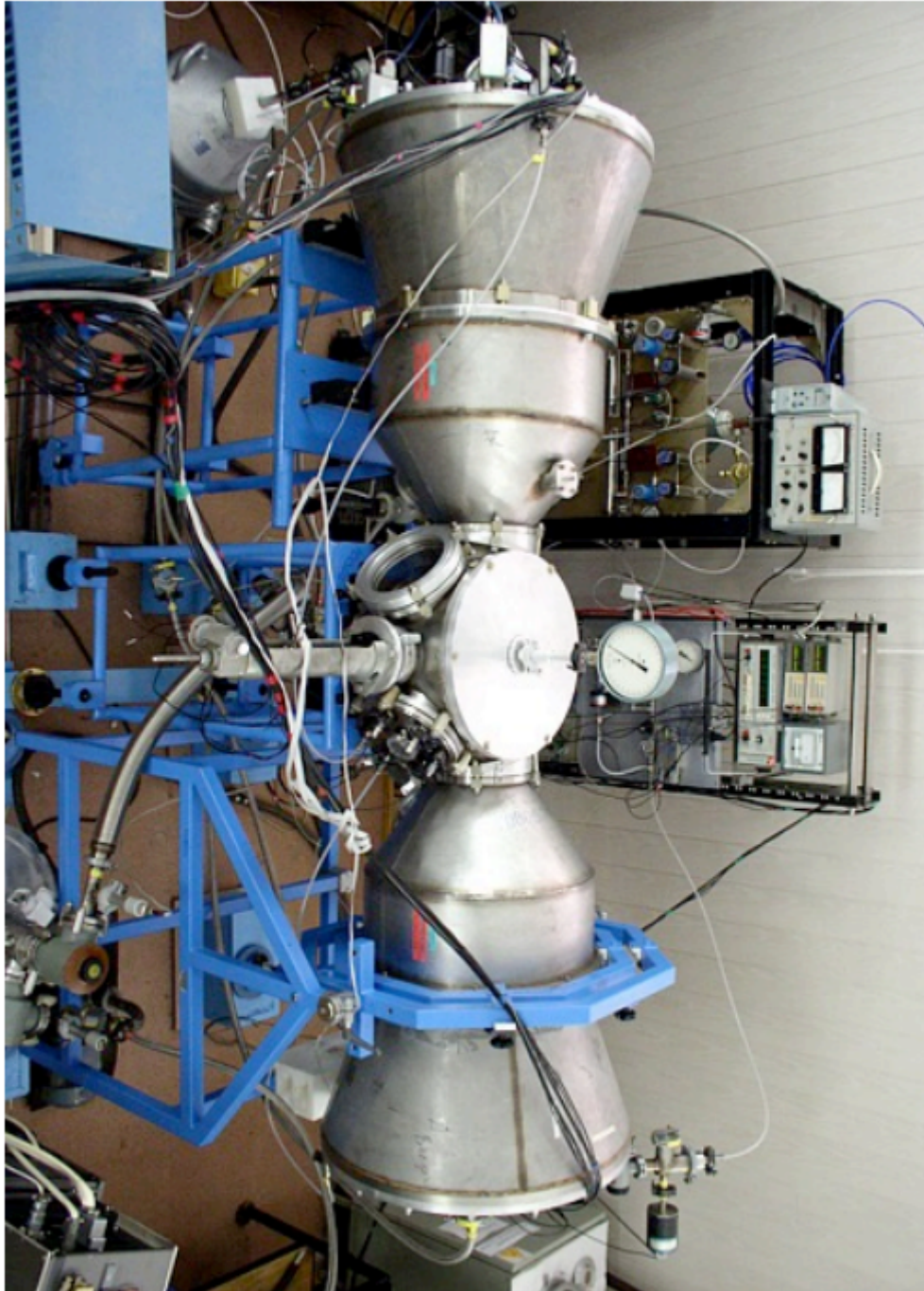


Figure 3.9: Picture of the mini-FOBOS spectrometer.

Subsequent experiments and spectrometers setups were developed to further study this phenomenon. One being the so called mini-FOBOS, to be used in an experiment where the neutron induced fission of ^{235}U was investigated. This mini-FOBOS (figures 3.8 and 3.9) was suitably modified to be used at the IBR-2 reactor in the Frank Laboratory of Neutron Physics at the JINR. Results from this experiment were very similar to those shown in figure 3.7, showcasing this same Ni-bump. Furthermore analysis of the charge of this bump confirmed the identity as Ni. Figure 3.10 is a projection of these Ni-bumps from both the spontaneous fission of ^{252}Cf and neutron induced fission of ^{235}U onto M_1 , clearly showcasing this Ni-bump in both of the experiments. This Ni-bump appears to show the isotopes ^{68}Ni and ^{70}Ni .

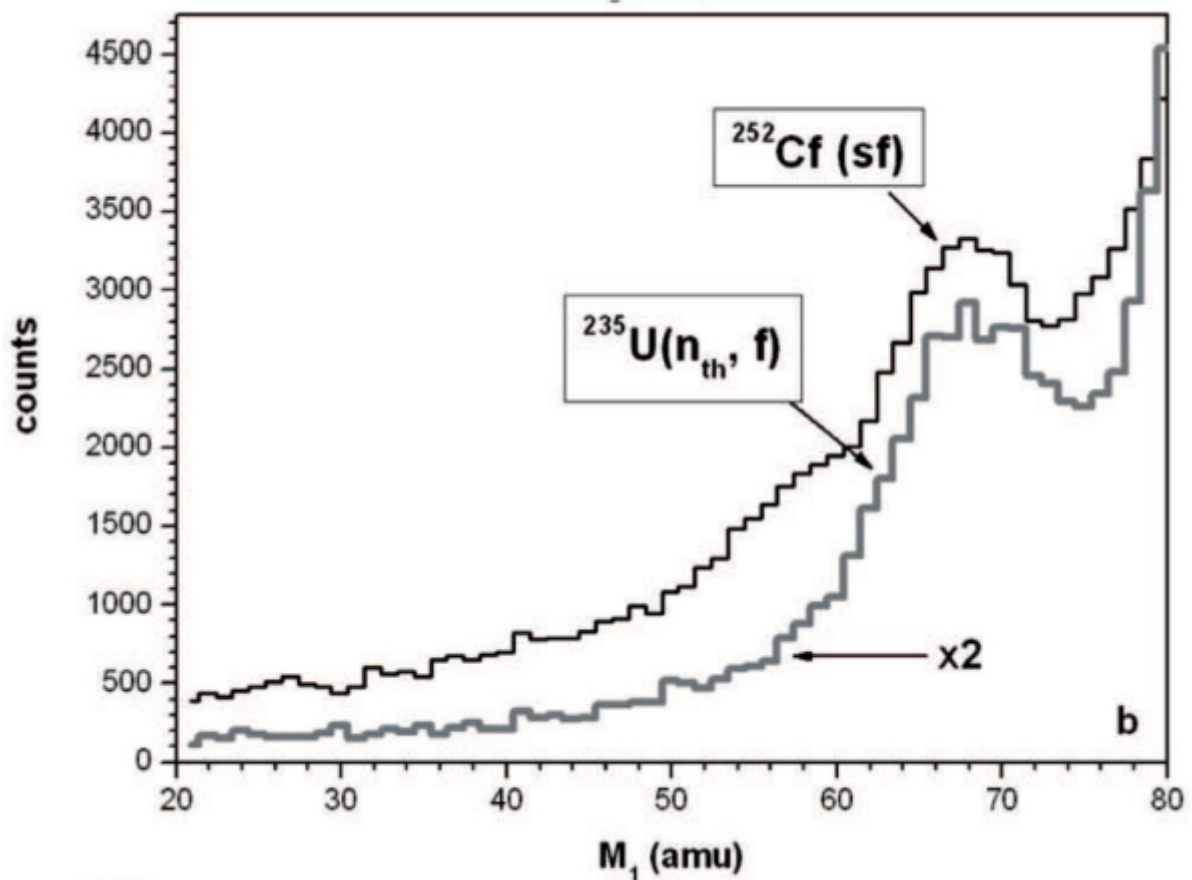


Figure 3.10: Projections of the “Ni-bump” onto M_1 for both the spontaneous fission of ^{252}Cf and neutron induced fission of ^{235}U from [48] and [49].

3.2.2 COMETA

The Correlation Mosaic Energy – Time Array (COMETA) spectrometer was built at FLNR. The design of this setup was first proposed in [50], with the aim of detecting all of the decay products following a CCT event directly. This direct detection of the decay fragments would provide more compelling evidence of the existence of CCT and possibly provide a deeper understanding of the phenomenon. To this end as the name suggests a detector array would be a central part of this spectrometer. A diagram of the COMETA setup can be seen in figure 3.11, showcasing this new array (marked as “4” in the figure) of detectors. This array would consist of 8 PIN-diode detectors (these will be discussed in more detail later in this Chapter), that would provide much higher granularity and positional information. These PIN-diodes in conjunction with the MCP could be used to measure the TOF of the decay fragments, as well as measure the fragments energy. These PIN-diodes had the added benefit of being small and could be placed close to one another. This Spectrometer would also feature a “neutron belt” consisting of 28 ^3He filled neutron counters similar to those in the FOBOS and mini-FOBOS would surround the central chamber. A picture of this setup can be seen in figure 3.12, the white tube bundles are these neutron counters.

Three different measurement can occur depicted in figure 3.13, in all of these one of the three fragment has trajectory marked 1. The other two fragments can have several different trajectories.

The first scenario (1-2-3) is given by particles ending up at positions 1, 2, and 3. Two fragments travel with near-collinear trajectories, with a separation angle $\theta < 1^\circ$, after passing through the degrader (source backing), one fragment (trajectory 2) is detected and the other is not (trajectory 3). Note that a particle that completely misses the detector array also counts as trajectory 3.

Another scenario (1-2-4), can occur if both of the fragments hit the same PIN-diode. This scenario presents some complications when it comes to particle distinction, and will be further discussed in chapter 4.

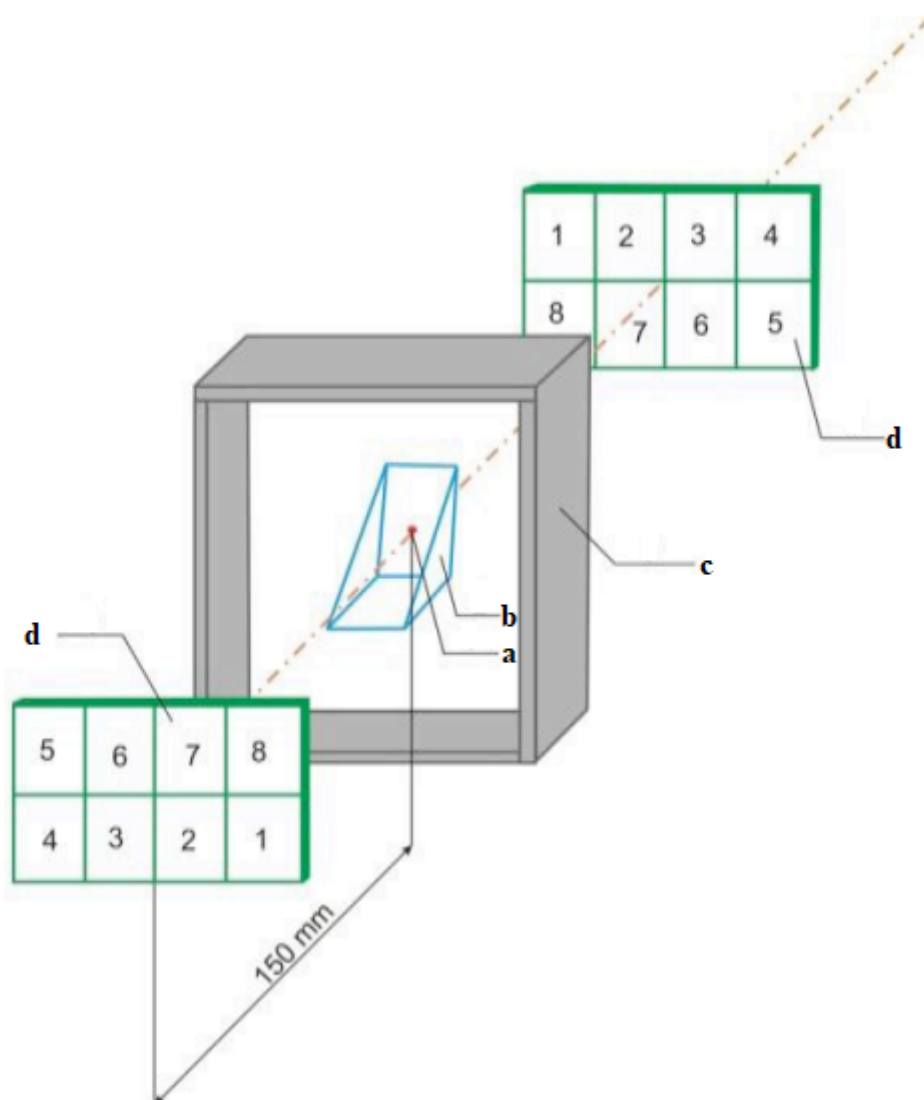


Figure 3.11: Diagram of the COMETA with PIN diodes (d), MCP Time Based detector (b) with ^{252}Cf source (a), and a neutron belt (c) that consists of 28 neutron detectors. [50].

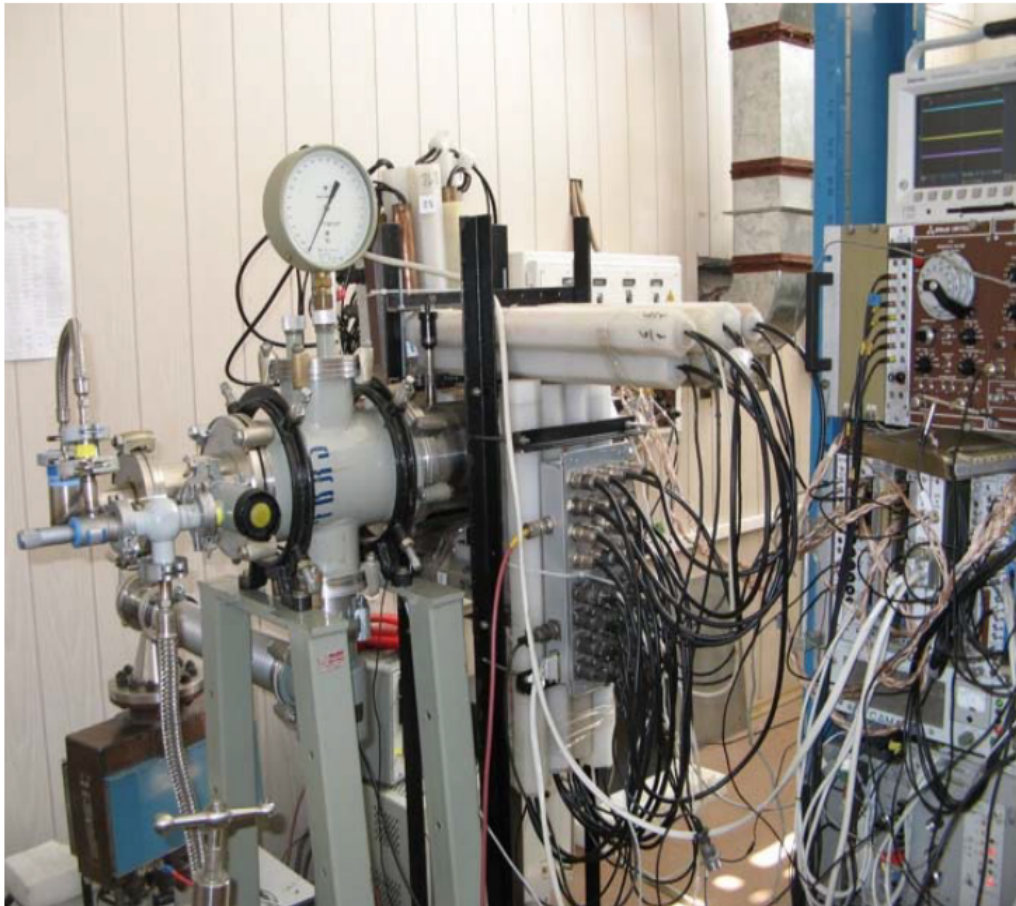


Figure 3.12: Picture of the COMETA setup [50].

Finally the scenario (1-2-5) is the desired one, and corresponds with each of the two fragments hitting a different PIN. For this scenario to occur the separation angle between the trajectories of the two fragments must be $\theta > 1^\circ$. In this scenario detection and positive identification of all three of the fragments would be possible.

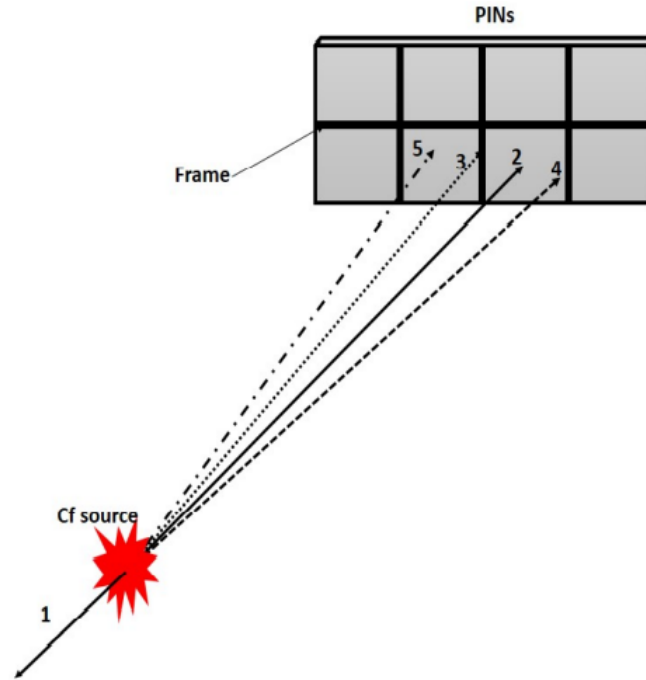


Figure 3.13: Diagram showing the possible configurations of fragments hitting the array of PINs [51].(note trajectory marked “3” hits the array structure and is not detected)

Some of the first results [51] from this spectrometer are displayed in figure 3.14. Showing not only the existence of a Ni magic cluster as a possible constituent of CCT, but also deformed magic clusters of ^{108}Mo and ^{98}Sr .

3.2.3 LIS - Light Ion Spectrometer

The LIS experimental setup consists of two MCP based timing detectors (St1 and St2), and a PIN diode that served for both energy and time registration 3.15. The data acquisition system consisted of the fast digitizer DT5742 and a desktop computer. The two MCP detectors allow an accurate measurement of the TOF of an ion, while using the PIN-diode to simply measure the energy of the ion. This has the

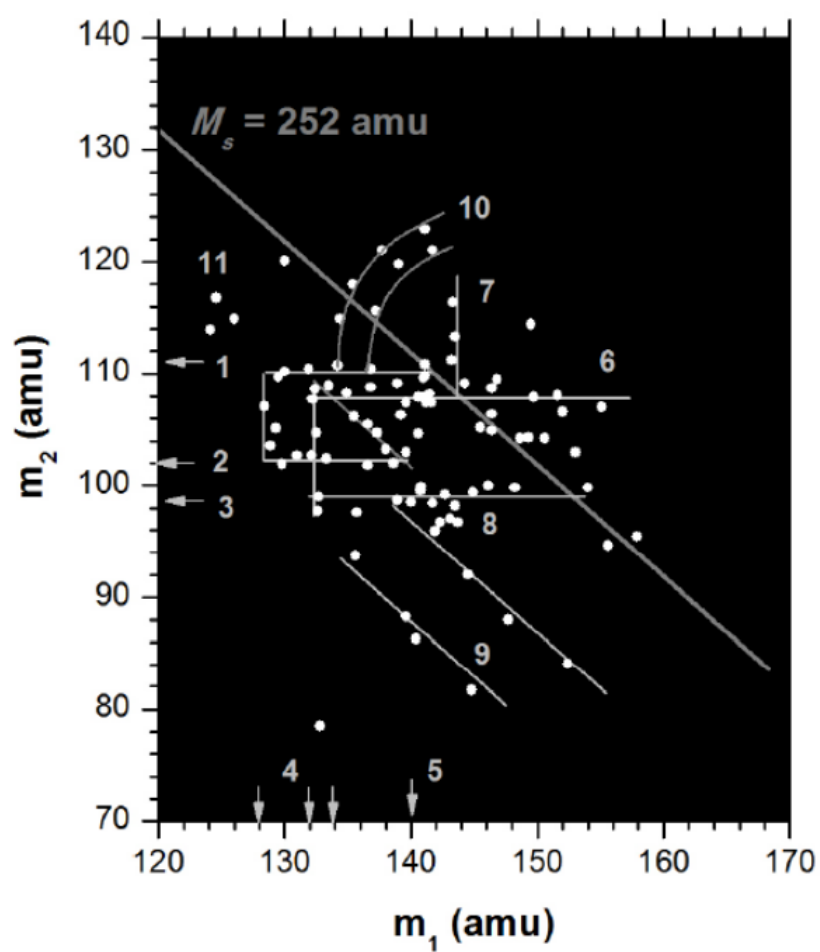


Figure 3.14: Mass-mass distribution of the two heavier CCT fragments. Each data point represent three individual fragments registered, with the condition $m_1 < m_2 < m_3$ [51].

benefit of not having to compensate for the Plasma Delay effect (discussed later in the Chapter), making it ideal for calibration and characterization tests of various experimental equipment. First proposed along with the COMETA setup in [50] with the purpose of verifying the mass reconstruction procedure needed to accurately measure the mass of a particle detected by a PIN diode. This mass reconstruction procedure is needed because of the phenomenon known as Pulse-Height-Defect (PHD), causing lower than expected energy recordings of heavy charged ions in semiconductor detectors, discussed later on in this Chapter. Note that the name “Light Ion Spectrometer” does not mean it can only be used for light ions.

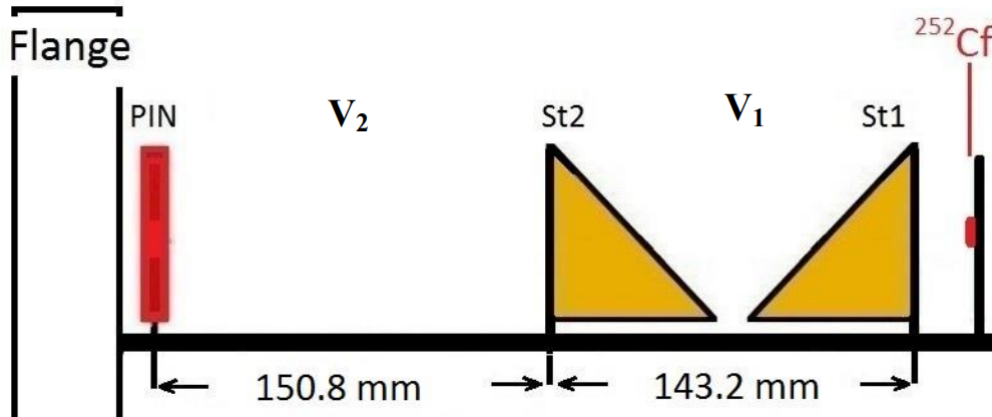


Figure 3.15: Layout of LIS spectrometer.

Further research into CCT proposed that the mechanism behind CCT involved fission shape isomer[52], whereby an original excited nucleus such as ^{252}Cf undergoes fission, splitting into two daughter fragments. One of these fragments would be highly deformed and in a shape-isomeric state, this deformed fragment would then undergo Rutherford break-up upon passing through a thin degrader. This thin degrader usually being the source backing. Because of how close this degrader is to the source, measuring the lifetime of this deformed fragment was not possible.

3.2.4 VEGA

A new experimental setup was developed [53]. The development and experimentation (discussed further in this section) of the VEGA spectrometer was done during

the same time as the study and write-up of this dissertation. This setup is unique in that it features an Electrostatic Guide System (EGS) between the initial event and the detector array. This EGS consists of a tube with a wire running through the middle. Figure 3.16 is a picture of this setup. An electric current is applied to this wire creating a magnetic field inside of the tube around the wire. Charged particles entering one end of this tube will spiral around this central wire because of the magnetic field inside the tube. The ff then spirals all along this tube and exists the other side, where it enters a mass spectrometer similar to some of the other experimental setups motioned in this Chapter. This dramatically increases the distance the ff traverses before break-up and detection, and therefore would allow a deformed ff in a shape-isomeric state to exist longer. The major benefit of this system is that it increases the TOF but does not reduce the amount of detected events.

Results from a study [53] performed with this experimental setup is shown in figure 3.17, and feature some interesting results.

The lines marked “1” and “2” in Figure 3.17 correspond missing masses of 72 u and 68 u respectively, and are associated ^{72}Ni and ^{68}Ni , both of which are magic nuclei. These fragments manifested themselves as the “Ni-bump” in previous experiments as in [55].

Kinematics of the Ni-bump [54] predicts a prescission configuration of ternary decay looking like those in figure 3.18. Events corresponding to ^{72}Ni and ^{68}Ni are predominantly caused due to the nucleus shape shown in figure 3.18b with the first scission point close to the surface of the Sn cluster, all pointing to ternary sequential decay (CCT). The proposed method for the events measured to occur goes as follows:

Binary fission of the excited ^{235}U nucleus excising in a prescission configuration similar to figure 3.18a occurs, forming a Ni nucleus as the light fragment and a heavier fragment moving in the opposite direction. This Ni fragment is lost while the heavy fragment is caught into the EGS tube. It travels down this tube for 400ns [53] before exiting the other side, passing through the thin foil of the MCP detector, causing break-up. The important conclusion from this as quoted from [53]



Figure 3.16: Picture of the VEGA experimental setup, the elongated flight tube of the can be seen extending from the center to the bottom left of the picture.

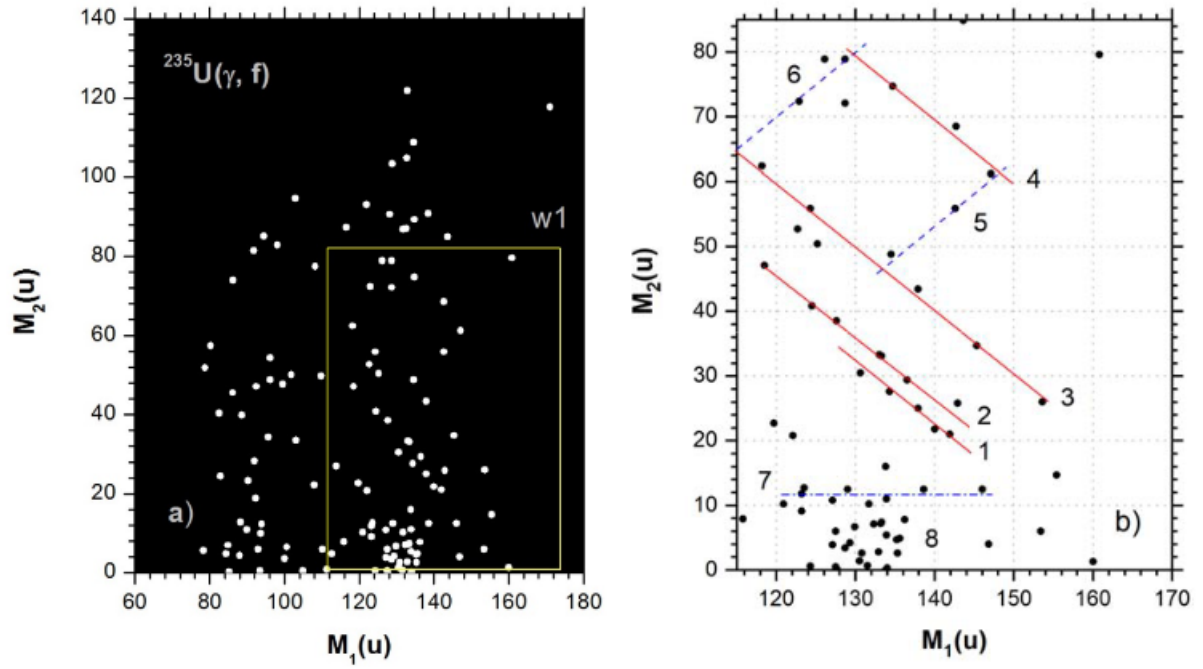


Figure 3.17: Mass correlation distribution for coincidence detected fission fragments in separate PIN-diodes(a) and the data from box marked w1 (b) [53].

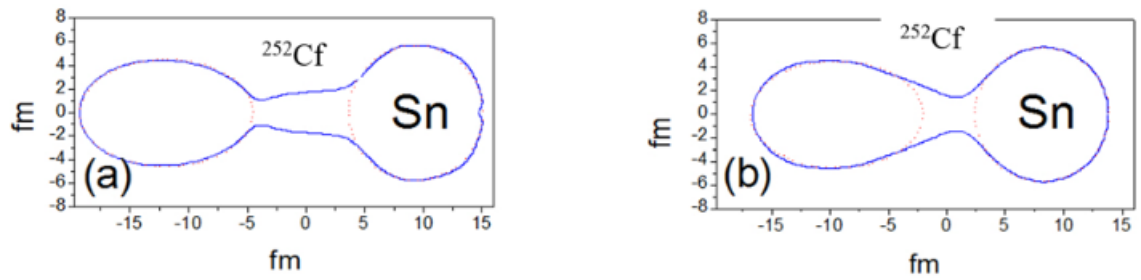


Figure 3.18: Two different fission valleys shapes of the fissioning ^{252}Cf nucleus [54].

is: “the heavy fragment of photo-fission of ^{235}U nucleus is born in the shape isomer state and the life time of this state exceeds 400ns.”.

3.3 EXPERIMENTAL EQUIPMENT

3.3.1 PIN Diode Detectors

The PIN diode detector is a silicon diode that consists of a p-type diffusion layer, an intrinsic region, and an n-type diffusion layer, which is where the acronym PIN comes from. There is a high resistance in the intrinsic region. Figure 3.19 is a diagram of a PIN-Diode showing the three different layers of semiconductors.

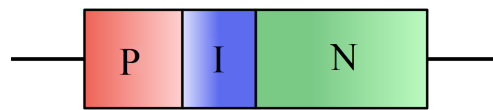


Figure 3.19: Diagram of a PIN-Diode [56] showing the three different layers of semiconductors, p-type semiconductor intrinsic semiconductor and n-type semiconductor

As an ion travels through this detector it deposits its energy, thereby getting slowed down until it is completely stopped inside the detector. Whether or not the particle completely stops depends on several factors, however for the purposes of this study seeing as we detect slow moving ions we always consider the particle to be completely stopped. The energy deposited into the detector disrupts the electric field inside of the detector, and this fluctuation is then recorded, indirectly measuring the kinetic energy of the detected ion.

The size of each PIN diode is $20\text{ mm} \times 20\text{ mm}$ but the working area of the PIN diode is $18\text{ mm} \times 18\text{ mm}$ as the edges of the active surface records incorrect pulseheights, this creates a so called "dead-space" in any configuration which uses more than one of these PINs as part of an array of detectors. There also exists a dead layer on the surface of the Pin, and inside this layer no ionization is produced. The dead layer thickness is $0.01\text{ }\mu\text{m}$. Figure 3.20 is a picture of a PIN diode used in a α spectrometer that was used to verify some measurements done in this study.

3.3.2 Micro-Channel Plate Time Based Detectors

To properly identify the identity of a detected ion inside experimental setups that cannot measure the charge of the detected particle another method or ion identifi-

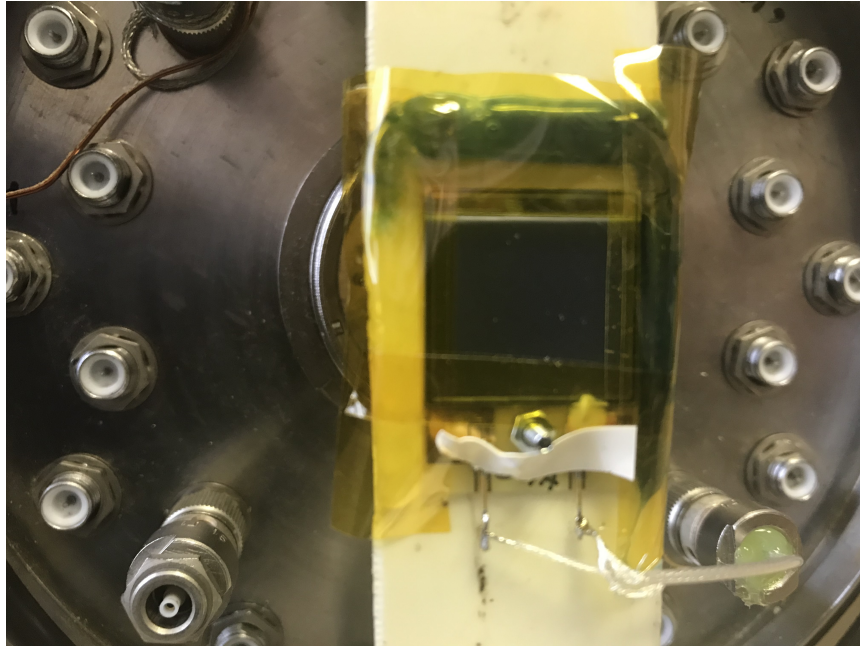


Figure 3.20: Picture of a PIN diode used inside an α spectrometer. The kapton tape is used to shield the border region of the active surface.

cation is required. This method combines TOF (which is used to calculate the ions velocity[v]) and detected energy (the particles kinetic energy[E_k]), and therefore the ions mass (m) can be calculated as $m = 2E_k/v^2$. This however requires a set of two time measurements along the ions trajectory. As discussed the PIN diode completely stops an incoming ion, and in the process records the energy of the particle and a time stamp at which this energy was recorded. This takes care of one of the time measurements and the energy measurement, however we still require another time measurement, that must be taken before this measurement, and in so doing affect the energy of the ion as little as possible. This is very important when working with slow heavy ions ($A \geq 40$) and ($1 \text{ MeV} \geq E/A$) [57] as they very rapidly lose energy. For these purposes Micro-Channel Plate (MCP) electron multipliers are used [58], or for the purpose of this study referred to as a MCP detector (even though in reality an MCP detector is an assembly of many different micro-channel electron multipliers). Figure 3.21 is a schematic view of such a a detector, figure 3.22 illustrates how electrons are multiplied inside the micro-channels and finally figure 3.23 is a photo of such a detector. This detector functions by having the ion pass through

a thin foil, and as it does this it knocks (or drags) electrons out of this foil. A bunch of wires form an electrostatic grid on the side of the knocked out electrons and redirect them towards the micro-channels electron multipliers, which act as an amplifier, creating in a measurable current (signal). This detector indirectly detects the passage of the ion leaving its energy unchanged (This is in reality not true but the energy difference is negligible for the purpose of this study.).

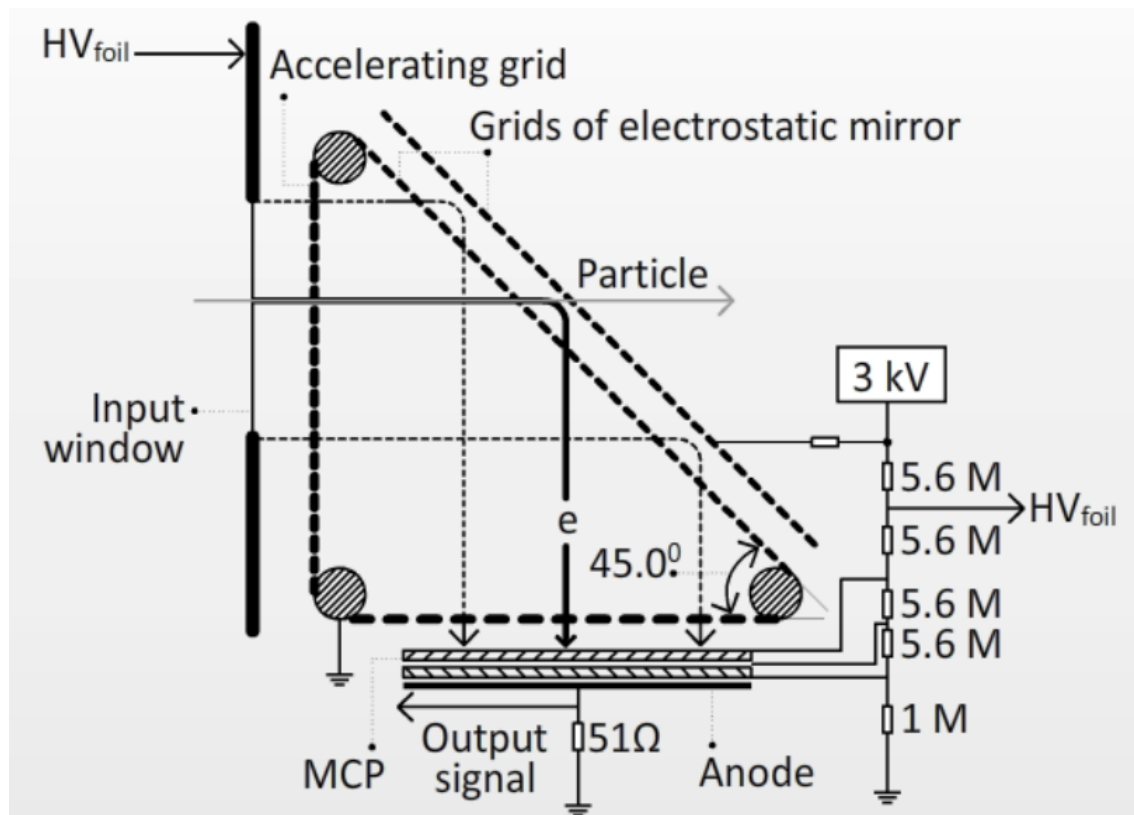


Figure 3.21: The schematic view that shows how the MCP detects the heavy ions passing through via the scattered electrons [58].

3.3.3 The Californium-252 source (^{252}Cf)

This isotope of Californium was first discovered/created in 1950 [59] at the University of California's Radiation Laboratory in Berkeley. The isotope ^{252}Cf is not naturally occurring and has to be produced. This can be done in several different ways such as bombarding curium with α - particles, or more commonly by bombarding ^{249}Bk with neutrons from a reactor ^{250}Bk is formed. This then quickly decays to ^{250}Cf ,

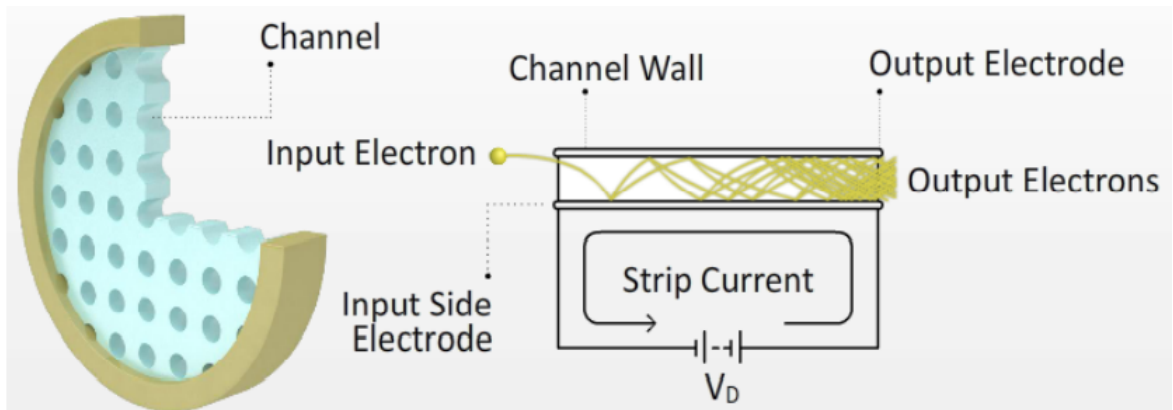


Figure 3.22: The schematic view that shows how the electrons scattered from the heavy ion get detected by the MCP plate of the MCP detector [58].

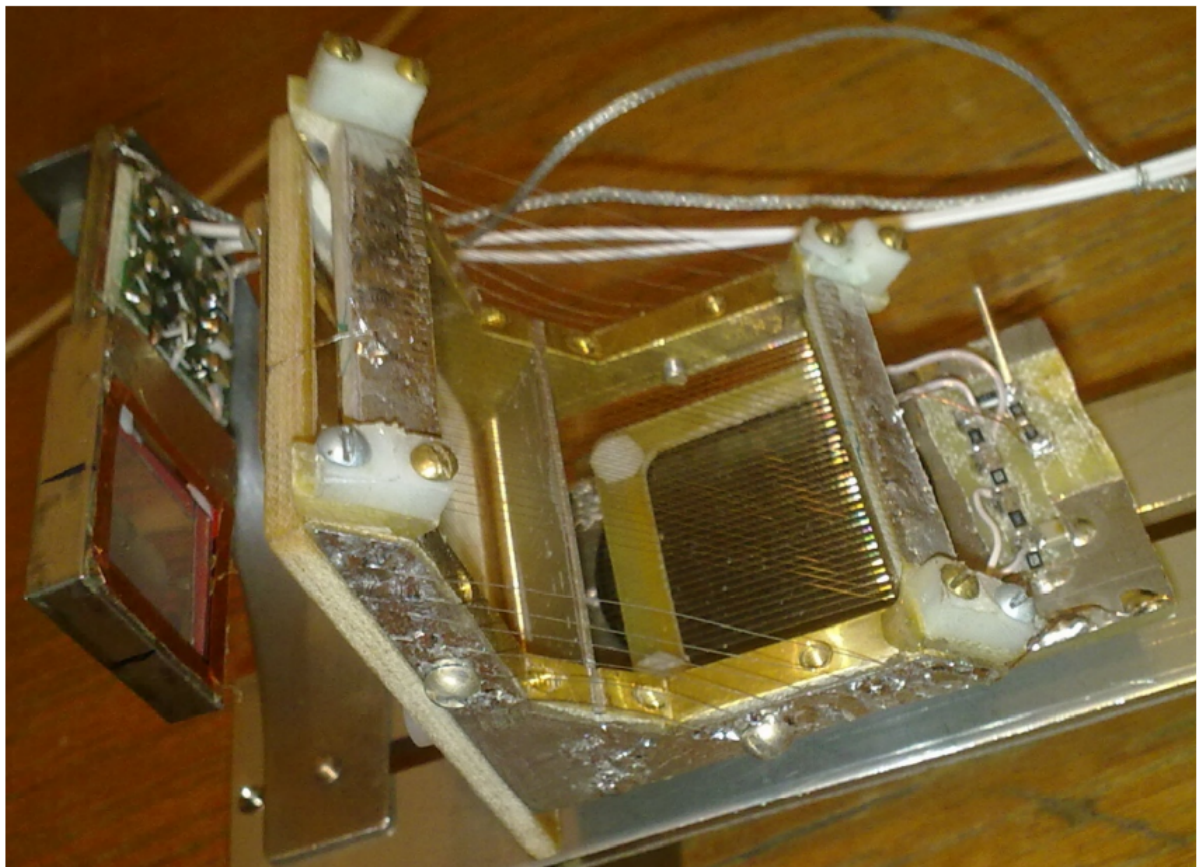


Figure 3.23: Picture of the MCP time-based detector and the PIN diode attached behind the MCP [51].

which when further bombarded with neutrons forms ^{252}Cf [60]. The half-life of ^{252}Cf is 2.638 ± 0.007 yr [61], decaying via spontaneous fission approximately 3% of the time emitting neutrons and via α decay the the rest of the time. It is a strong neutron emitter and is thus frequently used in nuclear reactors to initiate the nuclear fuels neutron induced fission. The relatively high activity rate of ^{252}Cf , the spontaneous fission, and relative safety of this source makes it ideal for use in experiments studying heavy nuclei. There is also no need for a reactor or accelerator to initiate the fission process, simplifying experiments and making them less costly to perform. Finally obtaining this source at the Joint Institute of Nuclear Physics (JINR) in Russia is comparatively easy and inexpensive. Figures 3.24 and 3.25 are pictures of two ^{252}Cf sources.

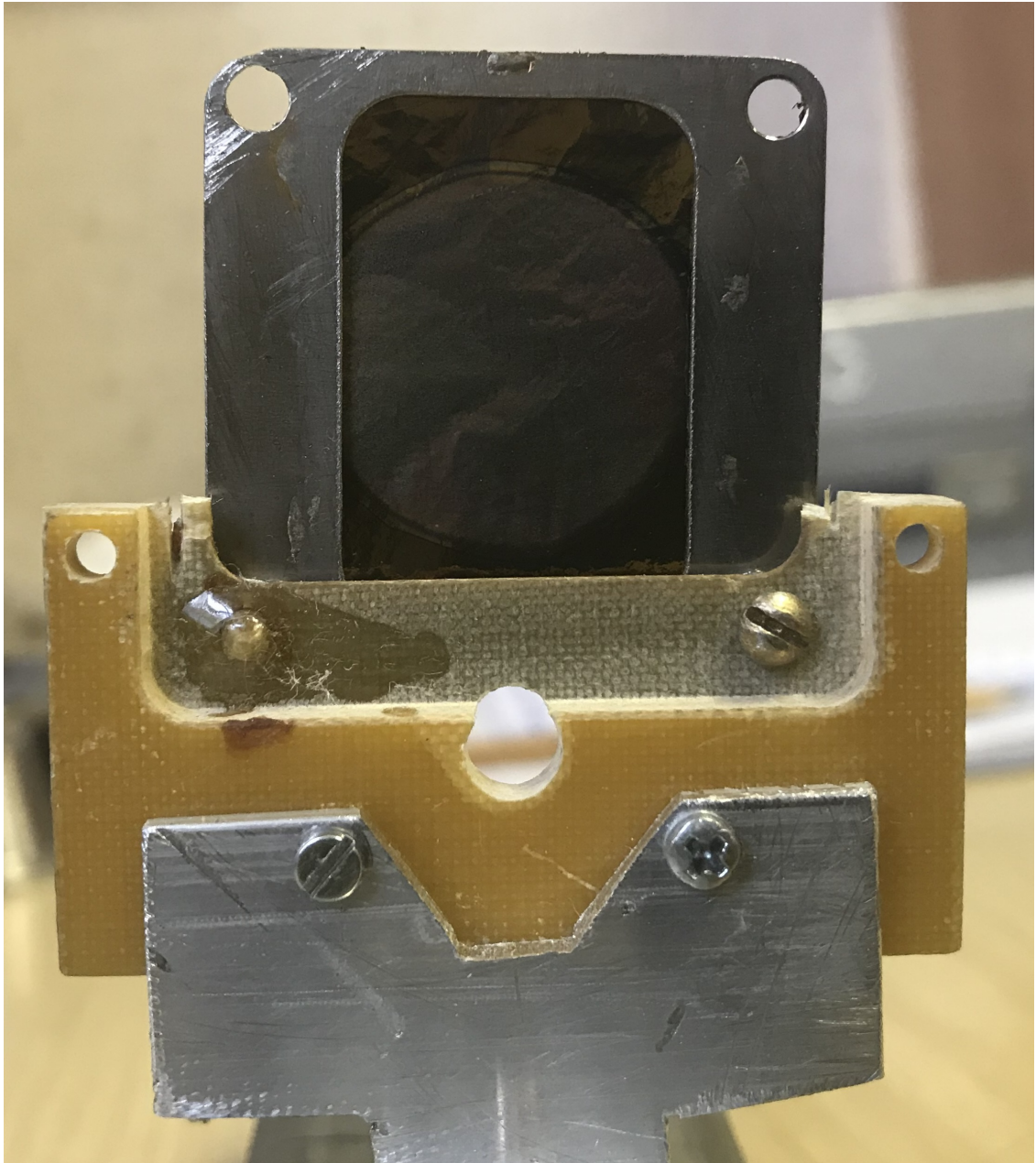


Figure 3.24: A photo of one of the ^{252}Cf sources used in this study, the thin coating of ^{252}Cf on top of the aluminium backing can be seen as the circular disk with a slightly lighter colour.

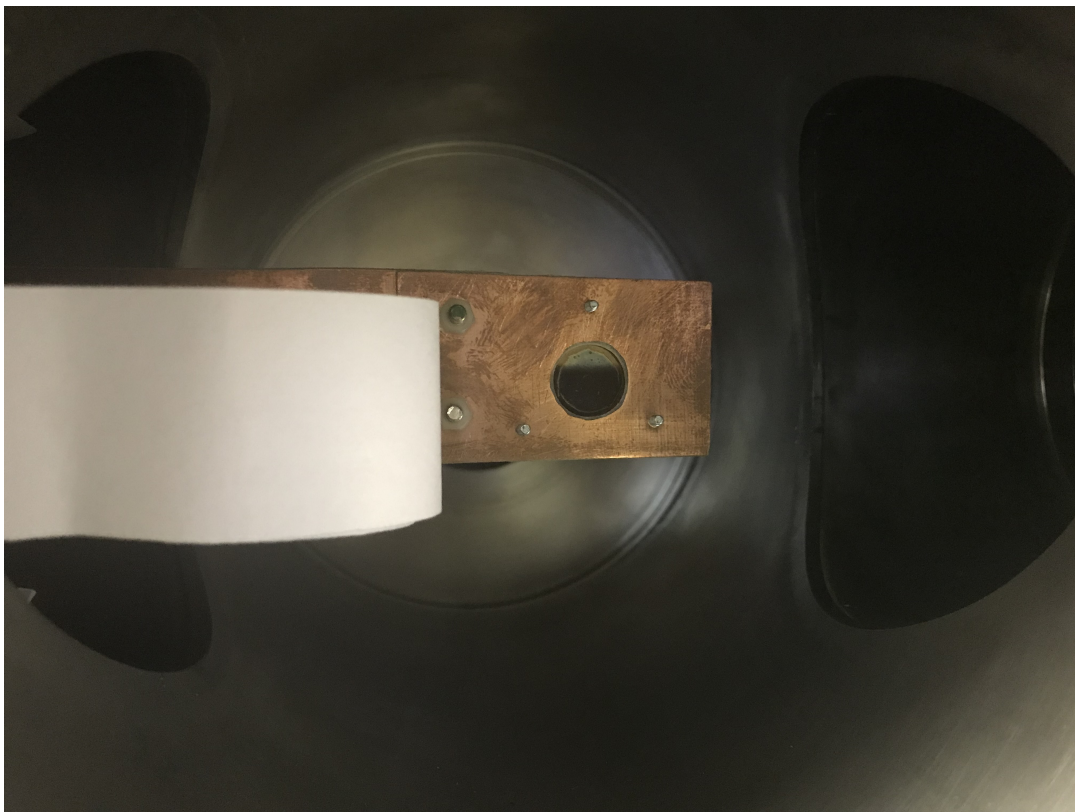


Figure 3.25: Photo of another ^{252}Cf source inside of a vacuum chamber.

3.4 EXPERIMENTAL MANIFESTATIONS

3.4.1 Pulse height defect (PHD)

When a particle hits a semiconductor detector and deposits its energy into the material, the detector registers a pulse. The amplitude of this pulse is proportional to the energy deposited. This pulse height does not behave linearly for all particles and energies. Most notably it affects heavy ions, ex. Fission fragments. This phenomenon is caused by 3 contributing effects the first of which being the “window deficit” (Wd).

Dead layers inside and at the surface of the detector. Bias voltage across the detector can reduce the effective thickness of these layers. Effective thickness can be measured by measuring different pulse height as a function of incident angles. Non linear for heavy particles. The second effect is the so called “nuclear stopping deficit” (Nd), this is due to elastic nuclear collisions between the incoming particle and the material. Recoil nucleus can still cause ionizing effects so not all energy is lost. Probability for elastic collisions is indirectly proportional to incident particle velocity. This effect is fairly well understood and can be calculated.

The final contribution to the PHD is the less well defined “Residual deficit” (Rd). This residual effect encompasses everything else (i.e. $Rd = PHD - Nd - Wd$). It is believed to be mainly caused by electron hole recombination in the plasma column produced as the heavy deposits energy into the material along its trajectory. This effect is dependant on multiple factor such as:

- Electric field strength across the detector, the stronger this field strength the more the material resists this effect.
- Type of detector (type of semiconductor).
- Doping amount and doping uniformity of the semiconductor.

A method was developed to accurately account for this effect in [51], a flow diagram of this can be found in Appendix A. This study will focus on the second experimental manifestation plaguing semiconductor detectors known as plasma delay.

3.4.2 Plasma Delay (PD)

As the particle interacts with the material in the detector and deposits energy into it, it creates high conductivity plasma along the trajectory of the particle. This disrupts the internal electric field F for some time which retards data collection. This effect manifests as a non-linear rising edge in the recorded pulse, i.e. it becomes problematic to accurately determine the exact time the particle hit the detector.

Equation 3.1 was proposed by Neidel and Henschel to model this delay t_p :

$$t_p = 1.33(m^{1/6}E^{1/2})/F \quad (3.1)$$

Here F is the electric field strength applied across the diode, E is energy deposited into the detector and m is the mass of the particle (ion) depositing the energy. This methods accuracy however is inconsistently across different energies and masses.

An improved model was then proposed by W.Bohne *et al* [62] in 1985 shown in equation 3.4 and 3.3. This model is piece-wise defined seperated by the critical electric field strength F_{min} (in kV/cm). This value can be calculated via equation 3.2.

$$\frac{1}{F_{min}} = 10^{-3} \left(\frac{2rM\rho}{E} \right)^{1/2} \frac{1}{d} \quad (3.2)$$

If $F_{eff} > F_{min}$ (region I):

$$t_p = \frac{\bar{Z}^2}{2M} \exp\left(\frac{-E}{3.75M}\right) C \left(\frac{\rho}{d}\right)^{2/5} \frac{1}{F_{eff}} \quad (3.3)$$

If $F_{eff} < F_{min}$ (region II):

$$t_p = t_0 - \text{sign}(d - r') 2.7 \left(\frac{m}{\bar{Z}}\right)^2 \ln\left(\frac{2E}{\bar{Z}^2}\right) \exp\left(\frac{-E}{3.75M}\right) (C\rho)^{1/2} \frac{1}{F_{eff}} \quad (3.4)$$

In equations 3.2, 3.3 and 3.4:

- E (in MeV) is the amount of energy deposited in the detector.

- M (amu) is the mass of the ion that deposited the energy.
- \bar{Z} (in coulomb) is the charge of the ion.
- d (in cm) is the thickness of the detector.
- r, r' (in cm) is the range of the ion in Si(if the ion passes through the detector: $r = d/2$!).
- ρ (in Ωcm) is the resistivity of the detector.
- C (in pF) is the capacitance of the depleted detector.
- $t_0 = 2.8 \times 10^{-5} (\bar{Z}/M)^2 C \rho / r^{1.2}$
- F (in kV/cm) is the electric field strength
- F_{eff} (in kV/cm) is the mean electric field strength

From these equations (3.1, 3.3 and 3.4) it is evident that this effect becomes more pronounced as the energy and charge/mass of the detected particle increases, however for light ions such as α - particles this delay effect is negligible. Correcting for this delay is prudent when working detecting heavier ions. Notably is the effect of the field strength F across the detector. As expected the stronger this field the more it resists the impact the plasma trail has, therefore decreasing the PD.

It is therefore imperative to apply high voltage across the detector when performing experiments, and to this end we needed to find the maximum voltage we could safely apply to the PINs without damaging them.

This is done by measuring the Figure 3.26 is a picture of this testing process.

Both of these methods however require an accurate energy and mass of the detected particle to calculate the plasma delay and in turn the true start time. This presents a problem: as discussed earlier in this Chapter, the time of flight (TOF) is used to determine the identity (and in turn its mass) of the detected particle.

Therefore another method is needed to calculate the true start-time of an event when using a semiconductor type detector as part of the TOF measurement. This is one of the core focuses of this work and will be explored further in Chapters 4 and 5.

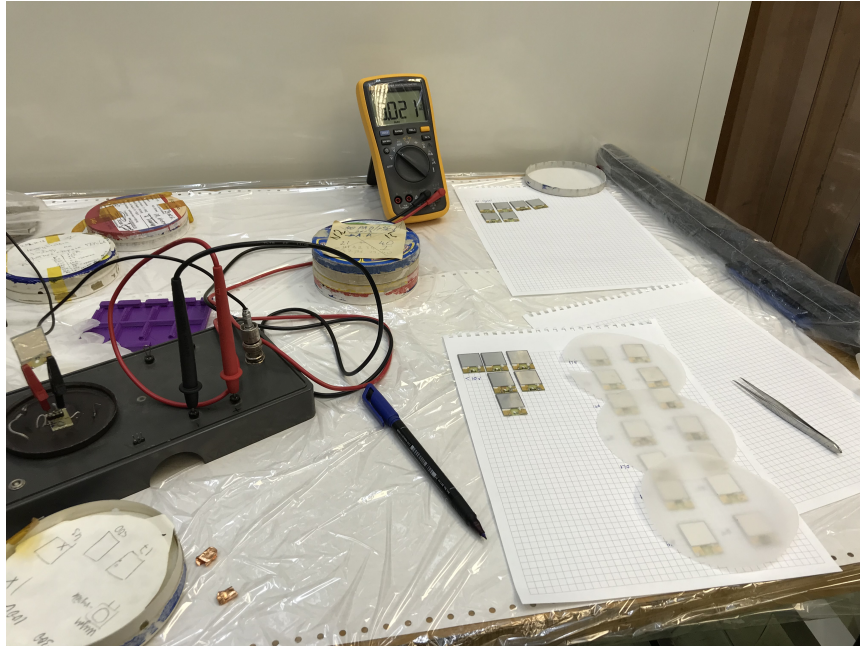


Figure 3.26: Picture showing how PIN diodes were tested inside a clean room to determine their peak working voltage.

The reason we cannot simply always use 2 MCPs as in the LIS setup is a matter of space and detection efficiency. The MCP detector is much larger than the PIN diode, and would therefore increase the distance from breakup to detection. This in turn decreases the solid angle of the PIN diode (end-point detector), decreasing the amount of detected events. Also MCPs are not 100% transparent, so each one added decreases the amount of detectable events.

CHAPTER 4

SIMULATIONS AND DATA PROCESSING

4.1 PROBABILITY ESTIMATION OF DETECTING CCT EVENTS

4.1.1 Goal of this section

When performing an experiment using the missing mass approach with a 2-arm spectrometer, the three particles travel down the two arms, one in the first arm and two down the second arm. Out of the three particles, only two are detected, and then the missing mass approach is used to calculate the mass of the third particle. To detect only one of the two particles the one arm, one of the two particles has to miss the detector array. Figure 4.1 showcases all the possible collision locations for a particle travelling down the arm. Points labelled 1 and 3 either miss the detector array completely (1) or hit the dead boundary layer of the detector array and, therefore, escape detection. Only a particle hitting the active part of the detector array (2) gets detected. So to confirm a CCT event via the missing mass approach in a two-arm spectrometer, two of the three particles must end up at a location 2 endpoint (one in each arm). The third particle must end up at either location 1 or 3.

The reason the third particle cannot be detected is a matter of distinction. Two of the three particles have a similar mass, and are much heavier than the third. This third particle always accompanies one of the heavier particle down one arm of the spectrometer. The two heavier particles have similar velocities, and the lighter particle has a much greater velocity. Therefore to detect all three in coincidence a large data collection timing window is needed. This drastically increases the amount of detected particles, as binary fission still occurs, and therefore correlating the correct pulses to a CCT event and filtering out the unwanted events become a monumental task. These particles can also appear as one bigger particle if the time resolution of the collected data is too low. The simple answer to this would be to detect the two particles in two separate PINs. This however isn't possible because

of the collinear nature of the particles trajectories, this small angle between the particles directions of motion and the short distance between the degrader and the detector array the separation between the particles is still smaller than the inner boundaries of the detector array.

All of this lead to a question on the detection efficiency of this particular setup. Given the detector geometry and setup presented in figure 4.1, what is the probability as a function of the angle between CCT particles that only one of the two particles hit a single PIN diode.

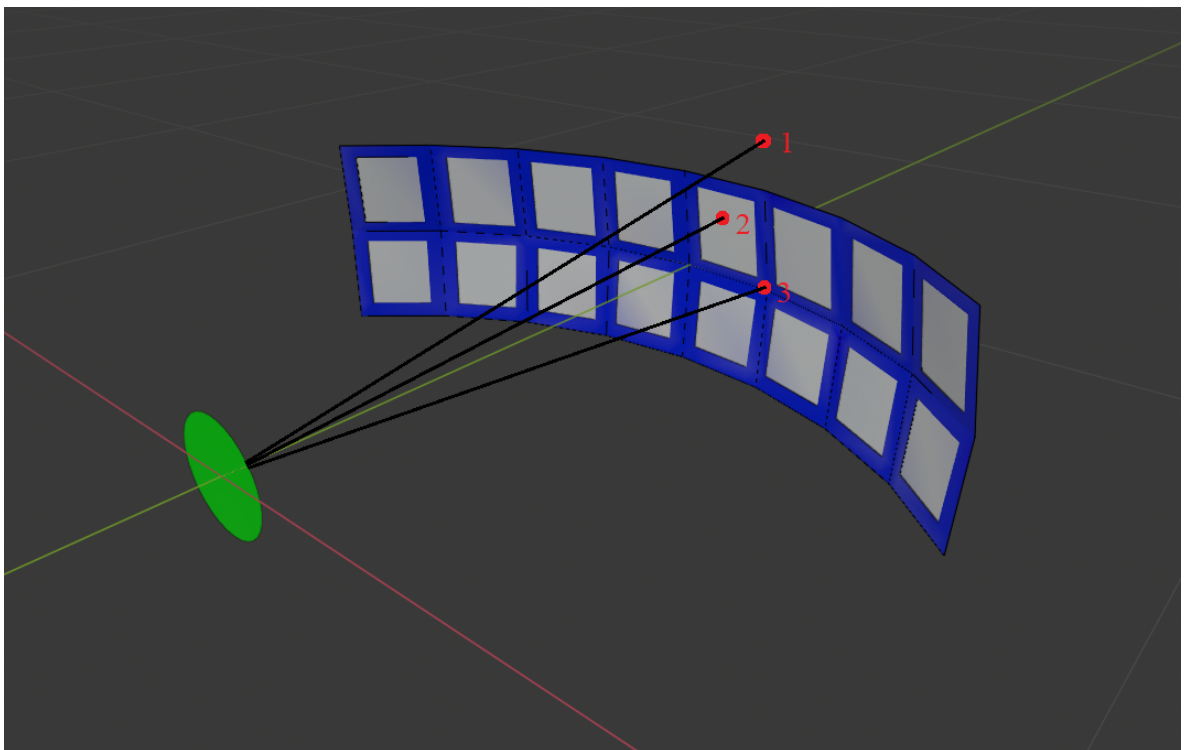


Figure 4.1: Diagram of the curved detector array (160mm x 40mm), with the 3 labeled different possible locations a particle can hit the array, with the black lines serving as examples of particle trajectories. All PIN diodes are 150 mm from the center of the source.

4.1.2 Method to accomplish this

To solve this problem, a Monte-Carlo simulation was developed (see Appendix B.0.1), note: this code was written in the programming language C and runs on

Windows operating system. Particles would be simulated originating at the source that radiates outward isotropically. The kinematics of these particles were then simulated until an endpoint was reached for each particle (either end up hitting the border area, a detectors active surface or missing the array). By counting the outcomes it is possible to determine the probability in the following way.

Particles originate from anywhere on the surface of the green disc (this is the ^{252}Cf target of radius 5mm). As shown from figure 1, there are three different possible locations a particle can hit the array. Position 1 is a particle that misses the array completely, position 2 is a particle that hits one of the active surfaces (14mm x 14mm) of the detector array, and position 3 is a particle that hits the border area between the active surfaces

- Particle locations 1 and 3 both count as a “**miss**” and therefore get assigned the score value of 0.
- Particle location 2 counts as a “**hit**” and get the “score” value of 1 assigned to it.

When simulating two particles, a position on the green disc is randomly chosen as the origin of the two particles. The first particle then gets a random trajectory in the direction of the array. The second particle can then get a trajectory assigned along a cone centred on the trajectory of the first particle. Once both particles have a trajectory, their endpoints can be calculated. You end up with 4 possible combinations: (1,1), (1,0), (0,1), (0,0). Finally define $\#(\mathbf{x},\mathbf{y})$ as the total number of events with outcome (\mathbf{x},\mathbf{y}) . With these terms defined, equation 4.1 describes the probability that we set out to calculate as:

$$P = \frac{\#(1,0) + \#(0,1)}{\#(1,0) + \#(0,1) + \#(1,1)}. \quad (4.1)$$

The events are simulated with some constraints on them. Both particles (in a single event) originate from the same point on the green disc. However, every event has a randomly chosen starting point on the source. The trajectories of the two different

particles in a single event differ by an angle θ .

4.2 DISTANCE DISTRIBUTIONS OF DETECTED PARTICLES

4.2.1 Goal of this section

As mentioned in the theory section, we need two values to identify a particle in a spectrometer arm accurately. These are the particle's velocity and the particle's kinetic energy. With this, one can determine the particle's mass and, in turn, infer the identity. To measure the particle's velocity, we measure the time it takes for the particle to travel a certain distance. This time-difference is calculated by taking the difference in the timestamp from the MCP and the PIN diode detector. The velocity is then calculated by dividing this delta time by the distance between the detectors.

The source in the experimental setup isn't a point source, and as such, the particles originating from it don't all start from the exact location. These particles can also end up hitting the PIN diode at different locations and therefore have flight paths of differing lengths. This presents a question surrounding this difference in path lengths: How much does this path length difference influence the velocity calculation? Which then begs the question: What is the path-length distribution of the particles?

For simplicity's sake, this section will replace the part of the MCP detector with the source itself. This can be done because in the LIS setup the source, and the first MCP are very close to one another. The time of the particles ejection is then set as the first timestamp. Each Pin diode detector used has a flat $1.4 \times 1.4 \text{ cm}^2$ detection (active) surface. The plan was to design a program to calculate the distribution of different path-lengths from a source to a PIN diode. Both the radius ($r = (0, 2.5, 8, 10) \text{ mm}$) of the source and the angle ($\Theta = (90, 95, 100, 105)^\circ$) at which the PIN is placed w.r.t. the source will be changeable parameters. A diagram of this setup can be seen in figure 4.2.

4.2.2 Method to accomplish this

Another Monte-Carlo simulation was developed (see Appendix B.0.2), note: this code was written in the programming language C and runs on Windows operating

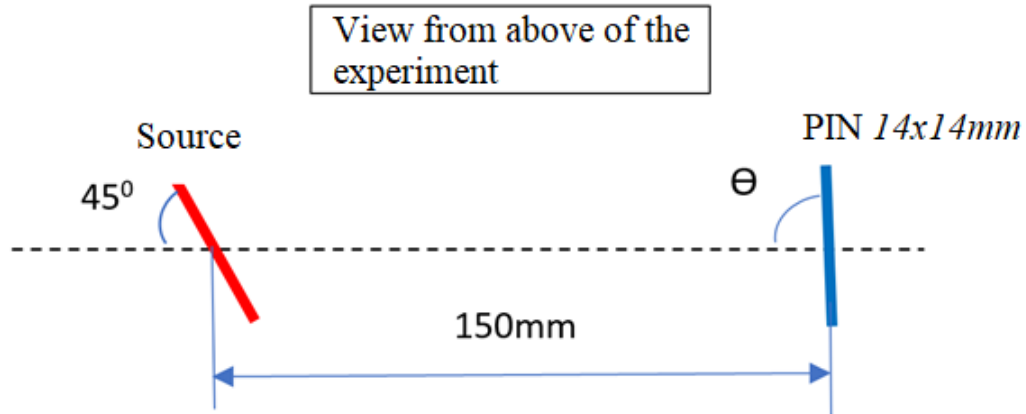


Figure 4.2: Diagram of the setup under investigation.

system. This programme functions via the following criteria:

1. A start point $p1(x1, y1, z1)$ is randomly chosen that lies somewhere on the Cf source of diameter $d = (0, 5, 16, 20)$ mm.
2. An isotropic vector was then chosen for this simulated particle.
3. The endpoint $p2(x2, y2, z2)$ was then calculated, that lies somewhere on the 14x14 PIN with angle $\Theta = (90, 95, 100, 105)^\circ$ (events that missed the PIN were discarded).
4. The distance between $p1$ and $p2$ is then calculated.
5. This process is repeated to create a list of distance values.
6. This list is then sorted into 1000 bins of equal size between the min and max value in the list.
7. These bins are then used to plot the histograms containing the distance distributions.

4.3 NEW TIME-PICK-OFF “PARASPLINE” ALGORITHM

4.3.1 Problem Outline

Experimentally finding the velocity of a particle along its flight-path is crucial, and is typically done by recording when the particle reaches two different locations, a “T1” and a “T2” time. In a lot of our experimental setups the semiconductor PIN diodes are used to measure one of the times. The PIN diode also completely absorbs the particle so it can only be used to record the “stop” time-stamp. When a particle enters the (PIN) detector we measure a pulse (signal), figure 4.3 is an example of such a signal. An output voltage is measured every 200 ps. This voltage amplitude consists of the change in electric field strength across the detector caused by the particle’s impact as well as the noise that is also continuously recorded. Because of the phenomenon known as Plasma Delay (discussed in Chapter 3) the waveform at first could be described as a slowly growing function of unknown form that changes into a nearly linear function as seen in figure 4.3. The start (“T2”) of the waveform is also obstructed by this background noise. The problem therefore is finding a method to accurately and reliably determine the start-time T2 from within the noise (figures 4.4 and 4.5) showcase the noise a little more clearly).

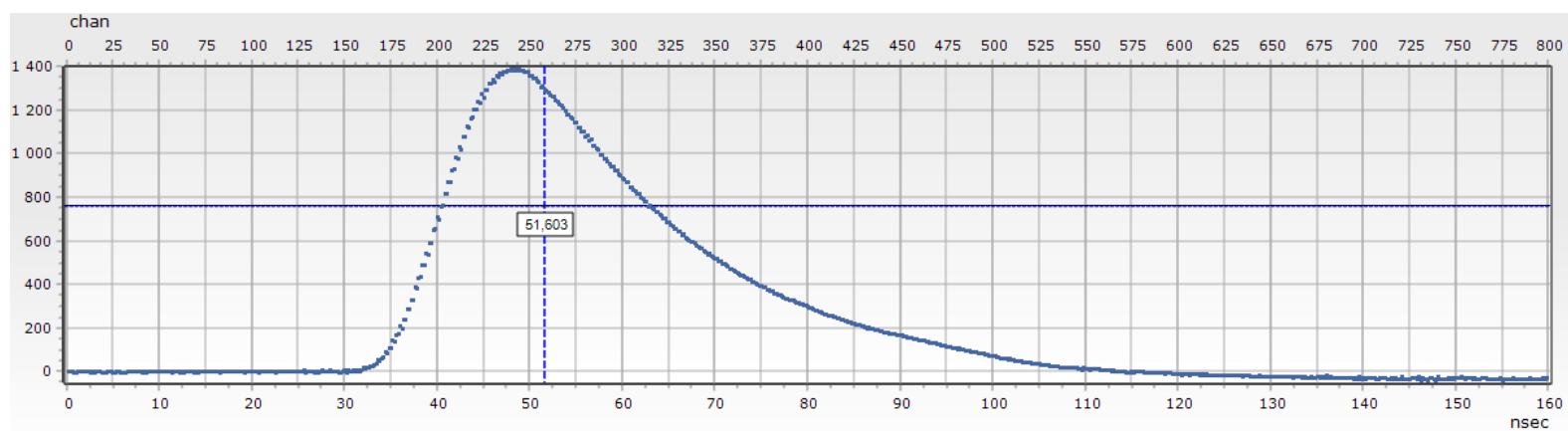


Figure 4.3: Output amplitude(arbt. units) versus time(ns), signal output from a PIN diode after a HCP impacted upon it.

Previously a method known as Parablin [63] was developed and used for this purpose,

functioning by fitting a line to the "linear" part of the pulse, and a parabola to the curved initial rise of the signal. These two functions were then "sewn" together at their intersection by setting the gradient equal to at this point. This method produced accurate results when faced with idealized scenarios, for example if the signal/noise was very large. However this method tended to fail often when working with "noisier" signals, discarding the event. Because of this high failure rate a newer more robust method needed to be developed. This new method would be named Paraspline. This algorithm functions as follows:

By splitting up the signal into two parts. The first of these is the part of the signal masked by the noise in the signal, and the second is the part of signal that can reliably be distinguished, this part will be approximated via a series of splines. Part one will be approximated via a parabola with its vertex coinciding with the start of the signal and lying on the average of the background noise. This is also where the algorithm gets its name.

4.3.2 Paraspline algorithm description

The mathematical work and implementation form [64] is used to develop this programme and is described in the section:

Suppose the set of points $(x_k, \dots, x_n, y_k, \dots, y_n)$ with $k \leq K, n \leq N$, consisting of $K+N$ points, contain the signal we are attempting to analyze. The point (x_0, y_0) is a point in the set that can be realibly distinguished from the noise. All points to the right in the interval $(x_0, \dots, x_n, y_0, \dots, y_n)$ are considered reliable points, the size of N is chosen to be relatively big (usually around $N=180$). The points to the left of this mostly fall in the interval $[y_b - 3\sigma, y_b + 3\sigma]$ with y_b as the average of the noise and σ^2 is the noise dispersion. Firstly we need to fit the best spline approximation of the signal $f(x_i) = y_i, i=1, \dots, N$, on the interval $(x_0, \dots, x_n, y_0, \dots, y_n)$ by means of the following conditions from [64]:

A spline of order q is a function $S(x), x \in [a, b]$, satisfying the following conditions:

- For fixed $x_1, \dots, x_n, a < x_1 < \dots < x_n < b$, called spline nodes, $S(\bullet)$ is a polynomial

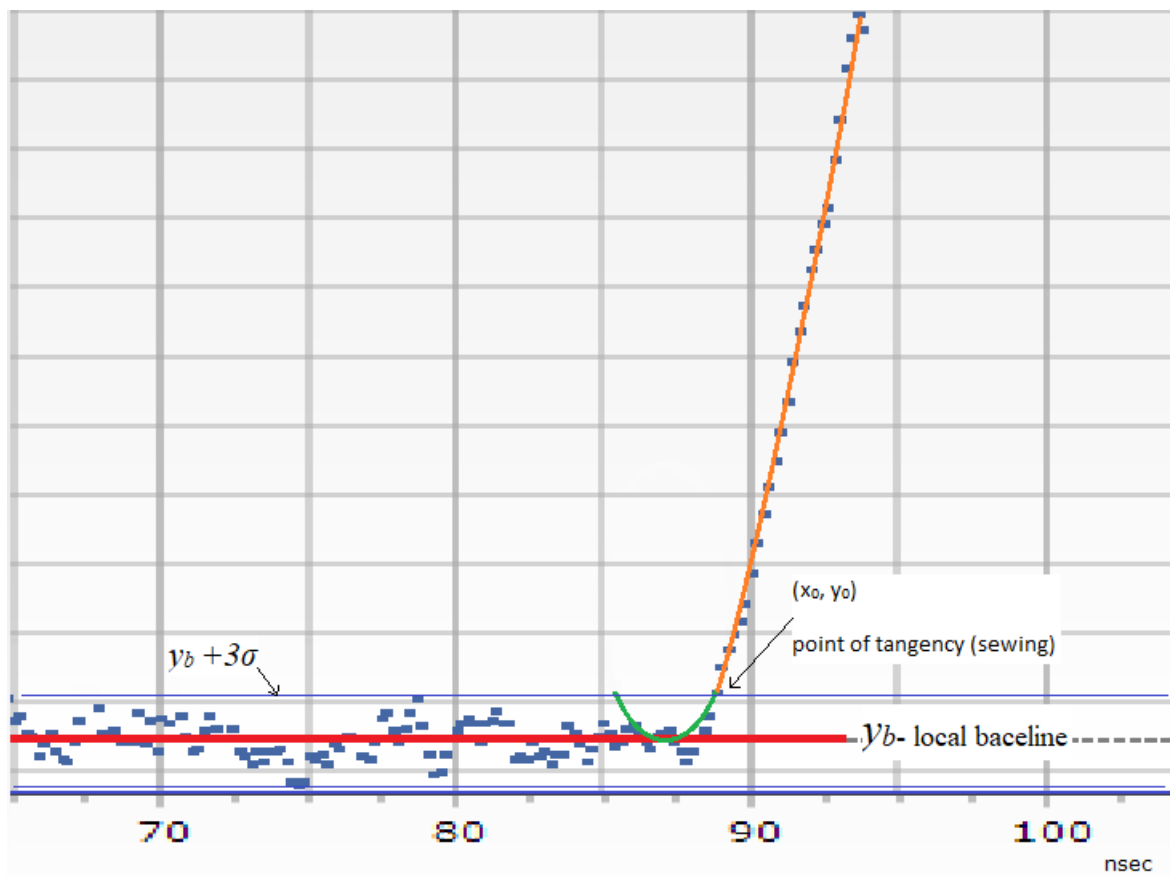


Figure 4.4: Red Line y_b - Local average of the noise, Blue Lines - $[y_b - 3\sigma, y_b + 3\sigma]$ noisy region, Orange - Fitted spline, Green - parabola with vertex at the signal start time.

of degree less than or equal to $2q-1$ on the intervals (x_i, x_{i+1}) , $i=1, \dots, n-1$, where $n \geq q$.

- $s(\bullet)$ is a polynomial of degree less than or equal to $q-1$ on $[a, x_1) \cup (x_n, b]$;
- its derivative of order $2q-2$ $s^{(2q-2)}(\bullet) \in C[a, b]$, where $C[a, b]$ is the class of continuous functions on $[a, b]$; i.e., at the nodes x_1, \dots, x_n the polynomials are sewn by continuity up to the derivative of order $2q-2$: $0 = s^{(2q-2)}(x_j + 0) - s^{(2q-2)}(x_j - 0)$.

We define the smoothing spline of order q as a solution $f(\bullet) = S(\bullet)$ to the following minimum problem (From [64] we know that the minimum problem in equation 4.2 with $n \geq q$ is the only solution for any y_1, \dots, y_n) The smoothness of the spline increases with increasing order q and increasing smoothing factor p .

$$\min \left\{ p \int_a^b (f^{(q)}(x))^2 dx + \sum_{j=1}^n (f(x_j) - y_j)^2 \right\} \quad (4.2)$$

The algorithm work by completing the following two steps:

1. With a fixed value of the smoothing parameter p , we find the smoothing spline $S_p(\bullet)$ of order $q=2$, which minimize equation 4.2 and is the best approximation for signal $(x_1, \dots, x_n, y_1, \dots, y_n)$ (that is, a cubic spline on intervals (x_i, x_{i+1}) , $i=1, \dots, n-1$, $n \geq 2$).
2. The parabola with a vertex on the mean of the signal's baseline (y_b on 4.4) is defined by the following equation:

$$y = ax^2 + bx + \frac{b^2}{4a + C} \quad (4.3)$$

It is necessary to sew the smoothing spline $S_p(\bullet)$ on its left border x_s (at the sewing point) with the parabola defined by the formula 4.3. This joining of the two functions is constrained by having equal value and derivative at the sewing point. And by using these constraints we have two equations for finding the parameters of the parabola a and b :

$$\begin{aligned} ax_s^2 + bx_s + \frac{b^2}{4a + C} &= S_p(x_s) = g \\ 2ax_sb &= S'_p(x_s) = h \end{aligned} \quad (4.4)$$

So we have:

$$\begin{aligned} a &= \frac{h^2}{4(g - C)} \\ 2ax_sb &= S'_p(x_s) = h \end{aligned} \quad (4.5)$$

The anchor point for the parabola $x_p = -b/2a$ (this point was found to be at a certain fixed value of the smoothing factor p). Then for a range of different p smoothing factors, $[p_1, \dots, p_n]$, (usually in increments of 0.01) the program calculates the corresponding splines $S_p(\bullet)$ of order $q=2$ each with the corresponding parameters a , b and x_p for the parabola.

Next we need to find the correct smoothing parameter p and we do this based on Lemma 2 of the article [64].

$$\begin{aligned} f(x_i) &= \sigma(x_i) + \mu_p(x_i) \\ \mu_p(x_i) &= f(x_i) - \sigma(x_i) \\ S\mu_p(x_i) &= Sf(x_i) - S\sigma(x_i) \text{ (apply smoothing operator } S) \\ V_p(x_i) &= Sf(x_i) - S(Sf(x_i)) \\ V_p(x_i) &= Sf(x_i) - S^2f(x_i) \\ V_p(x_i) &\approx 0, \text{ since } S^2 = S \end{aligned} \quad (4.6)$$

The set of equations 4.6 can be explained as follows: Lemma 2 claims that the smoothing spline $S_p(\bullet)$ allows us to present the results of measurements with two terms: the first term $\sigma_p(x_i)$, $i=1, \dots, n$, is the “smooth” term estimating the dependence of the signal of interest on time, and the second $\mu_p(x_i) = y_i - \sigma_p(x_i)$, $i=1, \dots, n$, is the differences representing the noise dependence on time.

If the factor p is selected correctly, then the smooth term should not contain “visible”

traces of noise, and the difference should not have "regular" components from the signal, in essence splitting the signal into a term containing only our detected particle and a term containing only the noise (see the example in Figure B.1).

If we now re-apply the smoothing spline σ_p with the correct smoothing factor to the difference $\mu_p(x_i)$, we get the spline $v_p(x)$, which is equal to zero. If however the smoothing spline "smooths" too much or too little (by having the incorrect smoothing factor p) $v_p(x)$ will not be equal to zero.

So in order to find the most optimal value of p we calculate the spline $v_p(x)$ and its norm $\|v_p(x)\|^2$ for each value of the smoothing factor p $[p_1, \dots, p_n]$. The best value for p is then the one where $\|v_p(x)\|^2$ is minimal. Hence we have now found the optimal smoothing spline from which we can calculate the parameters for the parabola and the binding point x_p of the parabola. Finally the vertex of this parabola gives us the estimate for the time-pick-off.

4.3.3 Paraspline testing methods

This program was developed and now needed testing and characterising. This is to be one of the core focuses of this study. Establishing some sort of baseline to test this, estimating the accuracy of the Paraspline method and finding the limits of the capabilities of this new algorithm.

Two different methods of noise testing were performed. The first of these was a simple noise-to-signal test. This was to be done by adding random noise of differing amplitudes to a "clean" signal. This "clean" signal was created using a smoothing method (moving average) on a normal signal to remove the noise it had. The sample size for this moving average varied depending on the signal amplitude and was chosen separately for each constructed Clean signal, to ensure that the shape of the Clean signal matched the original signals basic form as closely as possible. This clean signals start-time can easily be determined, by simply searching for the first data point that is non-zero. After this smoothing was done the signal was then considered a clean signal containing only the pulse height of the detected particle.

The second test was to first consist of gathering samples of noise. These noise samples were cut from the section of a signal before the leading edge. A graph showing this region is shown in figure 4.5. This region is signal-free, and therefore only contains noise. This noise can then be used to add noise back onto a clean signal, allowing us to compare the results from the program to the clean start-time.

Steps were followed to insure that the average of the noise was zero so as to not add any net amplitude. By fitting a line of best fit to this noise sample, the slope of this line of best fit will then be calculated, and if it was non-zero this sample of noise would also be discarded. This would be done to ensure that no net amplitude would be added to the clean signal.

A library would be created containing different clean signals as well as libraries containing various different noise segments. Doing this allows testing the algorithm with signals of different amplitudes and shapes, as well as different noise samples.

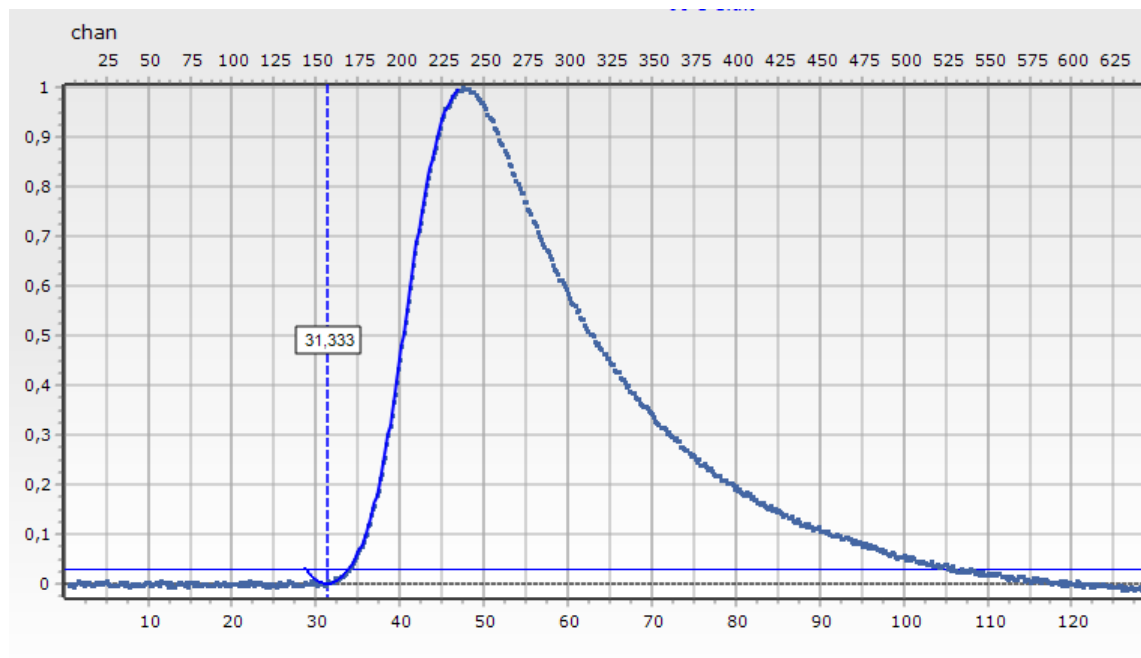


Figure 4.5: Example of a signal where the section of the signal between 0 ns and 30 ns could be seen as a noise-only region

Finally testing would be done with real data:

The LIS spectrometer (figure 3.15) with a ^{252}Cf source would be used, two MCP based timing detectors (St1 and St2), and a PIN diode that served for both energy and time registration. The data acquisition system consisted of the fast digitizer DT5742 and a desktop computer. MCP detectors do not suffer from PD, and so the start of the pulse can be extrapolated by fitting a line to the rising edge of the pulse. This line is then extended to where it intersects the average average noise amplitude. These two accurate times (T1 and T2) along with the distance between them can then be used to calculate the velocity $V1$ of the ion, and is considered to be the true velocity. After passing detector St2, the ion hits the PIN diode, recording the energy of the ion and together with the Paraspline algorithm a time T3. T2 and T3 would then be used in a similar way to calculate velocity $V2$. The fragment velocity were measured using St2 detector and the PIN diode. Comparing $V1$ and $V2$ event by event could then be done.

A second test would be conducted as well. This spectrometer also consisted of two MCP time detectors (St1 and St2), and a PIN diode used for time and energy registration. As in the LIS spectrometer experiment, T1 and T2 would be calculated using signals measured by St1 and St2. T3 would again be calculated via the Paraspline method using data recorded by the PIN diode.

Before St1 a degrader foil was installed. The ^{132}Xe beam with energy approximately 160 MeV provided by IC-100 accelerator At JINR would then be used to bombard this a target. Ions knocked out from the target at a 30° angle to the beam would then pass through the degrader and into the spectrometer.

Targets of Al (5 μm thick), Ti (2 μm), Cu (3.6 μm), Ag (0.1 μm), Au (0.1 μm), Zr (2 μm) and Ni (1 μm) would be used, allowing us to test the Paraspline algorithm across a wide range of ion masses. Ensuring a wide range of energies from knocked out ions reach the spectrometer the degrader would be varied as well:

1. No degrader
2. 4 μm thick Ti foil.

3. 5 μm thick Ti foil.
4. 6 μm thick Ti foil.
5. 4 μm thick Ti foil + 10 μm thick Al foil.

This setup can be seen in figure 4.7.

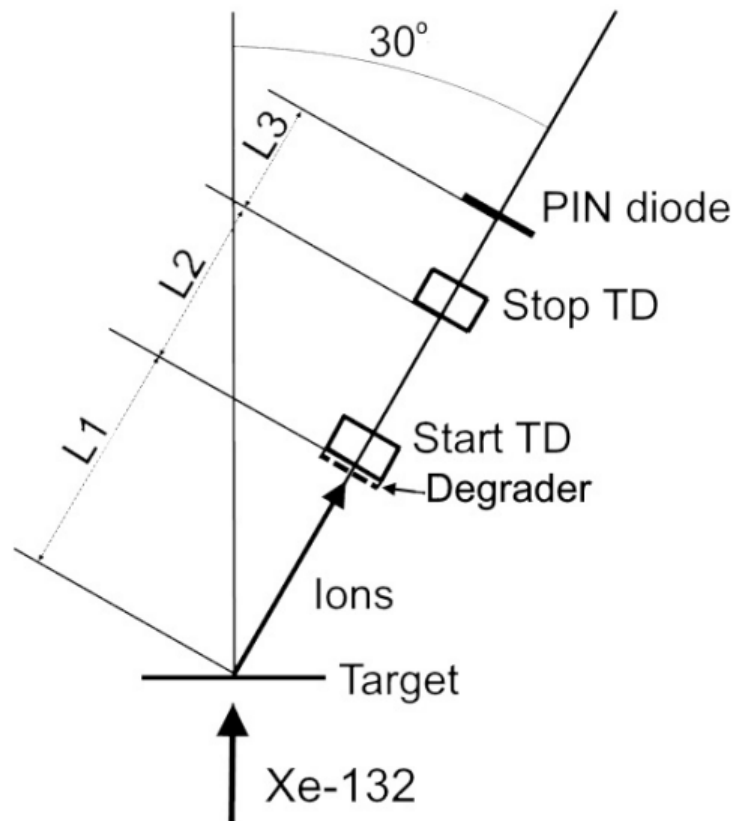


Figure 4.6: Experimental setup of the experiment at IC-100 accelerator. Target - Al, Ti, Cu, Ag, Au, Zr or Ni foil; Start TD, Stop TD - MCP time detectors; Degradator - Ti and Al foil of different thickness. $L1 = 500$ mm, $L2 = 142$ mm, $L3 = 141$ mm

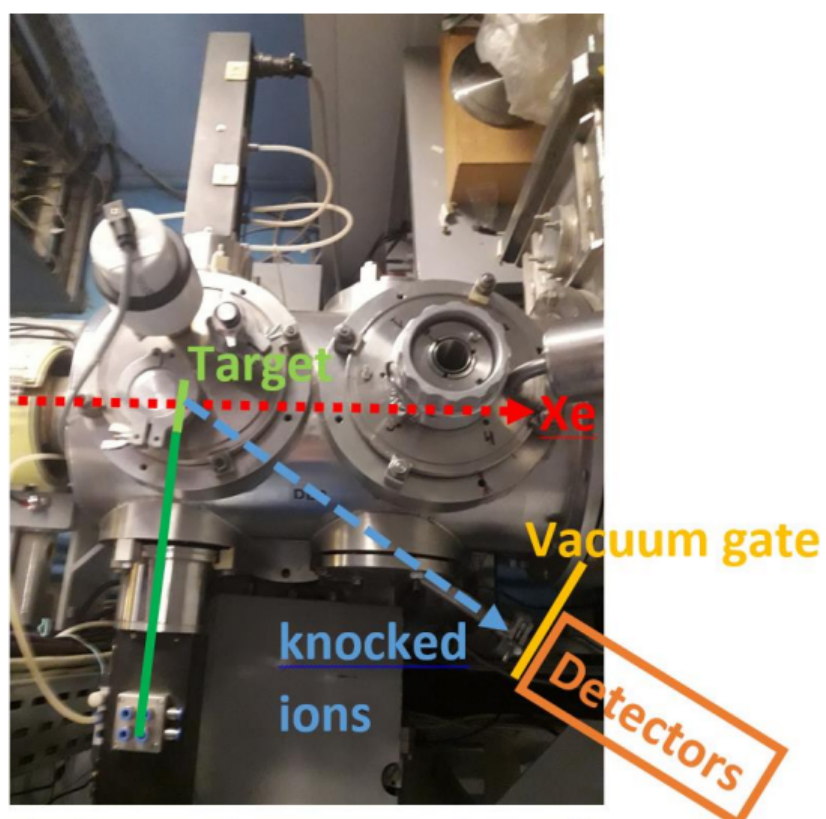


Figure 4.7: Photo of the target knot of the experimental setup at IC-100 accelerator.

CHAPTER 5

RESULTS

5.1 PROBABILITY ESTIMATION OF DETECTING CCT EVENTS

This simulation was done for a ^{252}Cf source with a radius of 5mm (green disc on figure 4.1). Further investigations were also done on larger angles and different sized Cf sources to see how that would affect the probability, (note that these results don't have any particular relevance to our setup, as the angles relevant to CCT are usually below 1 degree and our Cf source is fixed at a radius of 5mm) these results are graphed in figure 5.1.

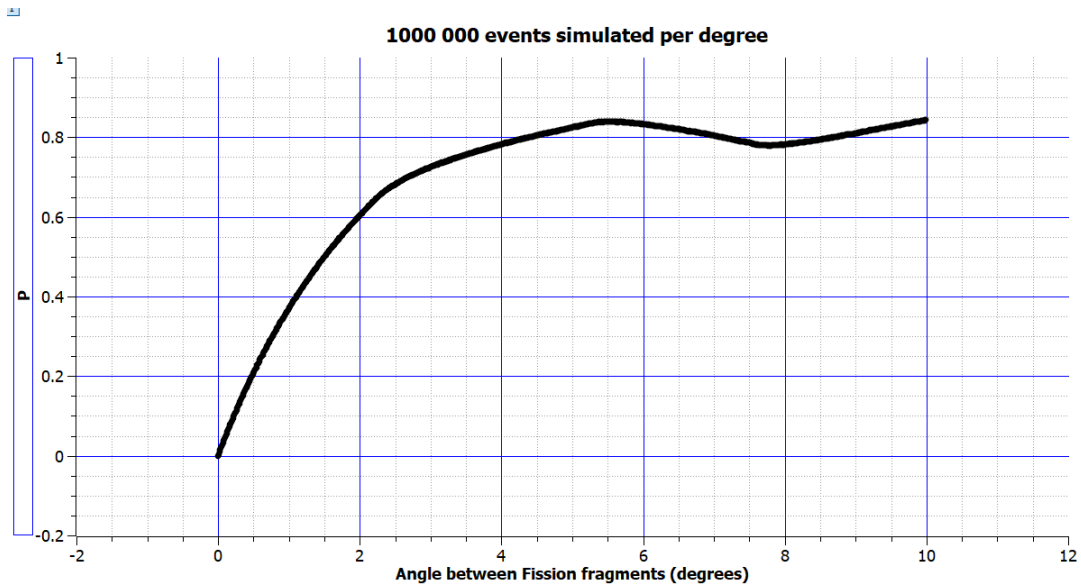


Figure 5.1: This graph simulates 1000 000 events per angle, in angular increments of 0.01 degrees.

A series of simulations was done in order to see what effect different target sizes would have on the final probability calculated. The results of these simulations are shown in figure 5.2 and figure 5.3.

As can be seen from figure 5.2 the effect on the probability is very minimal considering the difference in target radius ranges from 0mm up to 150mm (this is the same as the distance from the target to the array) Figure 5.3 is the same graph as

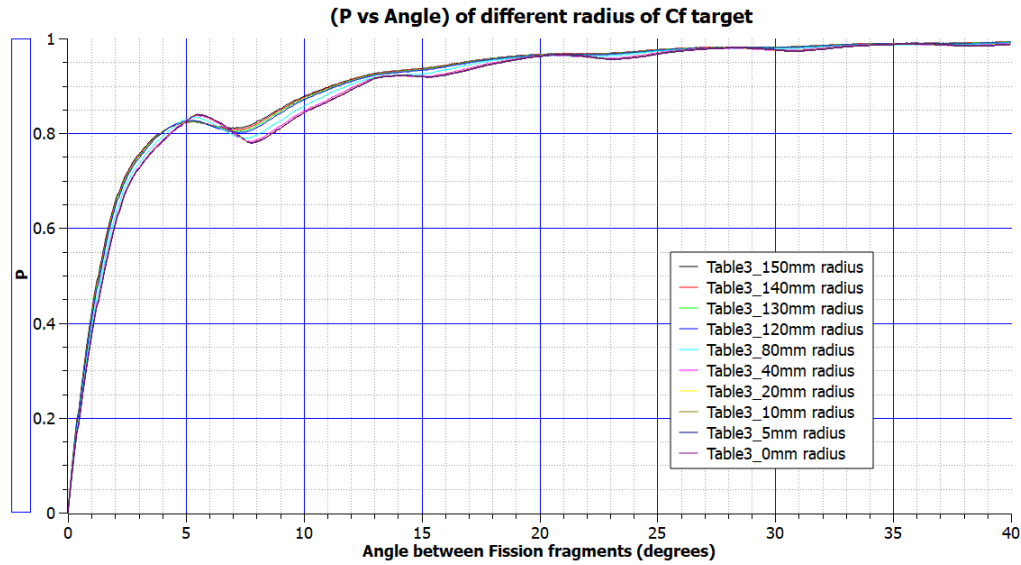


Figure 5.2: This graph simulates 1000 000 events per angle, with 1000 different angles between 0-10 degrees. This is done for each of the 10 different target sizes.

figure 5.2 but zoomed in on the region of [5;11] degrees. As can be seen from this graph there is practically no difference between the results of 0mm, 5mm, 10mm and 20mm radius of the Cf target. The target radius only really start to affect the results when it is larger than 20mm.

From figure 5.3 (same graph as figure 5.2 only zoomed) it appears that an increased target size (looking at 140mm and 150mm for exaggeration of this effect) affects the calculation in the following way:

- It seems that compared to the 0mm target radius the larger target radius results are squeezed in the x axis. As if the angle between the two particles are artificially increased.
- It also appears as if it “smooths” the graph. The turning points at around 5-6 and 7-8 degrees have a larger max and min value for smaller target sizes that that of the larger target sizes, i.e. it smooths the curve.

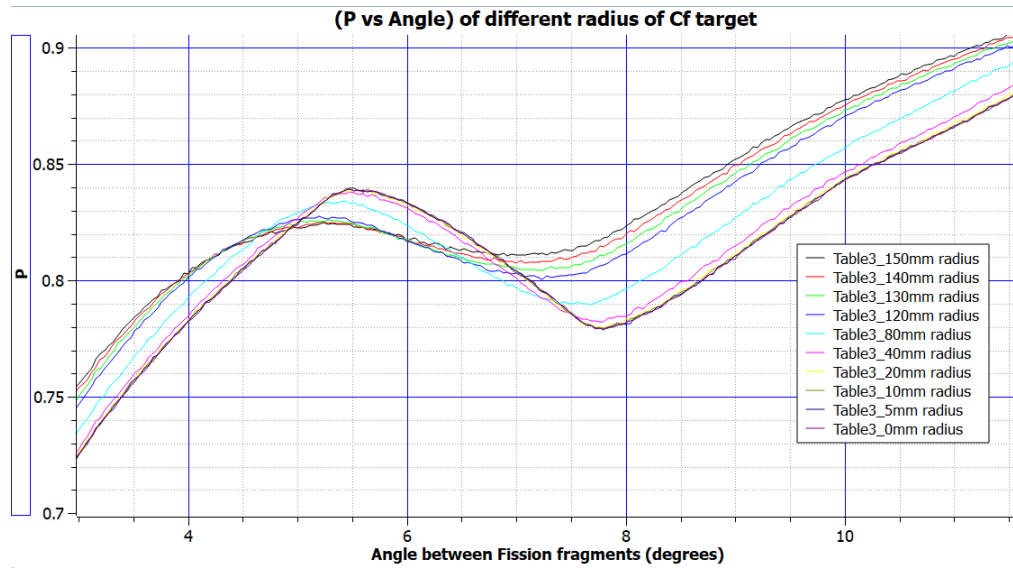


Figure 5.3: This graph simulates 1000 000 events per angle, with 1000 different angles between 0-10 degrees. This is done for each of the 10 different target sizes. Zoomed in on the significant part of the smaller angles.

5.2 DISTANCE DISTRIBUTIONS OF DETECTED PARTICLES

The results obtained from the distance distribution simulation can be seen in figures 5.4, 5.5, 5.6 and 5.7. Each of these has a fixed source diameter d , while varying the angle θ .

Seeing as how our ^{252}Cf source has a diameter of 5mm and that the PINs usually don't exceed 5° from perpendicular to the direction of the ions flight, it can be seen that the range of distances from the source to the PINs is (146.4, 153.9) [mm]. At this short distance it would have a maximum of $\pm 2.60\%$ effect on the distance, and therefore on the calculated velocity. Velocity has a squared effect on the calculated mass (M), leaving us with a maximum of $\pm 5.41\%$ inaccuracy in the calculated mass. The vast majority of the particle trajectories do however lie a lot closer to 150 mm, but this showcases how much of an effect the distance distribution has on results. Note also that this distance distribution affects is worse for heavier particles, further muddying the water when trying to detect heavy ions.

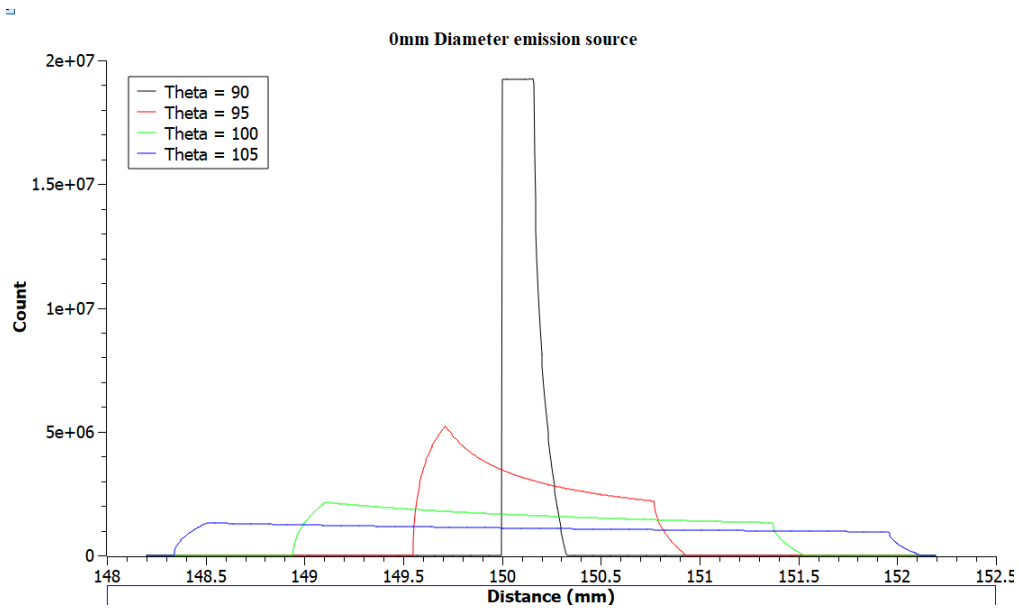


Figure 5.4: Histogram of the amount of different distances calculated for the configuration ($d = 0$ mm).

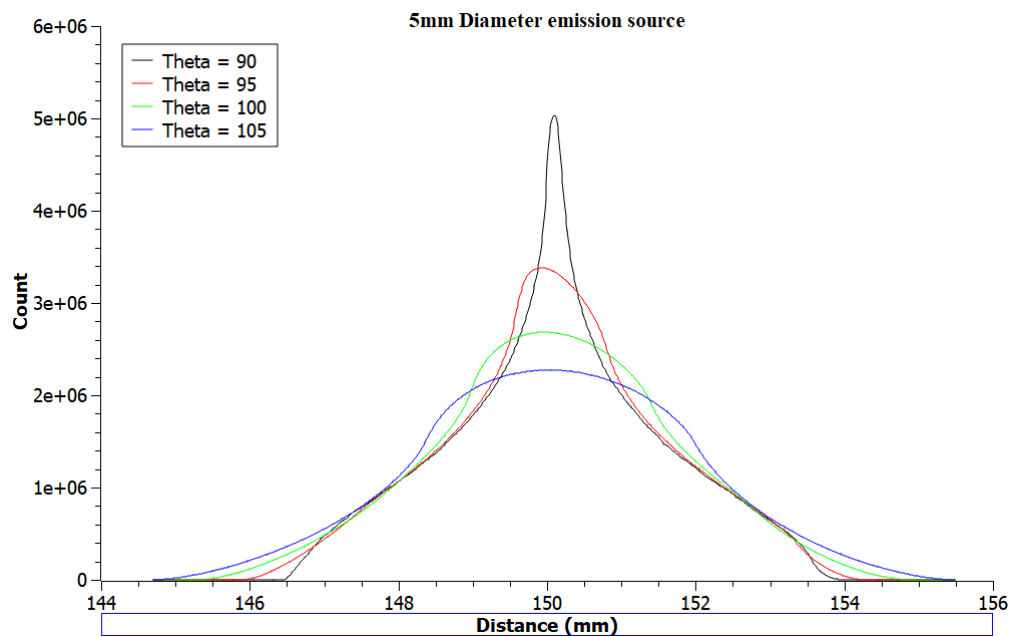


Figure 5.5: Histogram of the amount of different distances calculated for the configuration ($d = 5$ mm).

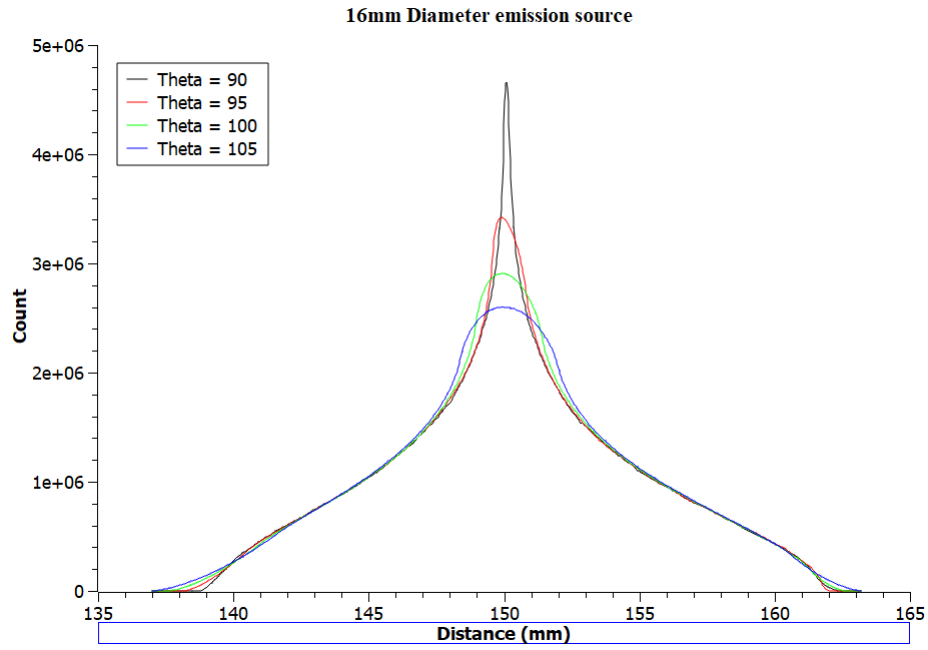


Figure 5.6: Histogram of the amount of different distances calculated for the configuration ($d = 16$ mm).

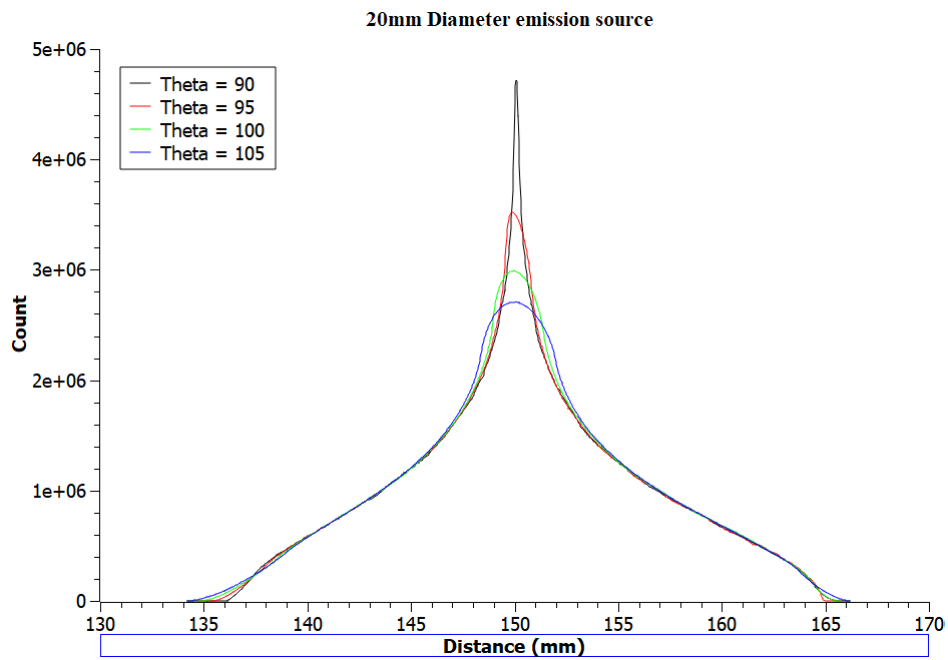


Figure 5.7: Histogram of the amount of different distances calculated for the configuration ($d = 20$ mm).

5.3 NEW TIME-PICK-OFF “PARASPLINE” ALGORITHM

5.3.1 Noise to signal ratio test results

The Figures 5.8, 5.9 and 5.10 are some of the results obtained while testing the programmes ability to find a signal pulse and determine that pulse’ start-time.

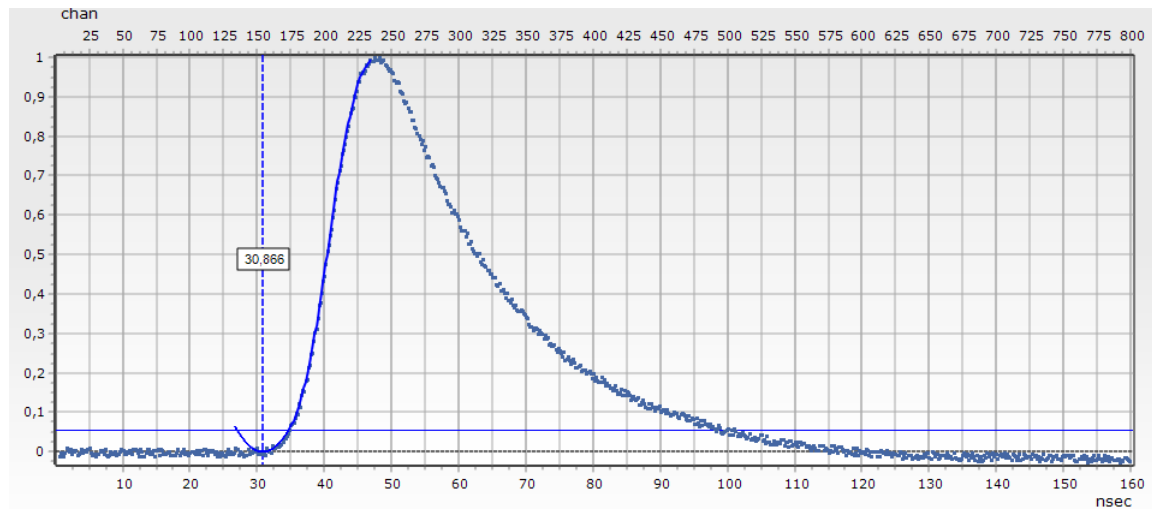


Figure 5.8: Clean signal with $\pm 2\%$ of the signals maximum amplitude added.

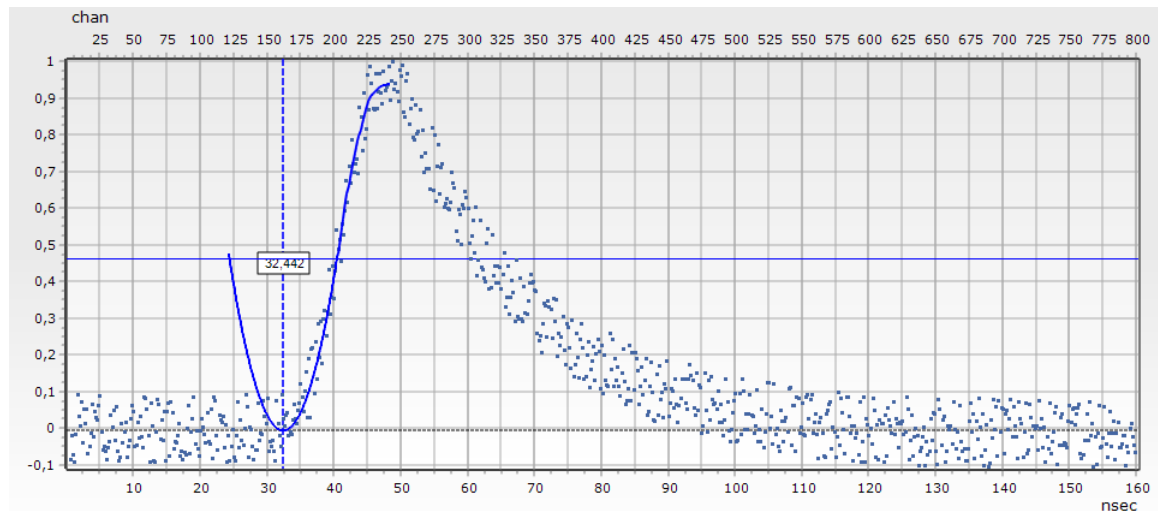


Figure 5.9: Clean signal with $\pm 20\%$ of the signals maximum amplitude added.

The program fails to calculate any sort of start-point when the noise to signal ratio reaches $\pm(30-35)\%$ and higher. The goal of this test was mainly to test the robustness

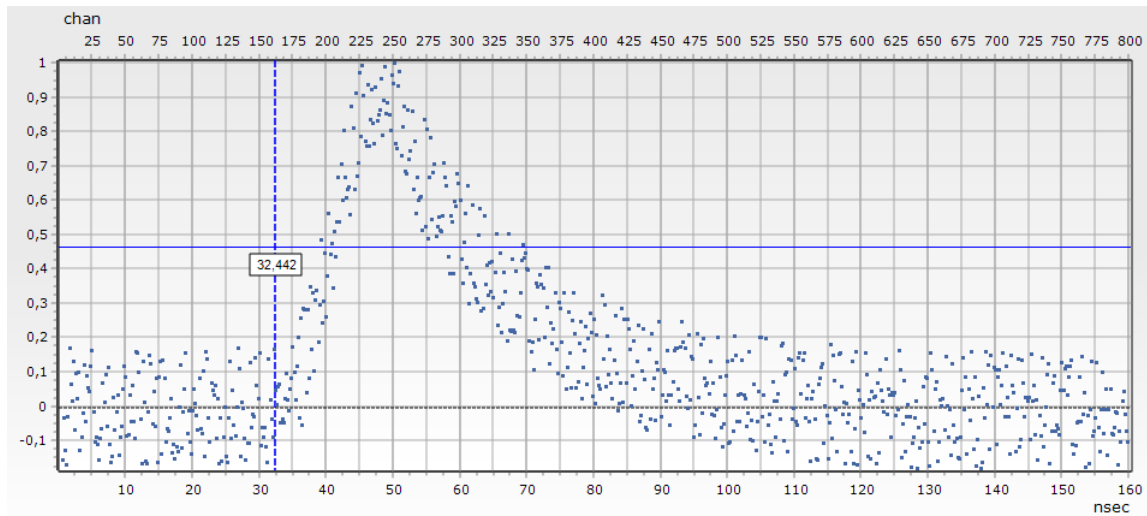


Figure 5.10: Clean signal with $\pm 40\%$ of the signals maximum amplitude added.

of the program, testing it to where it fails to perform its function.

5.3.2 Clean signal + real noise test results

Amplitude	Clean	Clean Paraspline	Mean	Average deviation	Standard Deviation	Error
30	48.4000	48.9182	46.1709	-2.2291	28.8927	± 10.9256
277	50.4000	51.8115	53.5141	3.1141	0.5484	± 1.2696
717	35.4000	36.0282	37.0979	1.6979	0.4431	± 0.8496
988	53.0000	54.1688	54.7255	1.7255	0.3134	± 0.5839
1452	29.4000	30.1805	31.7950	2.395	0.2809	± 0.5953
1777	25.2000	25.9317	26.9174	1.7174	0.2836	± 0.6205
1843	46.4000	46.8789	48.1857	1.7857	0.3329	± 0.68295

Table 5.1: Table containing some of the results from the second test on the Paraspline method.

- **Amplitude:** The amplitude of the clean signal.
- **Clean:** The start of the clean signal, determined by derivatives.
- **Mean:** The average start time of all the noisy signals determined by the Paraspline program.
- **Deviation:** The difference between the **Clean** start time and the **Mean**

- **Standard Deviation:** Standard deviation of the 37 start times determined by the Paraspline program.
- **Error:** This is the error* of each of the measurements.

**This error was obtained by taking the difference between the maximum and minimum determined start times and dividing by two.*

5.3.3 Results of the experiment at IC-100 reactor

In the calibration experiment at LIS spectrometer, Paraspline algorithm was first validated by comparing the experimental positions of the light and heavy peaks in ff mass and velocity distributions with the ones from the literature. The application of the algorithm let us calculate the velocities and masses of the ffs. These were then compared to values from literature [65]. The mass spectrum figure 5.11 shows a 0.9 a.m.u and 0.7 a.m.u difference for the lighter and heavier ffs respectively. This is less than 1% deviation for both.

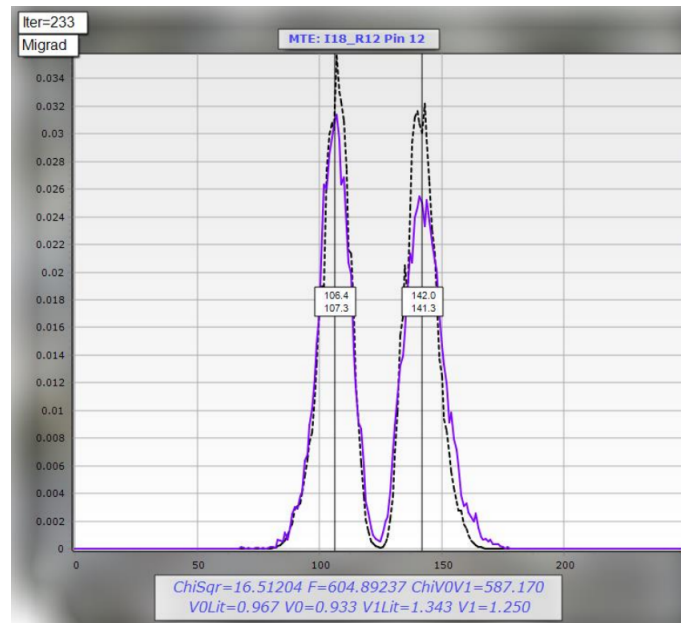


Figure 5.11: Experimental mass [a.m.u] spectrum from the ^{252}Cf source in LIS setup (blue line – experimental data, dotted line – literature data). (y-axis in arb. units)

Figure 5.12 is a velocity spectrum, showing a deviation of 0.034cm/ns for the slower

ff and 0.093 cm/ns for the faster ff and is a 3.5% and 6.9% deviation respectively. This shows that the Paraspline estimates the events start-time as a little bit later than the true value.

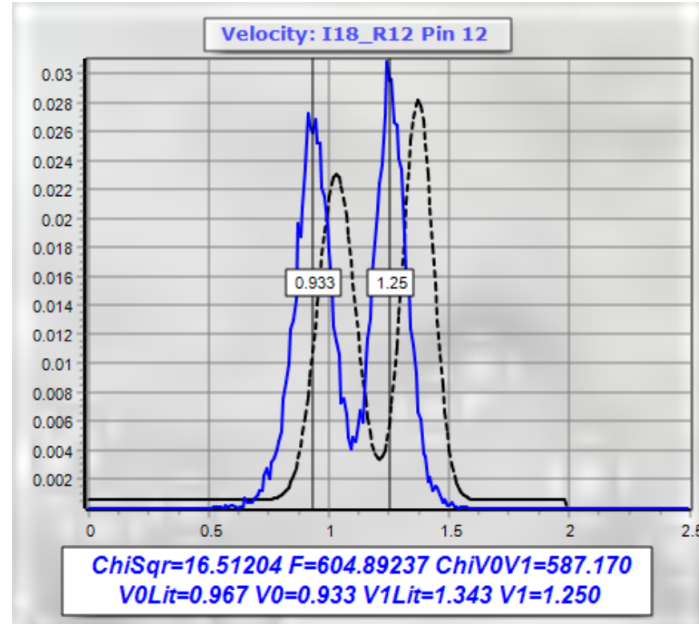


Figure 5.12: Experimental velocity [cm/ns] spectrum from the ^{252}Cf source in LIS spectrometer experiment (blue line – experimental data, dotted line – literature data) (y-axis in arb. units).

Next the Paraspline algorithm was further checked with an event by event comparison of “true” velocity $V1$ and $V2$. To do this, two-dimensional discretization was performed on the $V1/(V2 - V1)$ variables set. The arithmetic mean $\langle V2 - V1 \rangle$ was calculated for every $V1$ class, figure 5.13 is a graph of $\langle V2 - V1 \rangle$ versus $V1$. The result demonstrates that in the statistically reliable region, the mean difference $\langle V2 - V1 \rangle$ does not exceed 0.5% of the ions velocity.

The regions at the low and high end of the x-axis have very large uncertainties, this was due to the relatively low amount of data in these regions. and explains the high deviation in figure 5.12.

In the experiment at IC-100 accelerator, the Paraspline algorithm was further verified by reconstructing ion’s masses using velocity calculated from data collected by a PIN-diode. The correctness of the algorithm was checked from M/E distribution. Event

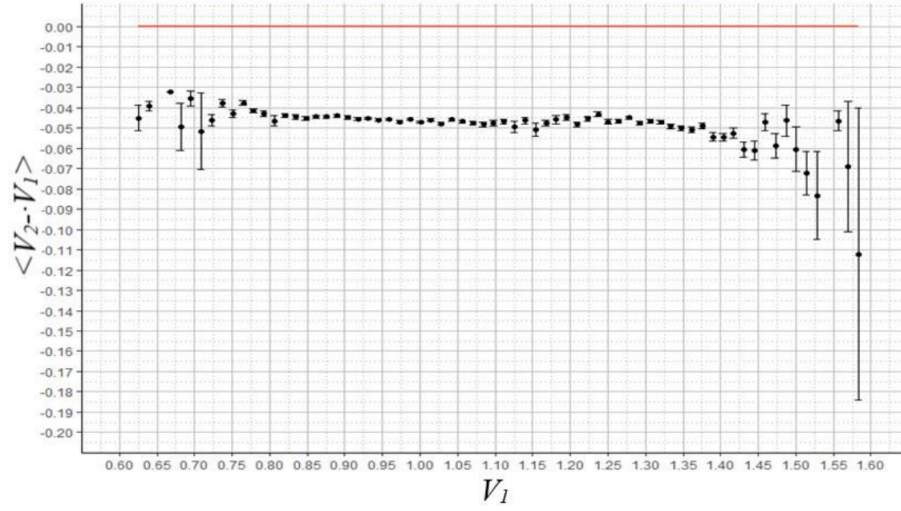


Figure 5.13: Mean difference $\langle V_2 - V_1 \rangle$ as a function of V_1 for the fragments from the ^{252}Cf source in LIS spectrometer experiment.

by event distribution (figures 5.14, 5.16, 5.18) was converted into a $\langle M \rangle/E$ after two-dimensional discretization (figures 5.15, 5.17, 5.19).

The result of the mass reconstruction for all emitters and degrader combinations in the experiment at the IC-100 accelerator is shown in figure 5.20. It demonstrates that the proposed Paraspline algorithm functions as intended and accurately enough corrects for the PD effect.

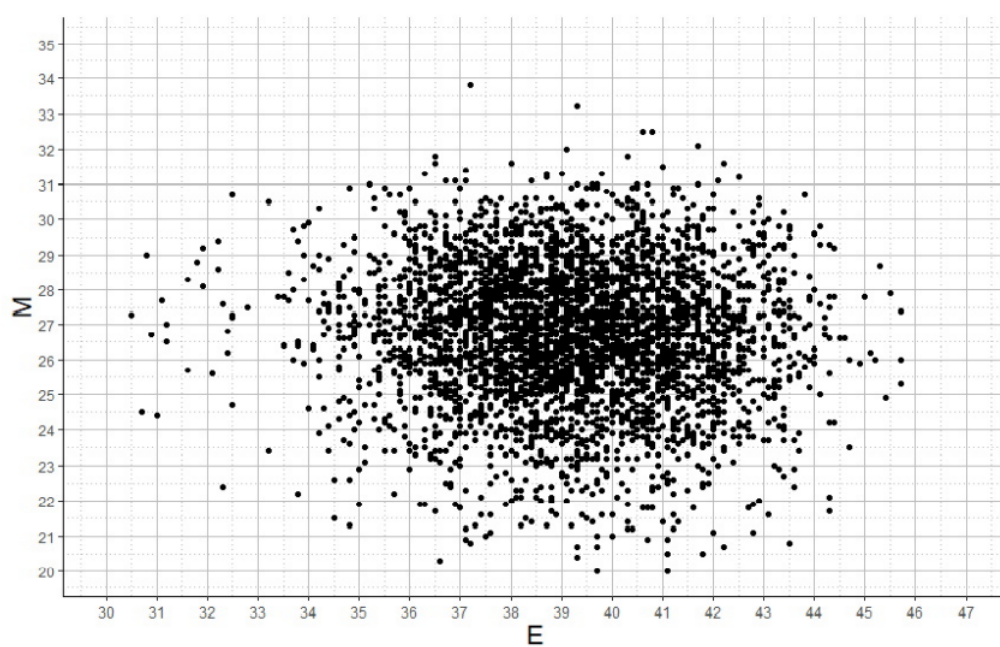


Figure 5.14: $M(\text{a.m.u})$ as a function of Energy (MeV) in experiment with Al emitter and 5 μm thick Ti foil degrader at IC-100 accelerator.

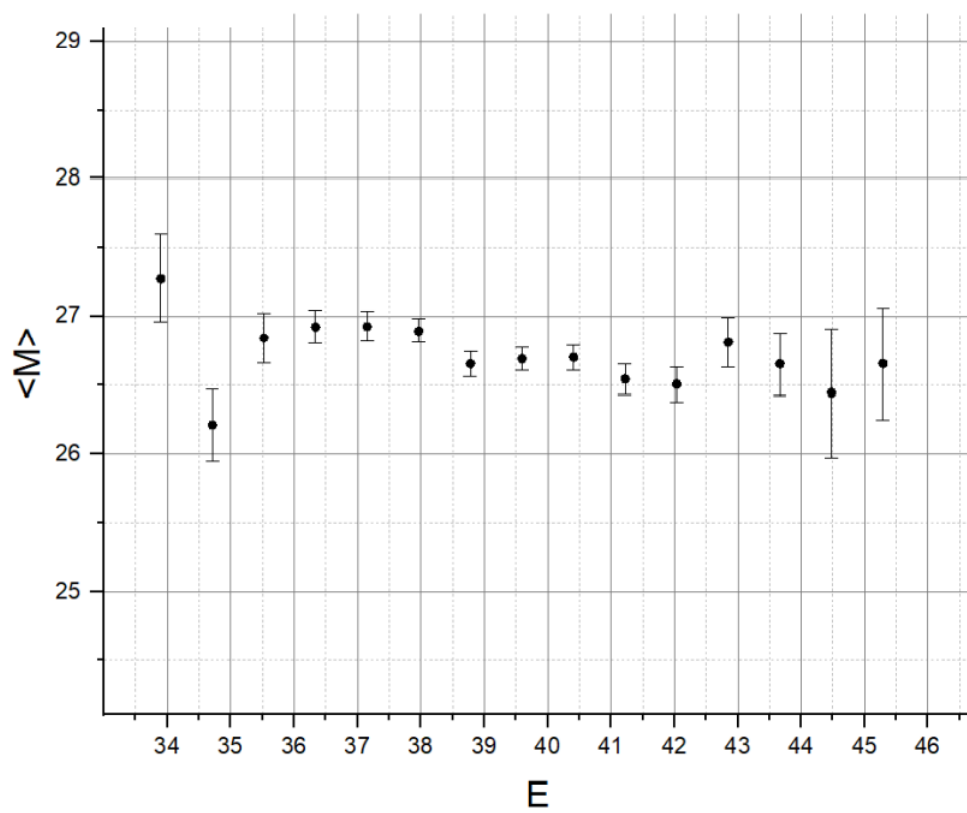


Figure 5.15: $\langle M \rangle$ (a.m.u) as a function of Energy (MeV) in experiment with Al emitter and 5 μm thick Ti foil degrader at IC-100 accelerator.

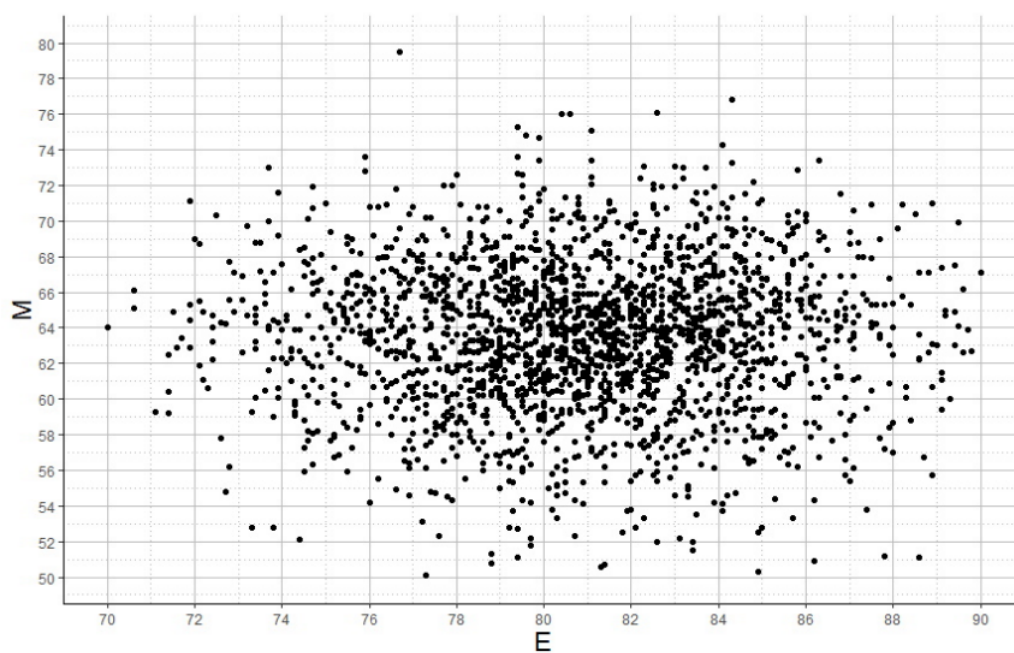


Figure 5.16: M (a.m.u) as a function of Energy (MeV) in experiment with Cu emitter and 5 μm thick Ti foil degrader at IC-100 accelerator.

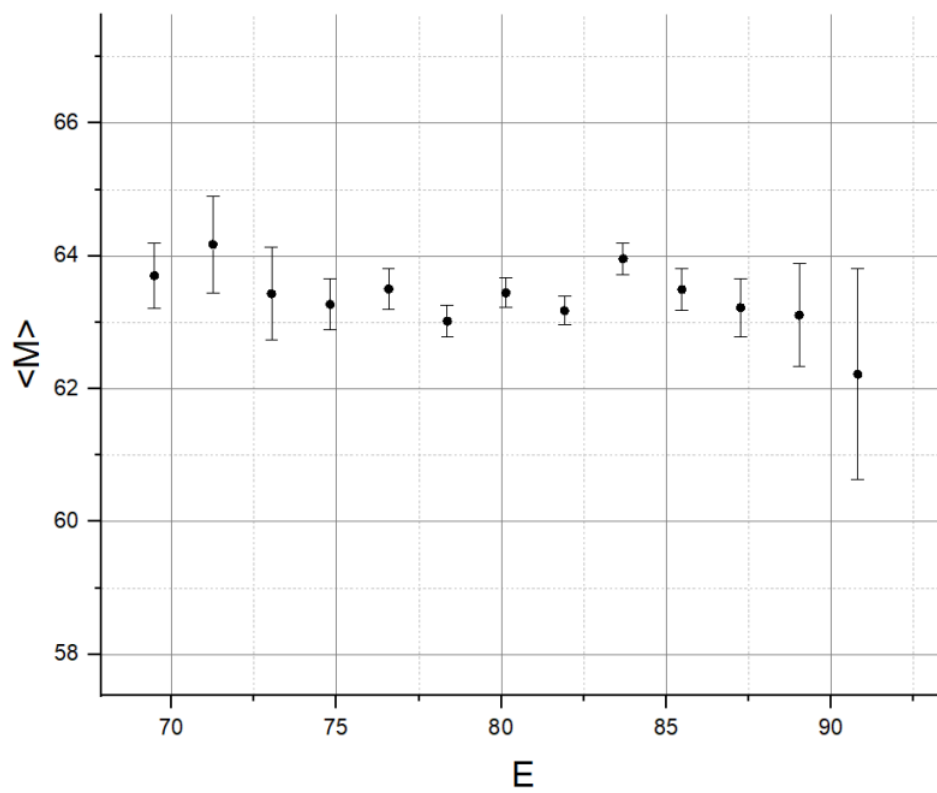


Figure 5.17: $\langle M \rangle$ (a.m.u) as a function of Energy (MeV) in experiment with Cu emitter and 5 μm thick Ti foil degrader at IC-100 accelerator.

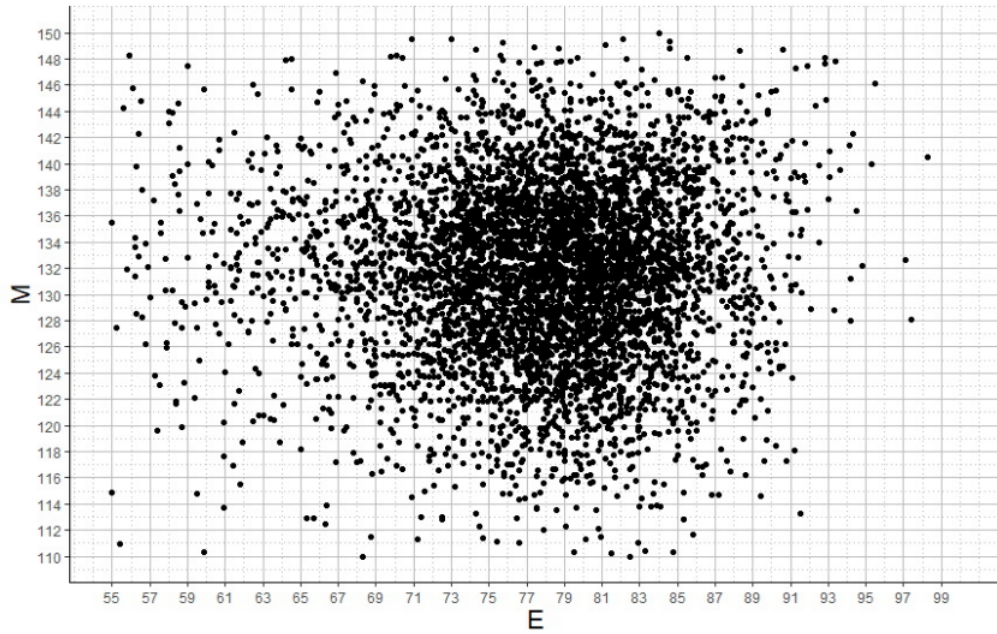


Figure 5.18: M (a.m.u) as a function of Energy (MeV) in experiment with Xe emitter and no degrader at IC-100 accelerator.

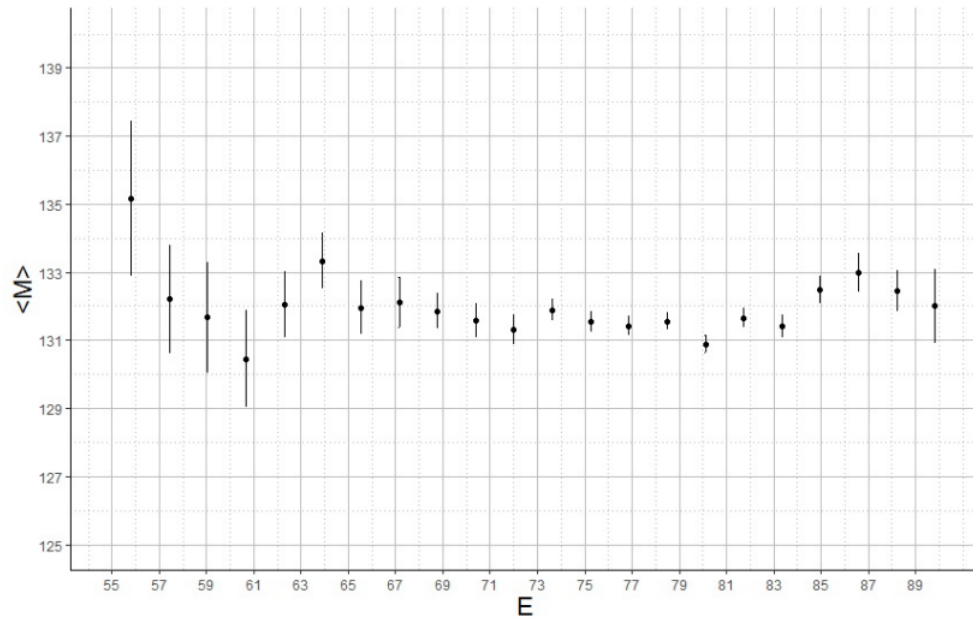


Figure 5.19: $\langle M \rangle$ (a.m.u) as a function of Energy (MeV) in experiment with Xe emitter and no degrader at IC-100 accelerator.

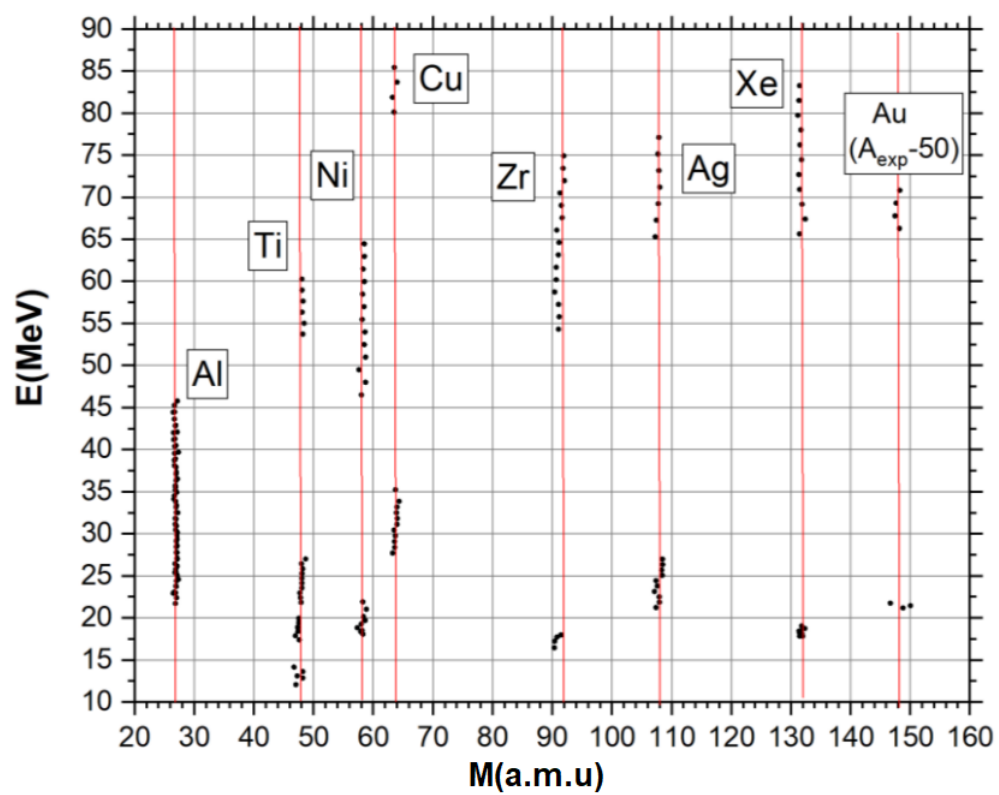


Figure 5.20: Energy/Mass distribution for all ions and all combination of degraders in the experiment at IC-100 accelerator (Standard Error of Mean is so small that error bars are omitted in the plot).

CHAPTER 6

CONCLUSION AND FURTHER OUTLOOK

6.1 CONCLUSIONS

From figure 5.1 it can very clearly be seen that our detection efficiency of these CCT events is quite low and points us to a possible avenue of increasing the amount of data that can be collected. However simply moving the PIN diodes closer to one another is easier said than done because of the attached electrical components such as signal amplifiers. Simply decreasing this distance also increases the distribution of distances that would be seen. From Chapter 5.2 we know how much this distance can influence the final mass calculation.

Increasing the distance between the two detectors when calculating TOF with a PIN diode and an MCP detector would provide more reliable mass reconstruction result. There is, therefore, a balance to be struck between the data collection rate and data accuracy.

Correctness of Paraspline pick-off algorithm was tested in two time-of-flight experiments as well as some signal/noise ratio tests. The results from the testing are very promising, good agreement between the experimental velocities and the respective values from the literature, as well as unbiased mass reconstructed in a wide range of particle energies. The test results demonstrate that the developed algorithm provides a reliable and robust “true” pick-off time for PIN diodes when used as timing detectors.

6.2 IMPROVEMENTS AND SHORTCOMINGS

The results/constraints from the probability estimation of detecting CCT events can be incorporated with the distance distribution simulation, disallowing the innermost region of the PIN as a viable detection surface. This is because of the fact that the two particles are moving very close to one another and as such could only really be detected separately if one of the particles hit the PIN on its edge, as hitting the PIN

in the center would result in the second particle hitting that same detector. This would also affect the distance distribution simulation results as less events would have a distance in close to or at 150mm. This would result in a higher count rate for distances far from 150mm and therefore result in more inaccuracy when calculating the mass of the particle.

Although there is no reason to doubt the accuracy of the results obtained from the two developed Monte-Carlo simulations (sections 5.1 and 5.2). Testing and confirming these results by performing these same simulations with known software such as GEANT4 developed at CERN would be a good confirmation (or possibly contradiction). Furthermore performing the distance simulation for the source at various angles (In this study only the outermost PIN diode in a PIN diode array such as in figure 4.1 was considered), errors can be calculated for each of the PINs in such an array, and used to sort events into "reliability categories" based on the PIN diode it was detected in.

As for the Paraspline algorithm, comparing the test results from the (Clean signal + Noise) with the results from the testing conducted with real data there is some discrepancy. It seems to perform much better with real data, suggesting that there could be a flaw in the method used in the (Clean signal + Noise) test. Although not confirmed it is theorised this flaw could have come from the smoothing process used to create the "Clean signal", altering the general shape of the signal, which then in turn caused the Paraspline algorithm to perform worse. Further testing of the Paraspline algorithm could also have been done, by comparing it to the older Parablin method. Due to time constraints this was not done. It is also important to note that the testing and developing of this algorithm is an ongoing endeavour (at the time of writing this).

REFERENCES

- [1] D. Kamanin and Y. Pyatkov, “Clusterization in ternary fission,” *Clusters in Nuclei*, vol. 3, pp. 2–69, 2014.
- [2] B. R. Martin, *Nuclear and Particle Physics*. John Wiley and Sons, 2006.
- [3] “NobelPrizes”, “All nobel prizes in physics,” 2021. <https://www.nobelprize.org/prizes/lists/all-nobel-prizes-in-physics/>.
- [4] E. Rutherford, “Uranium radiation and the electrical conduction produced by it,” *Found in Philosophical Magazine*, vol. 47, no. 284, p. 109–163, 1899.
- [5] P. Ehrenfest, “Ersetzung der hypothese vom unmechanischen zwang durch eine forderung bezüglich des inneren verhaltens jedes einzelnen elektrons,” *Die Naturwissenschaften*, vol. 13, no. 47, p. 953–954, 1925.
- [6] J. Chadwick, “The existence of a neutron,” *Proceedings of the Royal Society A*, vol. 136, no. 830, p. 692–708, 1932.
- [7] D. D. Iwanenko, “The neutron hypothesis,” *Nature*, vol. 129, no. 830, p. 798, 1932.
- [8] A. Caesar, “Atom diagram,” 2018. https://commons.wikimedia.org/wiki/File:Atom_Diagram.svg.
- [9] G. Elert, “Binding energy,” 2021. <https://physics.info/binding/>.
- [10] A. S. Eddington, “The internal constitution of the stars,” *The Scientific MonthlyPattern*, vol. 11, no. 4, p. 297–303, 1920.
- [11] “Nuclear”, “Nuclear binding energy,” 2021. https://en.wikipedia.org/wiki/Nuclear_binding_energy.
- [12] Yukawa and Hideki, “On the interaction of elementary particles,” *Proceedings of the Physico-Mathematical Society of Japan*, vol. 3, no. 17, p. 48–57, 1935.
- [13] “TheFourFourses”, “The four forces,” 1995. <http://webhome.phy.duke.edu/~kolena/modern/forces.html#005>.

- [14] E. Tretkoff, “December 1938: Discovery of nuclear fission,” 2021. <https://www.aps.org/publications/apsnews/200712/physicshistory.cfm>.
- [15] P. Regan, “Basic physics of nuclear reactors,” 2015. <https://slideplayer.com/slide/4881701/>.
- [16] K. Takada, “Nuclear liquid drop model,” 2006. http://ne.phys.kyushu-u.ac.jp/seminar/MicroWorld3_E/3Part3_E/3P33_E/nuclear_fission_E.htm.
- [17] N. T. Redd, “What is fission?,” 2013. <https://www.livescience.com/23326-fission.html>.
- [18] “Fission”, “Fission,” 2021. <http://oregonstate.edu/instruct/ch374/ch418518/Chapter\%2011\%20Fission.pdf>.
- [19] J. O. Rasmussen, “Radioactivity,” 2021. <https://www.britannica.com/science/radioactivity/Gamma-decay>.
- [20] L. Green and D. Livesey, “Ternary fission,” *Nature*, vol. 195, p. 332, 1947.
- [21] “GammaRadiation”, “Gamma radiation,” 2021. <https://www.arpansa.gov.au/understanding-radiation/what-is-radiation/ionising-radiation/gamma-radiation>.
- [22] J. Konya and N. Nagy, “Nuclear and radio-chemistry,” *Elsevier*, p. 74–75, 2012.
- [23] D. Schardt, R. Kirchner, O. Klepper, W. Reisdorf, E. Roeckl, P. Tidemand-Petersson, G. Ewan, E. Hagberg, B. Jonson, S. Mattsson, and G. Nyman, “Alpha decay studies of tellurium, iodine, xenon and cesium isotopes,” *Nuclear Physics A*, vol. 326, no. 1, pp. 65–82, 1979.
- [24] P. Möller, “The limits of the nuclear chart set by fission and alpha decay,” *EPJ Web of Conferences*, vol. 131, 01 2016.
- [25] B. R. Martin and G. Shaw, *Nuclear and particle physics: an introduction*. John Wiley & Sons, 2019.

- [26] D. Poenaru, “Spontaneous emission of heavy clusters,” *Journal of Physics G: Nuclear Physics.*, vol. 10, no. 8, p. 183–189, 1984.
- [27] Y. Ronen, “The relation between ternary fission and cluster decay,” *Annals of Nuclear Energy*, vol. 29, no. 8, pp. 1013–1018, 2002.
- [28] H. Rose and G. Jones, “A new kind of natural radioactivity,” *Nature*, vol. 307, p. 245, 1984.
- [29] F. Gönnerwein, “Ternary and quaternary fission,” *Nucl. Phys.*, vol. A734, pp. 213–216, 2004.
- [30] C. Beck, *Clusters in Nuclei*. Springer, 2012.
- [31] U. Brosa, S. Grossmann, and A. Müller, “Nuclear scission,” *Physics Reports*, vol. 197, no. 4, pp. 167–262, 1990.
- [32] R. Canavan and M. Freer, “Demonstration of the universality of molecular structures in prolate deformed nuclei,” 2020. https://www.researchgate.net/publication/346701747_Demonstration_of_the_Universality_of_Molecular_Structures_in_Prolate_Deformed_Nuclei.
- [33] S. Pieper, C. Steven, and R. Wiringa, “Quantum monte carlo calculations of light nuclei,” *Annual Review of Nuclear and Particle Science*, vol. 51, no. 1, pp. 53–90, 2001.
- [34] W. von Oertzen, M. Freer, and Y. Kanada-En’yo, “Nuclear clusters and nuclear molecules,” *Physics Reports*, vol. 432, no. 2, pp. 43–113, 2006.
- [35] J. Maruhn and Z. Greiner, W., “The asymmetric two center shell model,” *Physik*, vol. 251, no. 431, 1972.
- [36] B. Buck, C. Dover, and J. Vary, “Simple potential model for cluster states in light nuclei,” *Phys. Rev. C*, vol. 11, p. 1803, 1974.

- [37] E. J. du Toit, S. M. Wyngaardt, and S. M. Perez, “Cluster decay of ^{234}u and ^{232}th by the emission of neon isotopes,” *Journal of Physics G: Nuclear and Particle Physics*, vol. 42, no. 1, p. 015103, 2014.
- [38] F. Gonnenein, M. Wostheinrich, M. Hesse, H. Faust, F. H., and S. Oberstedt, ““seminar on fission”, belgium,” 2000. <https://slideplayer.com/slide/4881701/>.
- [39] E. Piasecki, M. Dakowski, T. Krogulski, J. Tys, and J. Chwaszczewska, ““evidence of the polar emission of alpha particles in the thermal neutron fission of ^{235}u ”,” *Physics Letters B*, vol. 33B, no. 8, pp. 568–570, 1970.
- [40] P. M. Walker and G. D. Dracoulis, “Atlas of nuclear isomers and their systematics,” *Nature*, vol. 399, no. 35, pp. 103–107, 1999.
- [41] K. Vijayaraghavan, W. von Oertzen, and M. Balasubramaniam, “Kinetic energies of cluster fragments in ternary fission of cf-252 ,” *European Physics Journal*, vol. 48, p. 27, 2012.
- [42] H. Diehl and W. Greiner, “Theory of ternary fission in the liquid drop model,” *Nuclear Physics A*, vol. 229, pp. 29–46, 1974.
- [43] Y. Pyatkov, V. Pashkevich, Y. Penionzhkevich, V. Tishchenko, and C. Herbach, “Collinear tripartition of ^{248}cm and ^{252}cf nuclei as a probe of clustering,” 2000. International Conference of Nuclear Physics ”Nuclear Shells – 50 Years, Dubna.
- [44] Y. Pyatkov, D. Kamanin, E. Sokol, A. Alexandrov, I. Alexandrova, S. Khlebnikov, S. Motrofanov, Y. Penionchkevich, Y. Ryabov, T. V.G., and S. Yamaletdinov, “Search for collinear tripartition of the cf-252 nucleus at the modified-fobos spectrometer,” *World Scientific*, pp. 181–185, 2002.
- [45] D. Kamanin, “Summary of experimental results on ccollinear cluster tripartition studies,” 2012. <https://slideplayer.com/slide/8489965/>.
- [46] S. Yamaletdinov, *Studies of Exotic Decay Modes in Fission of Heavy Elements*. PhD thesis, University of Jyväskylä, 2007.

- [47] H. Ortlepp, W. Wagner, C. Herbach, A. Aleksandrov, I. Aleksandrova, M. Andrassy, A. Budzanowski, B. Czech, M. Danziger, L. Dietterle, V. Doronin, A. Dshemuchadse, S. and Fomichev, M. Fromm, W.D. and Gebhardt, P. Gippner, K. Heidel, S. Heinitz, H. Homeyer, S. Ivanovsky, D. Kamanin, I. Kolesov, A. Matthies, D. May, S. Merzlyakov, W. von Oertzen, Y. Oganessian, G. Pausch, Y. Penionzhkevich, Y. Pyatkov, S. Radnev, G. Renz, L. Rubinskaya, I. Sandrev, K. Schilling, W. Seidel, D. Shishikin, A. Sirotin, H. Sodan, O. Strekalovsky, V. Tishchenko, V. Trofimov, I. Tsurin, C. Umlauf, D. Vakarov, V. Vasko, V. Vitenko, E. Will, M. Wilpert, R. Yanez, V. Zhuchko, P. Ziem, and L. Zrodowski, “The 4pi-fragment spectrometer fobos,” *Nuclear Instruments and Methods in Physics Research A*, vol. 403, pp. 46–97, 1997.
- [48] D. Kamanin and Y. Pyatkov, *Clusterization in ternary fission*, vol. 3. B. Christian, Ed., Springer, 2014.
- [49] D. Kamanin, Y. Pyatkov, W. von Oertzen, A. Aleksandrov, I. Aleksandrova, O. Falomkina, N. Kondratjev, Y. Kopatch, E. Kuznetsova, Y. Lavrova, A. Tyukavkin, W. Trzaska, and V. Zhuchko, “Collinear cluster tri-partition of cf-252 and in the u-235(n_{th} , f) reaction,” *European Physics Journal*, vol. 45, pp. 29–37, 2010.
- [50] V. Malaza, “Multi-detector registration system for the study of multi-body decay of heavy body nuclei,” Master’s thesis, Stellenbosch University, 2012.
- [51] V. Malaza, *Experimental study of cluster effects in binary and ternary decays of low excited actinides*. PhD thesis, Stellenbosch University, 2018.
- [52] Y. Pyatkov, D. Kamanin, A. Alexandrov, I. Alexandrova, N. Kondratyev, E. Kuznetsova, A. Strekalovsky, O. Strekalovsky, V. Zhuchko, N. Mkaza, and V. Malaza, “Observation of light shape isomers in the multi-body decay of cf-252,” 10 2015.
- [53] Y. Pyatkov, D. Kamanin, A. Alexandrov, I. Alexandrova, Z. Goryainova, V. Malaza, G. Mishinsky, E. Kuznetsova, A. Solodov, A. Strekalovsky,

- O. Strekalovsky, and V. Zhuchko, “New side of the collinear cluster tri-partition scenario,” *Proceedings of the 27th International Seminar on Interaction of Neutrons with Nuclei, Dubna, Russia,*, pp. 249–252, 2020.
- [54] Y. Pyatkov *et al.*, “Manifestation of pear-shaped clusters in collinear cluster tri-partition cct,” *Phys. Rev. C*, vol. 96, no. 6, p. 064606, 2017.
- [55] Y. V. Pyatkov, D. Kamanin, W. von Oertzen, A. Alexandrov, I. Alexandrova, O. Falomkina, N. Kondratjev, Y. N. Kopatch, E. Kuznetsova, Y. E. Lavrova, *et al.*, “Collinear cluster tri-partition of 252 cf (sf) and in the 235 u (n th, f) reaction,” *The European Physical Journal A*, vol. 45, no. 1, pp. 29–37, 2010.
- [56] “PINdiode”, “Pin diode,” 2021. https://en.wikipedia.org/wiki/PIN_diode.
- [57] W. Starzecki, A. Stefanini, S. Lunardi, and C. Signorini, “A compact time-zero detector for mass identification of heavy ions,” *Nuclear Instruments and Methods*, vol. 193, pp. 499–505, 1982.
- [58] J. Wiza, “Microchannel plate detectors,” *Nuclear Instruments and Methods*, vol. 162, pp. 587–601, 1979.
- [59] “Azhuk”, “What you may not know about californium-252,” 2020. <https://www.frontier-cf252.com/blog/what-you-may-not-know-about-californium-252/>.
- [60] “Californium-252(Cf-252)Production”, “Californium-252 (cf-252) production,” 2020. <https://www.frontier-cf252.com/californium-information/production/>.
- [61] V. Spiegel, “The effective half-life of californium-252,” *Nuclear Science and Engineering*, vol. 53, no. 3, pp. 326–327, 1974.
- [62] W. Bohne, W. Galster, K. Grabisch, and H. Morgenstern, “The influence of plasma effects on the timing properties of surface-barrier detectors for heavy

- ions,” *Nuclear Instruments and Methods in Physics Research Section A: Accelerators, Spectrometers, Detectors and Associated Equipment*, vol. 240, no. 1, pp. 145–151, 1985.
- [63] D. Kamanin, A. Strekalovsky, and V. Zhuchko, “New approaches to determination of the heavy ion’s mass in measurements with pin diodes,” *Kazakhstan: RGP IYaF*, 2017.
- [64] Y. Pyt’ev, O. Falomkina, and S. Shishkin, “Subjective restoration of mathematical models for a research object, its measurements, and measurement-data interpretation,” *Pattern Recognition and Image Analysis: Advances in Mathematical Theory and Applications*, vol. 29, no. 4, p. 577–591, 2019.
- [65] C. Wahl, “Atomic data and nuclear data tables,” vol. 39, 1988.

APPENDIX A

MASS RECONSTRUCTION PROCEDURE

Mass reconstruction procedure developed to compensate for PHD in semiconductor detectors, full description in [51].

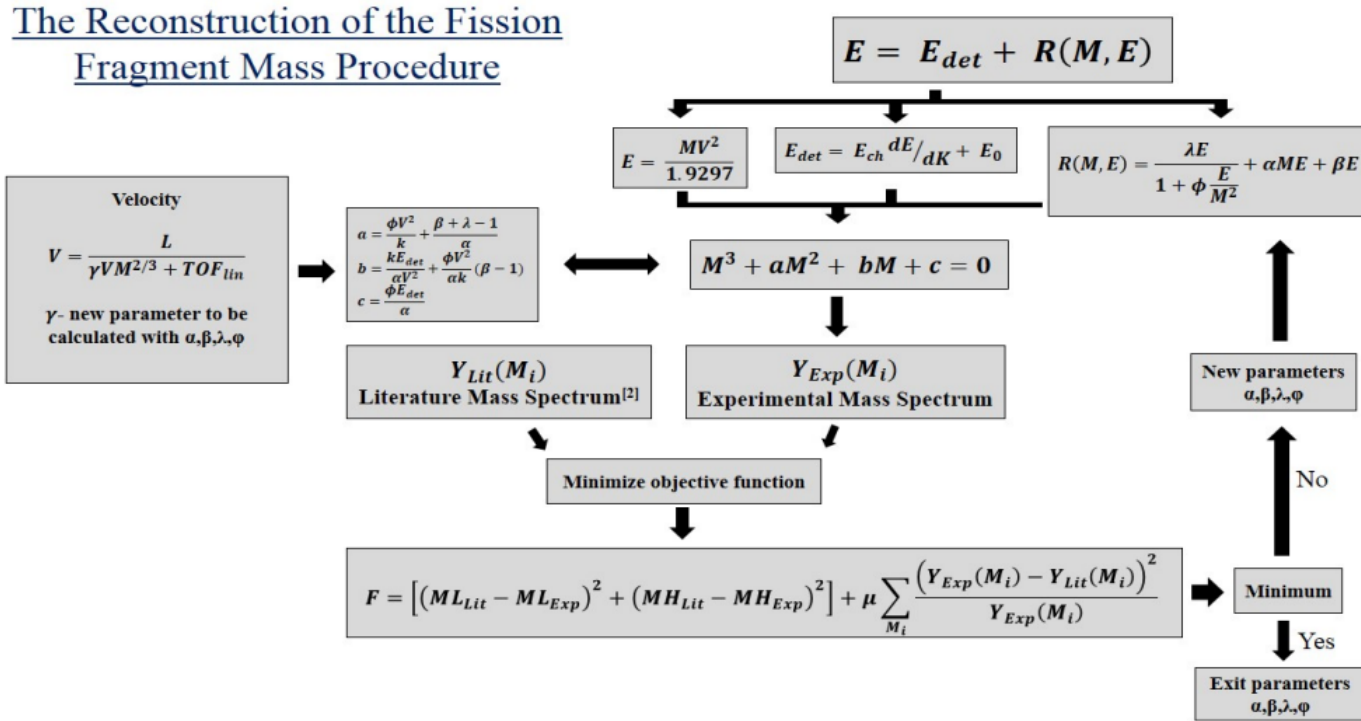


Figure A.1: Flow diagram of the mass reconstruction procedure used to compensate for the pulse height defect[51].

APPENDIX B

SPLINES

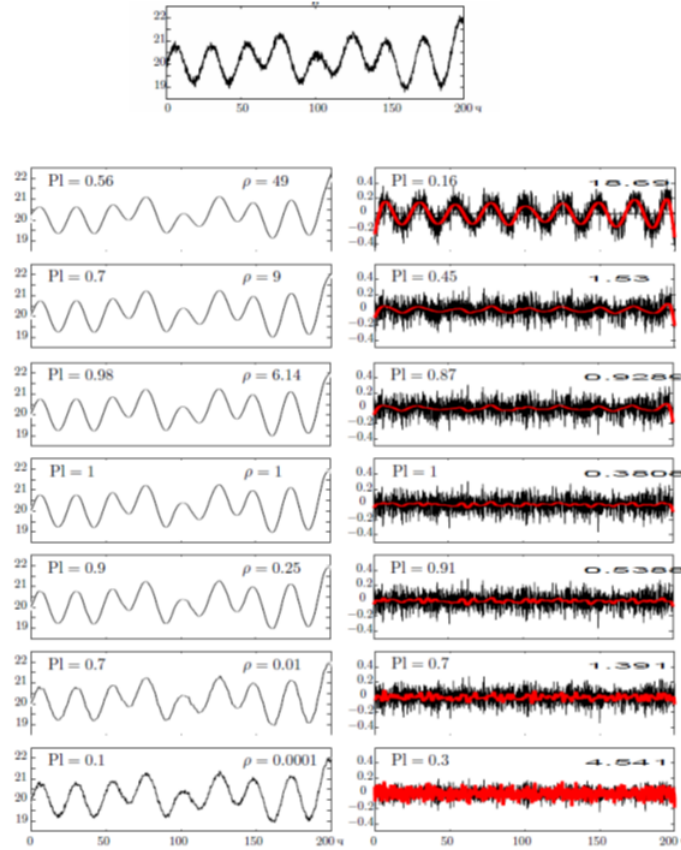


Figure B.1: Example from article [64], applying this criteria. The upper figure shows the dependence $f(x_i)=y_i$, $i=1, \dots, N$, of temperature from time in a certain water reservoir. The left column shows smoothing splines $\sigma_p(x_i)$, $i=1, \dots, n$, of order $q=2$, calculated for different values of the smoothing factor ($p=49, 9, 6.14, 1, 0.25, 0.01, 0.0001$, values of p indicated in the upper right corner of each chart in the left column). The right column shows graphs of the corresponding differences $\mu_p(x_i)=y_i-\sigma_p(x_i)$, $i=1, \dots, n$, and the red line on each chart in the right column shows smoothing splines σ'_p , calculated on the basis of differences $\mu_p(x_i)=y_i-\sigma_p(x_i)$, $i=1, \dots, n$. In the upper right corner of each chart the norm value is shown in the right column $\|v_p(x)\|^2$, $p=49, 9, 6.14, 1, 0.25, 0.01, 0.0001$. It can be seen that the value $\|v_p(x)\|^2$ is minimal for $p_{opt}=1$, which determines the optimal smoothing spline σ_{opt} .

APPENDIX C

CODE

C.0.1 Probability Estimation

```

1      #include <stdlib.h>
2      #include <stdio.h>
3      #include <math.h>
4      #include <time.h>
5
6      // Global Variables //
7      double RandomNum();
8      double Crosspoint(double *Vecto);
9      double SphereConvert(double *Vecto);
10     double PositionCheck(double *Vecto);
11
12     double radi,test,difper,diferp,maxdeg,f1x, f2x, f1y, f2y,
13     ↪   thetadeg,theta, arclength,
14     ↪   rando,pi,direction,pers,surfaceratio;
15
16     int
17     ↪   check,theyaredif,p22,p1,p2,events,numofdeg,xx1,xx2,yy1,yy2,different,dif,cumdif
18
19     ↪   //////////////////////////////////////
20     /*
21     ↪
22     ↪           START OF MAIN
23     ↪   */
24
25     ↪   //////////////////////////////////////
26
27     int main()
28     {
29         srand ( time(NULL) ); //seed random number
30         rando = RandomNum(); //initialize seed
31         /*
32         printf("Number of Events... ");
33         scanf("%d",&events);

```

```

25     printf("number of angles tested between 0 and Maximum angle...
↪     ");
26     scanf("%d",&numofdeg);
27     printf("Maximum Angle tested...  ");
28     scanf("%f",&maxdeg);
29     */
30     // initial conditions
31     // these first three are varied to change results
32     events = 1000000;
33     numofdeg = 1000;
34     maxdeg = 40;
35
36     pi = 3.141592654;
37     thetadeg = 10;
38     arclength = 2*pi*1*thetadeg/360;
39     xx1 = 0;
40     xx2 = 0;
41     yy1 = 0;
42     yy2 = 0;
43     different = 0;
44     cumdif = 0;
45     areacount = 0;
46     surfaceratio = 0.;
47     difper = 0.;
48     radi = 0;
49
50     //Define Arrays
51     double *Probabilities = (double *) malloc((((long)
↪     (numofdeg))*sizeof(double));
52     if(Probabilities == NULL) // error statement if the array could
↪     not be given the required amount of memory
53     {
54         printf("ERROR: requested size of arrayUniform is too large");
55         exit(1);
56     }
57     double *Degrees = (double *) malloc((((long)
↪     (numofdeg))*sizeof(double));
58     if(Degrees == NULL)

```



```

59     {
60         printf("ERROR: requested size of arrMag is too large");
61         exit(1);
62     }
63     double *Vector = (double *) malloc((((long)
64     ↪ (9)))*sizeof(double));
65     if(Vector == NULL)
66     {
67         printf("ERROR: requested size of arrMag is too large");
68         exit(1);
69     }
70     for (int i = 0; i < 9; ++i)
71     {
72         Vector[i] = 0;
73     }
74     for (int i = 0; i < numofdeg; ++i) //Uses the event function to
75     ↪ calculate
76     {
77         thetadeg = (double)i/(double)numofdeg*maxdeg;
78         Degrees[i] = thetadeg;
79         cumdif = 0;
80         for (int j = 0; j < events; ++j)
81         {
82             reset:
83             radi = RandomNum()*130;
84             direction = RandomNum()*360;
85             theta = direction*pi/180;
86             Vector[0] = radi*cos(theta);
87             Vector[1] = radi*sin(theta);
88             Vector[6] = (RandomNum()*140) + 20;
89             Vector[7] = (RandomNum()*100)-50;
90             Vector[8] = RandomNum()*360;
91             Crosspoint(Vector);
92             SphereConvert(Vector);
93             different = PositionCheck(Vector);
94             if (different == 3)
95             {

```

```

95         goto reset;
96     }
97     cumdif = cumdif + different;
98 }
99 pers = cumdif/(double)events;
100 Probabilities[i] = pers;
101 printf("%.2f\r Percentage Complete: ",
    ↪ ((double)i/(double)numofdeg*100));
102 }
103
104 // Output to file
105 FILE *fptr;
106 fptr = fopen("Algo3ResultsA.txt","w");
107 fprintf(fptr,"Theta");
108 fprintf(fptr," Probability\n");
109 for (int i = 0; i < numofdeg; ++i)
110 {
111     fprintf(fptr,"%f",Degrees[i]);
112     fprintf(fptr," %f\n", Probabilities[i]);
113 }
114 fclose(fptr);
115 printf("\n Done");
116
117 // Free all the memory //
118 free(Probabilities);
119 free(Degrees);
120 free(Vector);
121 }
122
123 ↪ //////////////////////////////////////
124
125 ↪ /*
126 ↪ END OF MAIN                                */
127
128 ↪ //////////////////////////////////////
129
130 // Functions
131 double RandomNum()

```

```

128 {
129     return (double)rand() / (double)RAND_MAX;
130 }
131 double Crosspoint(double *Vecto)
132 {
133     double t = 0;
134     double a = 0;
135     double b = 0;
136     double c = 0;
137     double A = 0;
138     double B = 0;
139     double C = 0;
140     double a1 = 0;
141     double b1 = 0;
142     double x1 = 0;
143     double y1 = 0;
144     double z1 = 0;
145     double x,y,z;
146     double radius = 1;
147     double tempx;
148     double tempy;
149     double arclength = tan(pi*thetadeg/180); // this should replace
        ↪ radius
150     a1 = Vecto[6]*pi/180;
151     b1 = Vecto[7]*pi/180;
152     a = cos(a1)*cos(b1);
153     b = sin(b1);
154     c = sin(a1)*cos(b1);
155
156     A = ((a*a)+(b*b)+(c*c));
157     B = 2*(Vecto[0]*a) + 2*(Vecto[1]*b);
158     C = ((Vecto[0]*Vecto[0])+(Vecto[1]*Vecto[1])-(150*150));
159
160     t = (-B + sqrt((B*B)-(4*A*C)))/(2*A);
161     x1 = Vecto[0];
162     y1 = Vecto[1];
163     z1 = 0;
164     Vecto[0] = Vecto[0] + t*a;

```

```

165     Vecto[1] = Vecto[1] + t*b;
166     Vecto[2] = t*c;
167
168     Vecto[3] = arclength*cos(Vecto[8]*pi/180);
169     Vecto[4] = arclength*sin(Vecto[8]*pi/180);
170     Vecto[5] = 1;
171     a1 = (-Vecto[6] + 90)*pi/180;
172     b1 = (-Vecto[7] )*pi/180;
173     x = Vecto[3];
174     y = Vecto[4];
175     z = Vecto[5];
176     Vecto[3] = x*cos(a1) + y*sin(a1)*sin(b1) + z*cos(b1)*sin(a1);
177     Vecto[4] = y*cos(b1) - z*sin(b1);
178     Vecto[5] = -x*sin(a1) + y*cos(a1)*sin(b1) + z*cos(a1)*cos(b1);
179     Vecto[3] = Vecto[3] + x1;
180     Vecto[4] = Vecto[4] + y1;
181     A =
182         ↪ (x1*x1)+(y1*y1)+(Vecto[5]*Vecto[5])+(Vecto[3]*Vecto[3])+(Vecto[4]*Vecto[4])-(2*
183     B = (2*y1*Vecto[4])+(2*x1*Vecto[3])-(2*y1*y1)-(2*x1*x1);
184     C = ((x1*x1)+(y1*y1)-(150*150));
185
186     t = (-B + sqrt((B*B)-(4*A*C)))/(2*A);
187     Vecto[3] = x1 + t*Vecto[3] - t*x1;
188     Vecto[4] = y1 + t*Vecto[4] - t*y1;
189     Vecto[5] = t*Vecto[5];
190 }
191 double SphereConvert(double *Vecto)
192 {
193     double x1,x2,y1,y2,z1,z2;
194     x1 = Vecto[0];
195     y1 = Vecto[1];
196     z1 = Vecto[2];
197     x2 = Vecto[3];
198     y2 = Vecto[4];
199     z2 = Vecto[5];
200     Vecto[0] = sqrt((x1*x1)+(y1*y1)+(z1*z1));
201     Vecto[3] = sqrt((x2*x2)+(y2*y2)+(z2*z2));
202     Vecto[1] = atan(z1/x1)*180/pi;

```

```

202     if (Vecto[1] < 0)
203     {
204         Vecto[1] = Vecto[1] + 180;
205     }
206     Vecto[4] = atan(z2/x2)*180/pi;
207     if (Vecto[4] < 0)
208     {
209         Vecto[4] = Vecto[4] + 180;
210     }
211     Vecto[2] = acos(y1/Vecto[0])*180/pi;
212     Vecto[5] = acos(y2/Vecto[3])*180/pi;
213 }
214 double PositionCheck(double *Vecto)
215 {
216     double f1y,f2y,f1x,f2x;
217     int theyaredif,p1,p2;
218     f1y = Vecto[2];
219     f1x = Vecto[1];
220     f2y = Vecto[5];
221     f2x = Vecto[4];
222     p1 = 0;
223     p2 = 0;
224     theyaredif = 1;
225
226     if ((f1y < 83.506478)||((f1y >= 88.854084) && (f1y <
    ↪ 91.145916))||((f1y >= 96.493522 ))
227     {
228         p1 = 1;
229         goto skip1;
230     }
231     if ((f1x < 60.588167)||((f1x >= 65.935773) && (f1x <
    ↪ 68.227604))||((f1x >= 73.575210) && (f1x < 75.867041))||((f1x
    ↪ >= 81.214647) && (f1x < 83.506478))||((f1x >= 88.854084) &&
    ↪ (f1x < 91.145916))||((f1x >= 96.493522) && (f1x <
    ↪ 98.785353))||((f1x >= 104.132959) && (f1x <
    ↪ 106.424790))||((f1x >= 111.772396) && (f1x <
    ↪ 114.064227))||((f1x >= 119.411833))
232 {

```

```

233     p1 = 1;
234 }
235 skip1:
236 if ((f2y < 83.506478)||((f2y >= 88.854084) && (f2y <
    ↪ 91.145916))||(f2y >= 96.493522 ))
237 {
238     p2 = 1;
239     goto skip2;
240 }
241 if ((f2x < 60.588167)||((f2x >= 65.935773) && (f2x <
    ↪ 68.227604))||((f2x >= 73.575210) && (f2x < 75.867041))||((f2x
    ↪ >= 81.214647) && (f2x < 83.506478))||((f2x >= 88.854084) &&
    ↪ (f2x < 91.145916))||((f2x >= 96.493522) && (f2x <
    ↪ 98.785353))||((f2x >= 104.132959) && (f2x <
    ↪ 106.424790))||((f2x >= 111.772396) && (f2x <
    ↪ 114.064227))||(f2x >= 119.411833))
242 {
243     p2 = 1;
244 }
245 skip2:
246 if ((p1 == 1) && (p2 == 1))
247 {
248     theyaredif = 3;
249 }
250 if ((p1 == 0) && (p2 == 0))
251 {
252     theyaredif = 0;
253 }
254 return theyaredif;
255 }

```

C.0.2 Distance Distribution

```

1      #include <stdlib.h>
2      #include <stdio.h>
3      #include <math.h>
4      #include <time.h>
5          #include <windows.h>
6
7      // Global Variables //
8      double RandomNum();
9      double Points(double *Vecto,double rad,double rot,double
    ↪ *histval,double *histcount);
10
11
12      double
    ↪ min,pi,rando,x,y,z,xs,ys,zs,xe,ze,radius,radi,direction,theta,R45,R0,R5,R10,R15
13      int events,subEvents,HistAmount;
14
15
16      ↪ //////////////////////////////////////
17      /*
18          ↪ START OF MAIN
19          ↪ */
20
21      ↪ //////////////////////////////////////
22
23      int main()
24      {
25          srand ( time(NULL) ); //seed random number
26          rando = RandomNum(); //initialize seed
27
28          events = 100000000;
29          subEvents = 1;
30          HistAmount = 200;
31          Histbin = 3.79/((double)HistAmount);
32          min = 148.34;
33          radius = 0;
34
35
36
37
38
39
40
41
42
43
44
45
46
47
48
49
50
51
52
53
54
55
56
57
58
59
60
61
62
63
64
65
66
67
68
69
70
71
72
73
74
75
76
77
78
79
80
81
82
83
84
85
86
87
88
89
90
91
92
93
94
95
96
97
98
99
100

```

```

30     pi = 3.141592654;
31     R45 = 45*pi/180;
32     R0 = 0;
33     R5 = 5*pi/180;
34     R10 = 10*pi/180;
35     R15 = 15*pi/180;
36
37     //Define Arrays
38     double *Distances = (double *) malloc(((long)
    ↪ (events*subEvents))*sizeof(double));
39     if(Distances == NULL) // error statement if the array could not
    ↪ be given the required amount of memory
40     {
41         printf("ERROR: requested size of arrayUniform is too large");
42         exit(1);
43     }
44     double *HistoCount0 = (double *) malloc(((long)
    ↪ (HistAmount))*sizeof(double));
45     if(HistoCount0 == NULL) // error statement if the array could not
    ↪ be given the required amount of memory
46     {
47         printf("ERROR: requested size of arrayUniform is too large");
48         exit(1);
49     }
50     double *HistoCount1 = (double *) malloc(((long)
    ↪ (HistAmount))*sizeof(double));
51     if(HistoCount1 == NULL) // error statement if the array could not
    ↪ be given the required amount of memory
52     {
53         printf("ERROR: requested size of arrayUniform is too large");
54         exit(1);
55     }
56     double *HistoCount2 = (double *) malloc(((long)
    ↪ (HistAmount))*sizeof(double));
57     if(HistoCount2 == NULL) // error statement if the array could not
    ↪ be given the required amount of memory
58     {
59         printf("ERROR: requested size of arrayUniform is too large");

```



```

60     exit(1);
61 }
62 double *HistoCount3 = (double *) malloc(((long)
    ↪ (HistAmount))*sizeof(double));
63 if(HistoCount3 == NULL) // error statement if the array could not
    ↪ be given the required amount of memory
64 {
65     printf("ERROR: requested size of arrayUniform is too large");
66     exit(1);
67 }
68 double *HistoVal = (double *) malloc(((long)
    ↪ (HistAmount))*sizeof(double));
69 if(HistoVal == NULL) // error statement if the array could not be
    ↪ given the required amount of memory
70 {
71     printf("ERROR: requested size of arrayUniform is too large");
72     exit(1);
73 }
74
75 Points(Distances, radius, R0, HistoVal, HistoCount0);
76 printf("\n");
77 Points(Distances, radius, R5, HistoVal, HistoCount1);
78 printf("\n");
79 Points(Distances, radius, R10, HistoVal, HistoCount2);
80 printf("\n");
81 Points(Distances, radius, R15, HistoVal, HistoCount3);
82 printf("\n");
83
84
85 // Output to file
86 FILE *fptr;
87 fptr = fopen("ResultsA0.txt", "w");
88 fprintf(fptr, "Bin");
89 fprintf(fptr, " Count0");
90 fprintf(fptr, " Count5");
91 fprintf(fptr, " Count10");
92 fprintf(fptr, " Count15\n");
93 for (int i = 0; i < HistAmount; ++i)

```

```

94     {
95         fprintf(fptr,"%f",HistoVal[i]);
96         fprintf(fptr," %f",HistoCount0[i]);
97         fprintf(fptr," %f",HistoCount1[i]);
98         fprintf(fptr," %f",HistoCount2[i]);
99         fprintf(fptr," %f\n", HistoCount3[i]);
100     }
101     fclose(fptr);
102
103     printf("\n Done");
104     // Free all the memory //
105     free(Distances);
106     free(HistoCount0);
107     free(HistoCount1);
108     free(HistoCount2);
109     free(HistoCount3);
110     free(HistoVal);
111     Sleep(1000);
112 }
113
114 ↪ //////////////////////////////////////
115
116 ↪ /*
117 ↪ END OF MAIN                                */
118
119 ↪ //////////////////////////////////////
120
121 // Functions
122 double RandomNum()
123 {
124     return (double)rand() / (double)RAND_MAX;
125 }
126 double Points(double *Vecto,double rad,double rot,double
    ↪ *histval,double *histcount)
127 {
128     for (int i = 0; i < HistAmount; ++i)
129     {
130         histval[i] = min + (double)i*Histbin;

```

```

127         histcount[i] = 0;
128     }
129     for (int i = 0; i < events; ++i)
130     {
131         ys = 0;
132         radi = RandomNum()*rad;
133         direction = RandomNum()*360;
134         theta = direction*pi/180;
135         xs = radi*cos(theta);
136         zs = radi*sin(theta);
137         //first rotation
138         x = xs;
139         y = ys;
140         xs = x*cos(R45) - y*sin(R45);
141         ys = x*sin(R45) + y*cos(R45);
142         //translation
143         ys = ys + 150;
144         //second rotaion
145         x = xs;
146         y = ys;
147         xs = x*cos(rot) - y*sin(rot);
148         ys = x*sin(rot) + y*cos(rot);
149         for (int j = 0; j < subEvents; ++j)
150         {
151             xe = (RandomNum()*14) - 7;
152             ze = (RandomNum()*14) - 7;
153             dist =
154                 ↪ sqrt((xs-xe)*(xs-xe)+(zs-ze)*(zs-ze)+(ys)*(ys));
155             for (int k = 0; k < HistAmount; ++k)
156             {
157                 if ((dist>=(min + (double)k*Histbin))
158                     ↪ && (dist<(min +
159                     ↪ (1.0+(double)k)*Histbin)))
160                 {
161                     histcount[k] = histcount[k] +
162                         ↪ 1/((double)events);
163                 }
164             }
165             k = HistAmount;
166             break;

```

```
161         }
162     }
163 }
164 if ((i%100) == 0)
165 {
166     printf("%.2f\rSim..    ",
167           ↪ ((double)i/(double)events*100));
167 }
168 }
169 printf("\rSim..    100.00");
170 }
```
